

A NEW DIMENSION IN UROLOGY: ADVANCED 4D MODELING TECHNIQUES TO
UNVEIL SEX-SPECIFIC BLADDER MECHANICS

By

Elijah Broemer

A DISSERTATION

Submitted to
Michigan State University
in partial fulfillment of the requirements
for the degree of

Mechanical Engineering—Doctor of Philosophy

2024

ABSTRACT

Bladder health and dysfunction is not well understood. Research with mouse models is an effective way to study soft tissue/organ function especially with the genetic tools available in this species. Despite this advantage, bladder research in mice is still lacking compared to other animal models. Particularly, mechanical testing/analysis of the mouse bladder tissue are near non-existent in literature. In this dissertation, experimental *ex vivo* pressurization of whole mouse bladders was used to analyze the mechanical stresses and stretches in the soft tissue. Bladder filling cycles were digitally reconstructed in four dimensions (4D: 3D space + time). The reconstructions were used to characterize the geometry and mechanics of the bladder as it fills. This led us to the novel discovery that male and female bladder behaves in significantly different way, even in health. This work contributes to the bladder mechanics literature as this level of 4D and mechanical analysis of bladder filling in a mouse model has not been shown before.

Dedicated to my brother,
Joshua Broemer
2000-2022

TABLE OF CONTENTS

CHAPTER 1	INTRODUCTION	1
1.1	Bladder Dysfunction	1
1.2	Bladder Health.....	2
1.3	Tools to Study Bladder Function	3
1.4	The Mouse Model	6
1.5	Anatomy	8
1.6	Mechanical Testing	14
1.7	Bladder Mechanics.....	17
1.8	Digital 3D Reconstruction.....	22
CHAPTER 2	MODELING BLADDER MECHANICS WITH 4D RECONSTRUCTION OF MURINE EX VIVO BLADDER FILLING	29
2.1	Introduction	29
2.2	Methods.....	30
2.3	Results	36
2.4	Discussion	43
2.5	Conclusion.....	46
2.6	Supplementary Material	46
CHAPTER 3	ADVANCED MODELING TO REVEAL SEX-SPECIFIC DIFFERENCES IN WHOLE BLADDER FILLING MECHANICS	49
3.1	Introduction	49
3.2	Methods.....	49
3.3	Results	52
3.4	Discussion	60
3.5	Conclusion.....	62
CHAPTER 4	UNIAXIAL BLADDER RING TESTS REVEAL SEX-SPECIFIC DIFFERENCES IN BLADDER TISSUE MECHANICS	64
4.1	Introduction	64
4.2	Methods.....	64
4.3	Results	73
4.4	Discussion	77
4.5	Conclusion.....	79
CHAPTER 5	SUMMARY	80
BIBLIOGRAPHY		84

CHAPTER 1

INTRODUCTION

1.1 Bladder Dysfunction

Bladder dysfunction is prominent in humans. Large-scale surveys of adults have estimated the prevalence of bladder dysfunction in Western populations is between 10-20%.^{1,2} Prevalence of at least one bladder symptom has been estimated at 40-70% of the world population.³⁻⁵ Treating bladder symptoms is challenging since the pathogenesis of dysfunction is often unclear⁶ and there are multiple risk factors including age, sex, body mass index, and high-impact sport.^{1,2,7-10}

The concept of bladder dysfunction is separated into storage dysfunction or voiding dysfunction.¹¹ Storage dysfunction is defined by the International Continence Society as “abnormal changes in bladder sensation, ... pressure or bladder capacity”, while voiding dysfunction is defined as “abnormally slow and/or incomplete bladder emptying manifest as an abnormally slow urine flow rate and/or an abnormally high post-void residual”.¹¹

Dysfunctions are diagnosed by patient symptoms and urodynamic testing.¹¹ Urodynamic study in the clinical setting involves artificial bladder filling followed by conscious voiding all while measuring bladder pressure and volume. This test is called cystometry. Pressure is measured via a double-lumen catheter, and volume is quantified by imaging the abdomen (via X-ray, CT scan, or ultrasound) and recording the infused and voided volumes. Abdominal pressure may also be measured to account for non-bladder pressure events such as coughing.¹¹ Dysfunction diagnosis is then done by comparing the pressure-volume chart to published standards for normal or dysfunctional cystometry results and pressure-flow nomograms,¹¹⁻¹³ and by interpreting the patient’s first sensation, normal urge, and strong urge to void during the test.¹¹

Patient-reported lower urinary tract symptoms (LUTS) can also inform dysfunction diagnosis.¹¹ LUTS are defined as “a symptom related to the lower urinary tract; it may originate from the bladder, prostate, urethra, and/or adjacent pelvic floor or pelvic organs”.¹¹ These symptoms may include for example: increased urinary frequency, incontinence, intermittent or slow voiding, or urinary tract infection. LUTS are the primary signal for some bladder-related dysfunction; however the root cause of the symptoms can be hard to determine from symptoms alone, and as such, the bladder has long been called an “unreliable witness”.¹⁴⁻¹⁷ For example, LUTS prevalence is high as 80% in spinal cord injury patients,¹⁸⁻²¹ but the initial symptoms are

the result of nervous system dysfunction (spinal shock), not a bladder pathology.²²⁻²⁶ However, the long term effect of the nerve dysfunction leads to bladder wall tissue remodeling and altered bladder function, which is then specifically a bladder dysfunction.²⁷⁻³² The challenges in assessing bladder health/dysfunction will be discussed further in the following sections.

1.2 Bladder Health

Bladder health has been defined as “a complete state of physical, mental, and social well-being related to bladder function and not merely the absence of LUTS” by the consortium on Prevention of Lower Urinary Tract Symptoms.³³ In regard to storage, a healthy bladder should be able to “hold urine for a reasonable duration of time and sense bladder fullness without fear of or concern about urgency, discomfort, or leakage”, while for voiding having “the ability to empty the bladder completely in a timely, efficient, effortless, comfortable manner”.³³ The consortium also asserted that objective measures should also be used to determine bladder health. These include: healthy first sensation and strong urge to void, capacity, duration of voiding, and time between voids.³³ Yet, they have not published data on normative bladder function to declare what these parameters should be in the “healthy” state. Herein lies a significant gap in the literature on bladder health. There is simply not enough evidence of measurable parameters to draw a consensus on healthy bladder function.³⁴⁻³⁸ Instead, much of the literature on bladder function is on the dysfunctional state.^{33,34} While studying dysfunction is crucial for disease treatment, the lack of healthy reference information leaves no context for understanding the research on dysfunction.

Although there are no established standards, there are studies on parameters for healthy bladder function. Healthy subjects will have between 4-12 voids per 24 hours, with 0-1 voids at night.^{34,39-45} Normative voiding time based on meta-review has been estimated between 23-33 seconds,^{34,35} and total voided volume over 24 hours is between 1400-1700 mL.^{34,37} Sex comparisons have found that males void at higher volumes and less frequently than females, although total voided volume over 24 hours and fluid intake were not found to be different.^{44,46} Brain activity in regard to bladder control has gender differences in the areas of neural activation and intensity as well.⁴⁷

Looking at normative parameters for bladder sensation, first sensation occurs between 100-250 mL, urge to void between 200-350 mL, and strong urge is from 350-500+ mL.⁴⁸⁻⁵¹ It should be noted that the healthy subjects in these studies are often included based on self-reported normal bladder health, when they may in fact have some non-normative function to which they have

acclimated.¹⁵ The subjectivity of bladder health, and the variability of these many “healthy” bladder parameters hint at the difficulty in establishing standards for normative bladder function.

1.3 Tools to Study Bladder Function

Cystometry is called the gold standard for measuring bladder function.⁵²⁻⁵⁷ It is indeed the best way for fully profiling filling and voiding behavior, and there are many parameters which can be gleaned from the test. Objective measures include: flow rate (maximum and average; named Q_{\max} and Q_{ave}), time to maximum flow rate (tQ_{\max}), intravesical pressure (i.e., internal bladder pressure), bladder capacity, the volume/pressure at which sensations occur (first, urge, and strong urge), and compliance (the relationship between volume and pressure, calculated as $\Delta V/\Delta P$).¹¹ Cystometry may be recorded in a single session, with simultaneous urinary tract imaging (videourodynamics), or for an extended period (ambulatory urodynamics).¹¹

Other methods for bladder assessment include free uroflowmetry or a bladder diary.¹¹ Free uroflowmetry is non-invasive and provides measures of flow rate, flow continuity, voided volume, and voiding time. This test only profiles voiding and cannot assess storage. A bladder diary in which voiding frequency and volume are recorded can also inform bladder health assessment. These methods are more accessible than cystometry with the tradeoff of less information.

Cystometry is the most comprehensive bladder test; however, it is not without its limitations. This test is invasive, requires special equipment/expertise not all clinics may have, and the results may not be comparable to published data if the established guidelines are not followed carefully (e.g., patient posture, infusion fluid properties, and fill rate).¹¹ It has been shown that the data is not repeatable in the same subject with successive testing.^{38,58} Furthermore, and as discussed earlier, the volumes at which sensations occur (first, normal, strong urge), and urodynamic parameters used for diagnosis are not consistent across healthy subjects.^{38,48,59}

Further illustrating the difficulty in assessing pressurized organs, one can look at lung testing for comparison. The lungs undergo pressure and volume changes via fluid flow, which are measurable similar to the bladder. The literature shows that, like the bladder, normative parameters from lung testing are not well defined and can have large variability.⁶⁰ Pressure-volume curves are obtained from lung testing and, like the bladder, these curves are not trivial to interpret.⁶⁰ The challenge in profiling these organs can be explained by the complexity of their multi-system function. The bladder does not function alone; it is a sophisticated interaction between the bladder wall, pelvic muscles, urethral sphincters, and neurological regulation. The same can be said for the

lungs, which function as the combined interaction of the lungs, chest wall, airway passages, and neurological regulation. It is for this reason that there has been an increasing call for investigating lung function in relation to the tissue mechanics.⁶⁰⁻⁶² It can be argued that there is a similar need for better understanding of bladder tissue mechanics as a means for assessing bladder function.

In pulmonary function testing and cystometry, compliance is a standard clinical measure that quantifies mechanical function of the target organ (i.e., distensibility).¹¹ It is calculated as the change in pressure per change in volume when filling from empty.¹¹ This “mechanical” measure is fraught with issues though. The International Continence Society standardized this parameter in 1976,⁶³ and still recommends its use for bladder assessment¹¹ even though it has been known to be highly variable in healthy subjects for over four decades.^{64,65} Furthermore, it can be completely misleading as an indicator for tissue distensibility. While compliance is purported to be a comparable metric for modulus of elasticity^{65,66}, it is not. A bladder with supposed low compliance, as indicated by the pressure-volume data, can actually have a higher compliance if modulus of elasticity is analyzed from stress-stretch data (Figure 1.1).⁶⁷ To understand this conflict, the definition(s) of compliance must be unpacked further.

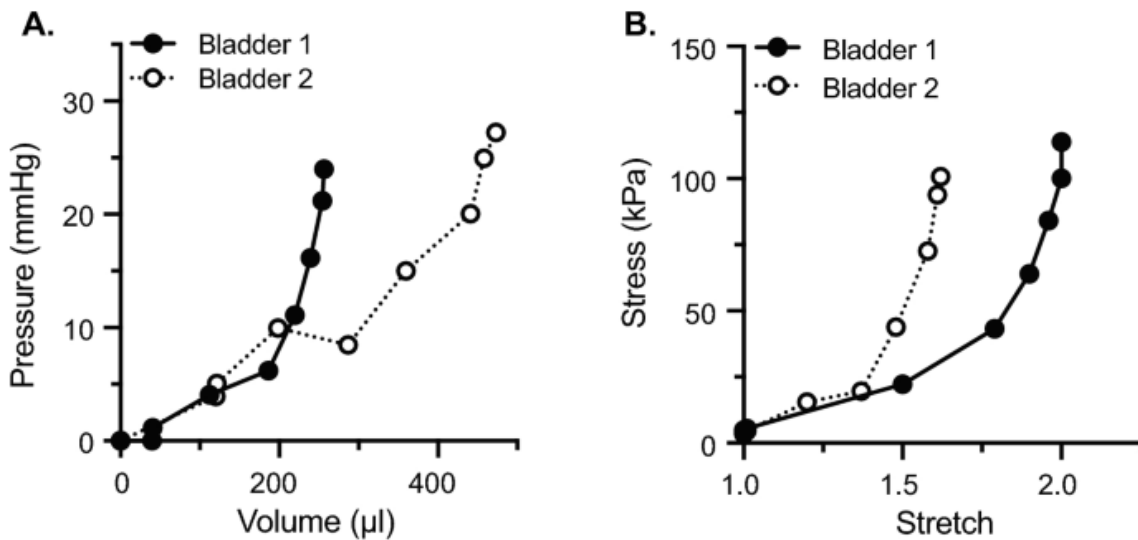


Figure 1.1: Different conclusions about bladder distensibility obtained from bladder compliance vs. mechanical compliance.⁶⁷ A) Bladder compliance, as derived from pressure-volume data, cannot show the true nature of bladder wall stiffness. B) Stress-stretch data provides more accurate results not captured by pressure and volume alone. Reproduced from Hennig et al. 2022.⁶⁷

Compliance as discussed, which may also be called bladder compliance, suffers from homonymy between the fields of urology and mechanics.^{11,65,66} Further complicating the issue, the objective of the compliance measure is the same between the fields – it is a measure of distensibility. However, the measure is obtained differently in urology vs. mechanics, and they are often discussed as equivalent when they are not.^{68–70} The term “compliance” in the field of mechanics is defined as the inverse of stiffness, or modulus of elasticity, which is the change in stress by change in strain.⁷¹ Bladder compliance is used as a proxy measure for mechanical compliance as the ratio of pressure to volume is said to be a substitute for the ratio of stress to strain.^{69,70} The difference is that mechanical stress accounts for the material geometry, which in this case would be bladder wall thickness, and that strain is normalized. Mechanical metrics are superior for analyzing bladder function for these reasons, in addition to the fact that stress and elasticity correlate with sensation and bladder muscle activity, whereas bladder compliance does not reflect these bladder functions.^{72–74}

Standard urological assessment methods can be more valuable with some extension into macroscopic tissue mechanics. Urologists and urology researchers may not be engineers, but they have the tools and capacity to include some straightforward mechanical analysis which can enhance medical insights. For example, bladder wall thickness can be measured via ultrasound.^{75–79} Then, with the commonly used method of modeling the bladder as a sphere,^{72,80–82} a bladder effective radius can be estimated, and mechanical stress (σ) and strain (ε) may be calculated with the thin-walled spherical pressure vessel equations from Laplace’s Law⁸³ given in Equation (1.1):

$$\sigma = \frac{Pr}{2h}, \quad \varepsilon = \frac{r}{r_o} \quad (1.1)$$

where P is the bladder pressure measured during cystometry, r and r_o are the radius during filling and radius at empty, respectively, and h is the bladder wall thickness. This method of determining bladder distensibility/stiffness is more accurate and relevant than the traditional bladder compliance measure since it accounts for the bladder geometry and is normalized.

Beyond extending current standard assessment methods, there is a need to “reverse engineer” the bladder, so that the underlying mechanisms which drive its functions can be better understood. A common method engineers use for researching mechanical behavior of soft tissue

is stretching excised tissue strips and recording the loading and deformation characteristics (stress and strain).⁸⁴⁻⁸⁹ This method is limited in that it does not reflect the *in vivo* loading conditions; however it allows for direct measurement of the tissue's material properties with well-established mechanical tests. Tissue strip stretch tests have indeed revealed that the bladder wall has anisotropic behavior (directional material properties), and that the bladder wall has stress-regulating components that behave differently in diseases, such as diabetes.⁹⁰⁻⁹⁶ For more accurate physiological mechanical testing, preliminary methods were developed by researchers for tracking the mechanical behavior of the whole bladder during pressurization.^{95,97-104} These tests have validated that the bladder has directional mechanical behavior, and that the shape of the organ is best approximated by a spheroid.^{105,106} Whole organ pressurization methods are limited in that they are less standardized than planar tissue stretching, but the fact that the true loading behavior of the tissue is captured provides significant value. These types of mechanical testing tools are not yet integrated into urological assessment methodologies, but as their value is continually demonstrated, mechanical testing may be the missing link needed to better characterize bladder health and dysfunction. Developing whole bladder pressurization mechanical models is a primary aim of this dissertation, which will help understand *in vivo* function in terms of bladder mechanics.

1.4 The Mouse Model

Animal models are popular for research and development of mechanical testing and modeling the bladder. Pigs and rats are commonly used animal models for bladder mechanical testing.^{27,29-31,81,96,103,107-111} The mouse model, however, has been underutilized in this field of research.¹¹²⁻¹¹⁴ The reasons for this may be due to the smaller size of the bladder can make it more difficult to work with compared to pigs or rats, and the fact that the mouse bladder lacks smooth muscle in the mucosa layer that is present in larger animals (anatomy to be discussed in the next section). These "limitations" can actually prove to be advantageous. As will be explored in Chapter 2, the smaller diameter and thinner bladder wall in mice allowed for a novel whole-bladder pressurization device and mechanical modeling method to be developed.⁶⁷ Furthermore, mouse models have many benefits compared to other animal models. Mice are more cost-effective due to their smaller size and faster maturation vs. pigs and rats.¹¹⁵⁻¹¹⁷ There are also a number of standardized mouse models for health and disease.¹¹⁸⁻¹²³ This aids in reproducibility of research, and allows results from different labs to be compared. Finally, mice are powerful models due to the established genetic manipulation tools available. Methods such as cre-lox recombination and

CRISPR/Cas9, allow targeted DNA modifications to knockout or knock-in genes to explore their function or mimic diseases in humans.^{124–126} For these reasons, mice are a go-to animal model for biomedical research, although these advantages have not been utilized to their potential for the study of bladder mechanics.

One must certainly be cautious in extrapolating results found in mouse models to humans, but for development and validation of mechanical testing methods and models, they are valuable as explained above. Additionally, there are still notable similarities between humans and mice. For one, it is known that 80% of the mouse genome is shared by humans.¹²⁷ Moreover, in regard to the bladder, human and mouse bladders function within similar pressure and stress magnitudes.^{67,72,128,129}

When fully developed, the mouse urinary bladder *ex vivo* tissue weighs ~50 mg with an area of 100 mm² when empty and flattened – roughly the weight of 2 grains of rice and similar in size to an M&M.^{130–132} Typical fluid capacity of the mouse bladder is around 200 μL, which is equivalent to 4 drops of water.^{133–135} Mice will void a total of 2-4 mL/day with an average fill rate of 2 μL/min.^{136–138} Filling and voiding patterns can be affected by sex, stress, and age.^{112,138–143} Genetic background also affects mouse bladder function.^{142–144} While all this is known, research on the mouse bladder – and especially bladder mechanics – is lacking. The paucity of literature on mouse bladders is an open invitation for basic research on this organ (although few may be tooled to accept it). More research on the mouse bladder will allow the power of genetic models in the mouse to be leveraged for deeper understanding of the bladder.

Presently, literature on the physiological mechanical behavior of the mouse bladder is sparse to non-existent. There are few studies that analyze the loading/stress behavior of the bladder wall in mouse models. However, in all of these studies, the data was collected via bladder tissue sectioned into strips and uniaxial or biaxial extension.^{113,114,145–147} While these studies are still useful, they are not true to the actual mechanical loading of the bladder *in vivo*. Sectioning damages the tissue and alters the boundary conditions, as the *in vivo* organ is loaded via pressurization and not planar extension. The mechanical stresses of the pressurized mouse bladder have not been quantified before. In contrast, bladder research in humans, pigs, and rats has developed extensive characterization of the tissue mechanics, often with accurate 3D models.^{99,104,148}

The scientific community knows much about mice and much about bladder mechanics; yet, the Venn diagram intersection of these two is extremely thin. The aims of this dissertation are

to: A) quantify wall stresses of the pressurized bladder in a mouse model, and B) elevate mouse bladder research up to the level of other animal models with 3D modeling and mechanical analysis.

1.5 Anatomy

The mouse bladder has a unique structure which allows it to be highly distensible while maintaining low internal pressure. Its primary functions are to store and facilitate evacuation of urine, and to prevent waste products from re-entering the body during storage. The bladder wall is composed of layers with each contributing to the organ's functions. Figure 1.2 gives a schematic identifying the different layers, and Figure 1.3 shows a cross-section micrograph of the layers in mouse tissue. The bladder wall structure is not as complex as other tissues, such as vasculature and the gut,¹⁴⁹ but it does have some specialized components which are unique to this organ.

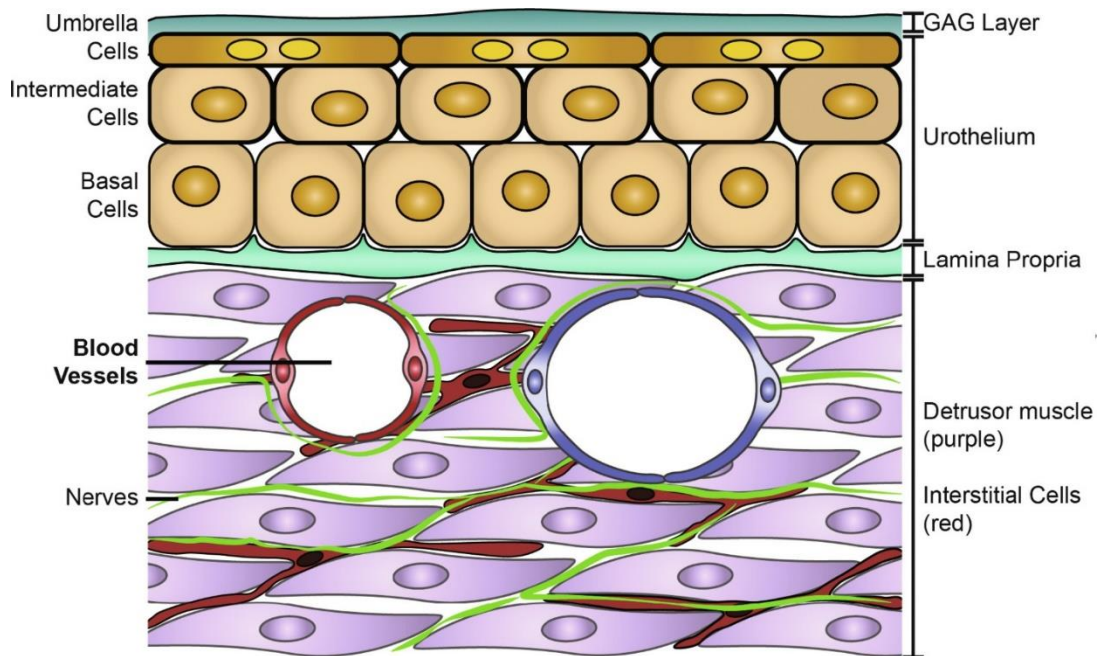


Figure 1.2: Schematic of bladder wall in mice. Reproduced from Tykocki et al. 2022.¹⁵⁰

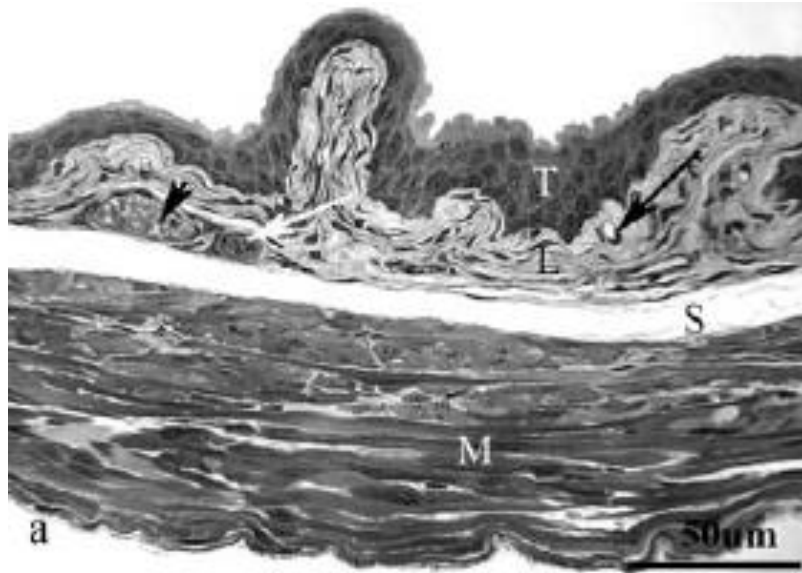


Figure 1.3: Cross section of the mouse bladder wall. T, transitional epithelium/urothelium; L, lamina propria; S, submucosa; M, muscle layer. Reproduced from Hossler et al. 2013.¹⁵¹

The inner-most layer of the wall is the urothelium, which serves as the impermeable barrier between urine and the underlying tissues.¹⁵² The urothelium has been shown to be the strongest epithelial barrier in the body across species.¹⁵³ This is accomplished by the combination of a glycosaminoglycan (GAG) surface barrier, which is protective against bacteria and other inflammatory insults,^{154,155} and umbrella cells that are unique to the bladder urothelium. The umbrella cells of the urothelium are highly compliant,¹⁵⁶ and as the bladder fills, their shape changes from cuboidal to a flat lengthened shape with an increased surface area to accommodate stretching of the bladder wall.¹⁵⁷ In addition to being a protective barrier, the urothelium has a significant role in the mechanical behavior of the bladder wall. Specifically, the urothelium shows stretch-induced cellular signaling.^{147,158–161} Moreover, the urothelium contributes significantly to the elasticity and compliance of the bladder wall,^{92,147,162} which has been suggested to be driven by a muscle-relaxation mechanism of the urothelium in response to stretch.^{92,162–165} Another factor is the strong tight junctions that are the bond between the umbrella cells, which may also contribute to the overall stiffness of the bladder wall, although this factor has not been well explored.^{166,167}

The urothelium and lamina propria make up the bladder mucosa. When relaxed, the mucosa has a high degree of folding.^{168–170} Figure 1.4 shows these folds on the inner surface of the bladder. As the bladder is filling, these folds (also called rugae) flatten and contribute to the high

distensibility of the tissue. After flattening, the lamina propria, which is primarily connective tissue, stretches for further accommodation of urine.^{146,170} Figure 1.5 shows two cross sections of the whole bladder highlighting the extensive inner folding and thickness of the detrusor layer. As mentioned previously, the mouse bladder wall is unique in that it lacks smooth muscle in the lamina propria (muscularis mucosa).¹⁷¹ Based on evidence that removing the detrusor muscle from the mouse bladder has no significant effect on the pressure-volume profile during filling,¹⁶² it is possible that the mucosa is largely responsible for the passive mechanical behavior of the bladder during filling. Passive accommodation is indeed the role of the lamina propria's elastin-collagen network as the bladder is filled.

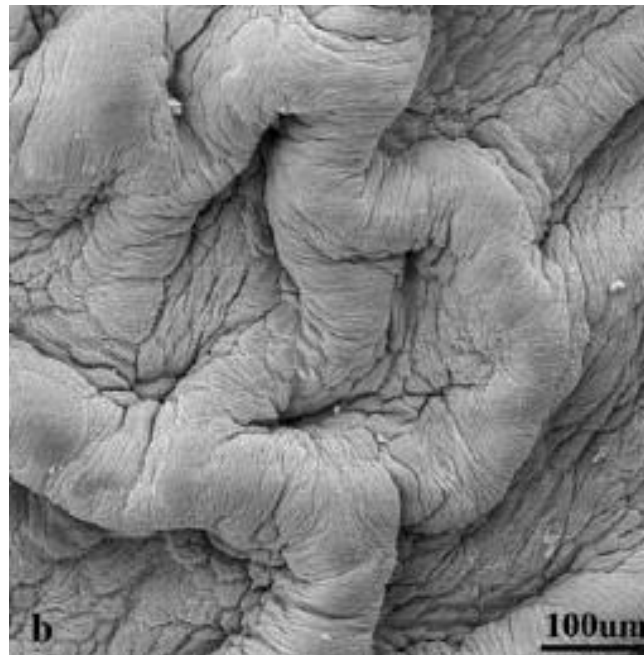


Figure 1.4: Folds in mouse bladder urothelium. Reproduced from Hossler et al. 2013.¹⁵¹

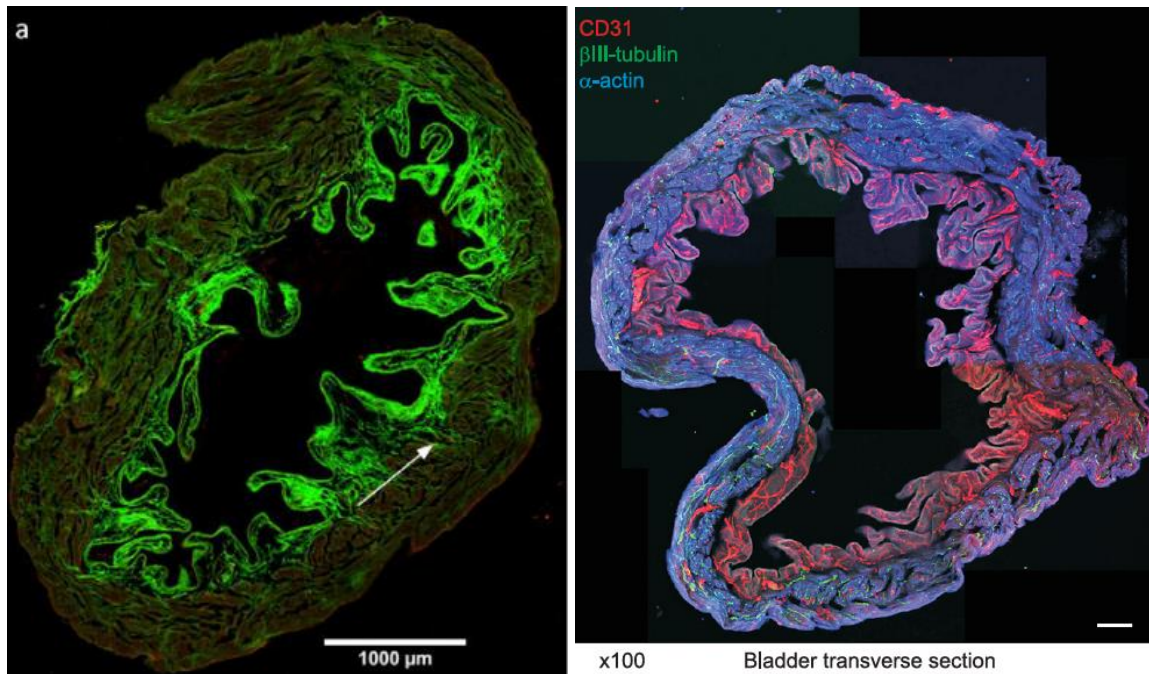


Figure 1.5: Cross sections of relaxed mouse bladder showing extensive folding on the inner mucosa layer. Left: green shows collagen and arrow indicates mucosa/detrusor boundary. Reproduced from Hornsby et al. 2017.¹⁴⁶ Right: blue shows urothelial cells, blue shows muscle cells. Reproduced from Nguyen et al. 2021.¹⁶⁹

Below the mucosa is the smooth muscle layer, called the detrusor, which is the active part of the wall.¹⁷⁰ Contraction of the detrusor allows the bladder to empty, while the muscle must relax during filling to allow distensibility. An interesting feature of the detrusor is that, during filling, the muscle exhibits rhythmic transient contractions called non-voiding contractions.^{172–174} These contractions may act as a “pressure monitoring” function via the stress response of the bladder wall.^{175–177} To elaborate, when the bladder is at a low volume, these contractions are able to be dispersed throughout the tissue as it still has appreciable elasticity. However, when the bladder is nearing its capacity, the tissue has increased stiffness, and these contractions transiently increase the stress on the bladder wall which increases the signal to void via bladder sensation.^{72–74,172} However, this pressure monitoring function is still a hypothesis. Transient bladder contractions are well known in the literature, and it has been made clear that the bladder wall has mechanosensory components, but the exact mechanisms by which the bladder is able to sense stretch and stress are unknown.

Beyond the detrusor muscle, there is another connective tissue layer called the adventitia. This layer is a mesh-like arrangement of collagen and elastin.¹⁷⁰ It should be noted that while the layers of the bladder wall have distinct functions, they themselves are not neatly divided. In reality, the layers have some degree of entanglement between one another, and connective tissue (collagen and elastin) is dispersed throughout the bladder wall layers as the “glue” holding it all together.^{170,178} Even in the detrusor layer, connective tissue is found permeating the muscle bundles/fascicles/fibers. Finally, the outermost layer of the bladder wall is covered in mesothelial cells, which create a slippery surface allowing the organ to slide freely on other abdominal tissues as it distends and deforms.^{179,180}

Each of the bladder layers has a significant blood and nerve supply, with nerve endings particularly concentrated between the lamina propria and detrusor muscle.^{151,169,181} Bladder vasculature has a unique structure with many features that allow it to maintain blood flow even as the tissue is stretched and compressed during filling. In particular, the mucosa has a dense mesh-like network of capillaries arranged with extensive cross-connections for collateral circulation.¹⁵¹ Figure 1.6 shows the complex bladder vasculature via corrosion casting imaging.

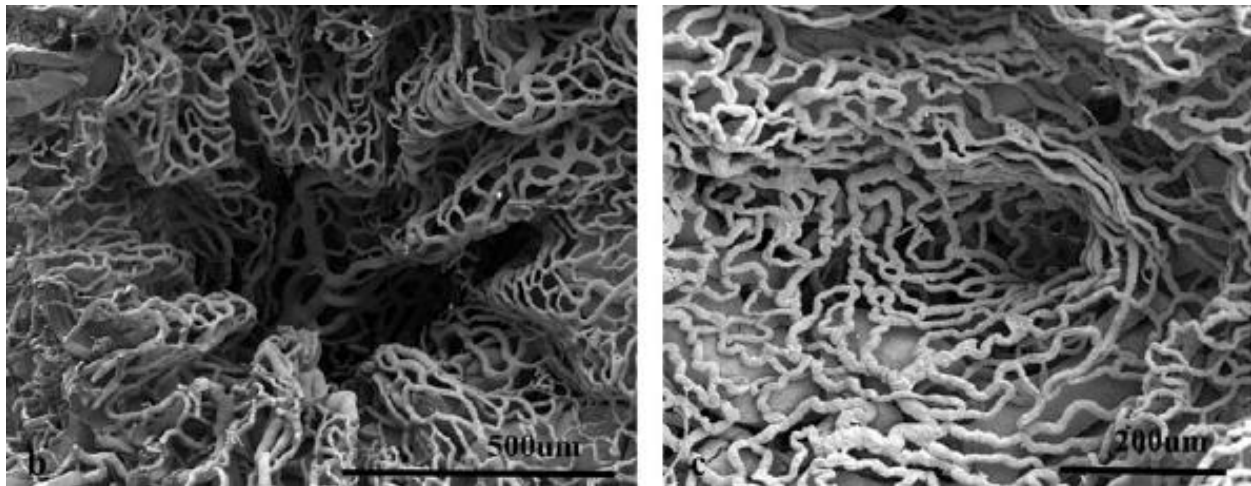


Figure 1.6: Corrosion castings of mouse bladder capillary structure. Left shows the fine blood supply of the bladder wall around the urethral outlet, Right shows a ureteral inlet.

Reproduced from Hossler et al. 2013.¹⁵¹

While this dissertation is primarily focused on the bladder wall itself, it cannot go without mentioning the bladder neck (urethral outlet) and the ureters. The bladder is comparable to a

balloon in shape and with each narrowing down to an opening at the bottom neck. The trigone is a triangular structure at the neck which includes the urethral sphincter and two ureters at each “corner” (each orifice is also visualized by Figure 1.6).^{182–185} The trigone is part of the bladder wall, but does not exhibit appreciable deformation during filling as it is stiffer than the rest of the luminal wall.^{93,186} The two ureters provide the inflow of urine from the kidneys, and the urethral sphincter relaxes to permit voiding.^{187–190} The ureters are open to one-directional flow (although reflux is possible as a dysfunction), and the urethral sphincter is held closed except during voiding. Although each is important for bladder function, this dissertation will make minimal reference to these anatomical features. The focus here is on the mechanics of the deformable bladder wall tissue. Furthermore, as will be explored in the next section, mechanical testing of the whole bladder typically involves closing or disregarding the ureters, and artificial filling and voiding is often accomplished by infusion/outflow from a catheter via the urethral opening, which nullifies the sphincter action.

The final detail worth mentioning is nomenclature for the anatomical directions used to describe the bladder. Figure 1.7 illustrates the two common directions, namely circumferential denoting the transverse orientation, and longitudinal denoting the apex-to-base (dome-to-neck) orientation. For the purposes of the current work, the longitudinal direction is not specific to the coronal or sagittal planes. Although the bladder wall does have some distinct structure front-to-back, this is beyond the scope of this dissertation and is left to be explored in future work.

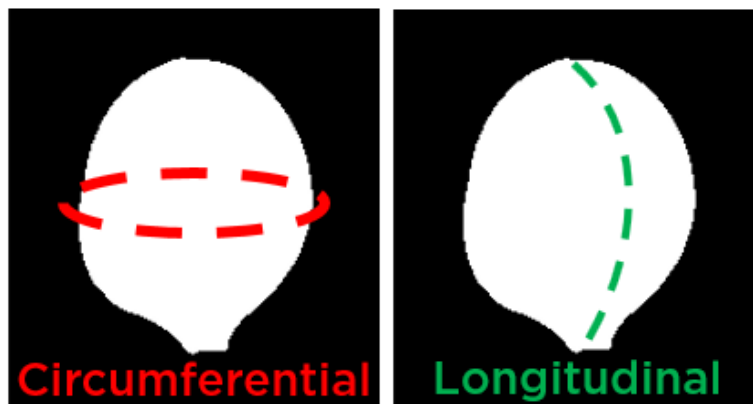


Figure 1.7: Directions used to describe the bladder. The top of the bladder is called the dome, while the bottom is called the base or trigone.

1.6 Mechanical Testing

The method of measuring bladder physiological function *in vivo* via artificial filling is termed cystometry. Fluid, typically saline, is infused at a specified flow rate through a double-lumen catheter. Internal bladder pressure is measured via a pressure transducer in-line with the fluid infusion. The pressure is plotted against the infused volume or infusion time. The shape of this plot reflects bladder function. Typical bladder function shows an initial phase where the pressure is low and slowly increasing as the organ expands. As the bladder tissue approaches its elastic limit, the pressure ramps up quickly with a corresponding sensory urge to void. Figure 1.8 illustrates this typical bladder pressurization behavior in a conscious mouse.

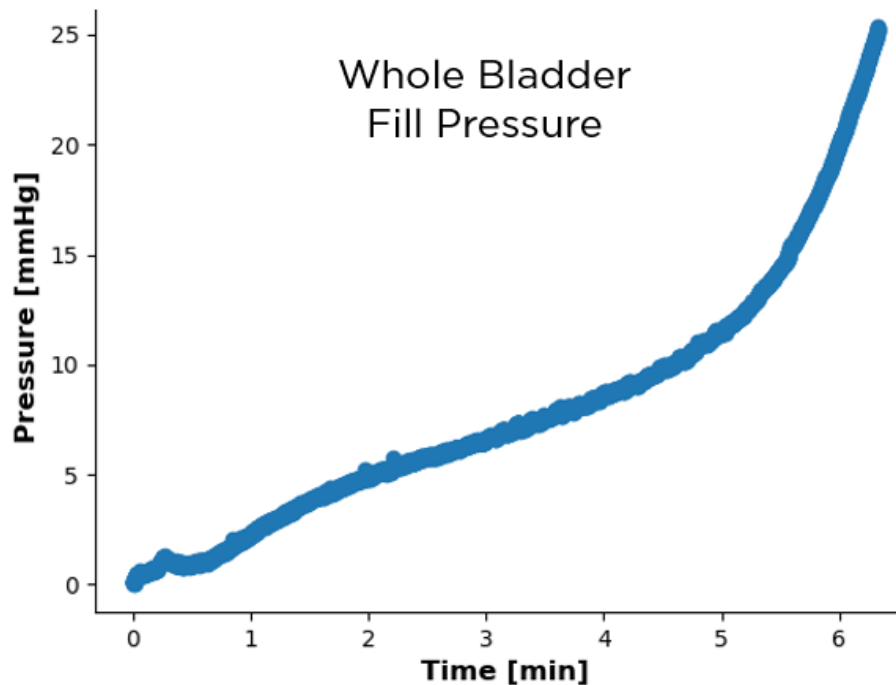


Figure 1.8: Bladder pressurization from *ex vivo* mouse bladder filled at a rate of 30 $\mu\text{L}/\text{min}$.

While previous studies have not included mechanical analysis, there are several reports of whole-bladder filling experiments in mouse models. These studies primarily analyze bladder physiological function *in vivo* with two approaches. In one approach, the animal is catheterized via the urethra (traditional catheterization). Another approach is surgically implanting a tube at the dome of the bladder. Traditional catheterization can be used to both fill and empty the bladder. However, this method can disrupt physiological voiding function as the infusion route blocks

natural outflow, and the fact that with current tools it is nearly impossible to catheterize the male mouse without damage to the urethra.^{191–193} Surgical implantation of a tube at the bladder dome is only intended for filling; the tube acts as a synthetic 3rd ureter. This procedure is more invasive, and the surgical implantation can confound the bladder mechanics due to wound healing and remodeling around the surgery site which will alter the tissue mechanics. However, dome catheterization allows for the bladder neck and urethra to remain unaffected which is valuable for studying voiding function. Bladder filling experiments may also be done *ex vivo*, with the bladder excised and catheterized via the urethra.^{128,162,172} In this case, voiding function is clearly no longer present, and the ureters need to be closed off to prevent leakage. This method may be preferred over *in vivo* experiments so that the bladder tissue is better isolated for imaging in certain experimental setups.⁶⁷

Regardless of the method which the bladder is filled, the rate of fluid infusion must be considered. As with any soft tissue, the observed mechanical behavior depends on the rate of deformation. In bladder tissue this is due to viscoelastic characteristics of the connective tissue and relaxation of the smooth muscle (often called “tone”). There is no standard filling rate for cystometry. Physiological filling occurs around 1-2 $\mu\text{L}/\text{min}$.^{136–138} Most researchers choose not to use a physiological filling rate since the length of the experiment becomes prohibitive. Studies with mouse cystometry commonly use an infusion rate of 25 $\mu\text{L}/\text{min}$,^{112,144,194–197} although some use rates as low as 10 $\mu\text{L}/\text{min}$,^{139–142} and as high as 50 $\mu\text{L}/\text{min}$,^{197,198} or even 100 $\mu\text{L}/\text{min}$,^{159,199–201} and some use a range of fill rates.^{128,133,135} Infusion of room temperature fluid is standard, however one study was found which used 37°C fluid. Viscoelasticity of the bladder tissue may be affected by the temperature of infused fluid,^{82,202,203} and the kidneys infuse the bladder at body temperature, so artificial filling with a fluid at body temperature is justified for mimicking physiological conditions.

Since the bladder wall exhibits viscoelastic characteristics, the fill rate will directly affect the observed mechanical behavior.^{202,204} The ability for soft tissue to deform has a time-dependent characteristic as the microstructure reorganizes and relaxes over time. Studies that have tested a range of fill rates show how this variable affects the bladder behavior.^{128,133,135} Slower fill rates allow the constituents of the bladder wall to have more time to reorganize and relax.¹³⁵ So, experiments with slower cystometry fill rates will better reflect physiological conditions with greater capacity and distensibility. However, there is conflicting data on this. One study found that

increasing fill rates show decreasing bladder capacity,¹³⁵ while another study found that different fill rates did not affect capacity.¹³³ The different results found by similar studies may be due to the different mouse strains tested, or to one study being performed in unconscious animals and the other used awake animals. Other results from varying fill rate show that higher fill rates increase bladder pressure overall (at baseline and at maximum), and that voiding occurs more frequently.¹³³ There is other evidence that fill rate does not cause more frequent voiding.¹²⁸ This shows that while the fill rate can affect the bladder behavior, it is only a contributing factor and may have complex interactions with other aspects of bladder filling.

Preconditioning is also important when mechanically testing soft tissues.²⁰⁵ Preconditioning refers to the practice of repeating mechanical loading to allow for hysteresis to be minimized which results in repeatable behavior. Mouse cystometry studies may perform 3 cycles,²⁰¹ 4 cycles,^{139–141} or simply state that they started recording data once it appeared repeatable.^{112,197} However, many studies make no mention of repeatability when testing this soft tissue. It is arguable whether the bladder is preconditioned as it functions *in vivo*. Bladder filling via the ureters is continuous, although it has been shown that fill rate has some variation with circadian rhythms.^{135,206} On one hand, the slow continuous and repeated filling of the bladder are good arguments for the bladder being preconditioned *in vivo*. On the other hand, the nature of voiding is not reflective of preconditioning. Voiding incurs large contractile deformation in a very short time frame compared to filling, and has a cycle rate on the order of hours. Thus, it seems reasonable to conclude that the bladder is preconditioned *in vivo* during the natural filling phase, but the voiding phase does not reflect the concept of preconditioning.

In vivo bladder filling experiments may be performed in animals under anesthesia or while conscious.^{112,172,207,208} When feasible, conscious cystometry is most physiologically accurate, as it has been shown that cystometry under anesthesia affects bladder function.²⁰⁹ Moreover, the type of anesthesia used can disrupt bladder function to different degrees. Urethane is preferred for anesthetized cystometry. While urethane does have some effect on bladder function, other types of anesthesia, particularly isoflurane, can significantly alter the observed bladder behavior.^{210,211}

A relevant factor of interest in bladder filling is the point where the organ signals the desire to void. In *ex vivo* conditions, the bladder may be filled until leakage occurs. However, leakage is not typical physiological behavior. *In vivo* studies are more useful in determining the point where desire or urge to void occurs. Conscious cystometry is the best source of this information, since

anesthesia can suppress sensory signaling. Unconscious animals do still void, however it seems to be delayed compared to awake animals.¹⁹⁴ In unconscious mice, voiding occurs around 20-30 mmHg,^{112,135,144,194} while in conscious mice, voiding occurs around 15-20 mmHg.^{140,142,194,197} 25-30 mmHg has been deemed to be the “max” physiological pressure by some.^{128,133,135}

Using cystometry it has been found that genetic background,^{142,144} age,¹¹² stress,^{139–141} sex,¹⁴² and time of day¹³⁵ effect bladder function. Bladder wall remodeling (i.e., changes in the wall structure and composition) has been also associated with altered bladder function.^{112,141,197,201} Although there is a chicken-and-egg problem where it is not clear if the remodeling precedes dysfunction or *vice-versa*. Changes in sensory function are also associated with bladder dysfunction,¹¹² and bladder wall remodeling may be downstream of sensory pathology.¹⁹⁵ To create context for the relationship between bladder mechanics, wall microstructure, and dysfunction, it is crucial to investigate the basic mechanics of the bladder wall so that remodeling, as seen in aging and pathology, can be better understood for potential therapies and treatments.

Mechanical stretching of excised bladder tissue strips is another way of measuring the mechanics of the bladder wall. Although uniaxial or biaxial stretching tissue sections may not directly inform bladder function per se, this type of testing is still valuable. As previously discussed, this type of test is a well-established method of material testing, and the loading conditions are not directly reflective of the bladder pressurization *in vivo*. However due to the advanced development of stretch tests compared to bladder pressurization experiments, stretch tests can allow for the material properties to be directly measured, and with advanced imaging techniques simultaneously.¹⁴⁶ This contributes significantly to knowledge about bladder function and bladder mechanics, since the microstructure of the bladder wall can be studied in tandem with the applied deformation.^{146,147,212} Understanding bladder mechanics in terms of the microstructural aspects is necessary for advancing insights into bladder function, and currently planar tissue stretch tests are the best tools available for this goal. The combination of stretch testing and whole bladder pressurization experiments provide powerful tools for researching bladder function at the tissue level and as a whole organ.

1.7 Bladder Mechanics

The urinary bladder is often modeled as a spherical pressure vessel.^{72,73,80,82,129,186,213–217} The law of Laplace is typically invoked when the bladder wall is presumed to be thin-walled.²¹⁸ This law asserts that wall tension $T \propto Pressure \times Radius$. Less often, when the bladder is presumed

to be thick-walled, the more complex Lamé equations are used to model the internal wall stress.²¹⁴ Thin-walled is often defined as the radius being 10× or 20× wall thickness.²¹⁹

Either way, these spherical models imply that the bladder wall tissue is isotropic, homogeneous, incompressible, has uniform thickness, and has no viscous behavior. In reality (and based on the anatomy of the bladder wall) none of these assumptions are valid and the use of Laplace's Law has been long critiqued for this reason.^{218,220} Still, the law is ubiquitous in bladder mechanics research as it is a valuable general principal and is remarkably simple. Furthermore, more sophisticated bladder models which do not assume homogeneity, isotropic, or incompressible behavior show results that do not differ much from those obtained employing Laplace's Law.²²¹ The law of Laplace is quite reasonable barring highly accurate finite element simulations; even then, the results of this simple equation may not be significantly different. This result will be explored later in this dissertation.

The bladder wall undergoes large deformation as it fills, and this is quantified in the measure of stretch, λ . Specifically, the circumferential stretch is calculated as the ratio between the deformed and undeformed circumference. This ratio can be reduced to the deformed radius by the reference radius. The radial stretch is calculated as the ratio of the deformed wall thickness by the reference thickness. Large deformation (finite strain theory) is when the undeformed and deformed configurations are significantly different. Small deformation (infinitesimal strain theory) is when the deformation is small enough that the undeformed and deformed configurations are similar enough to be considered identical.²²² The mathematical notation and models used for deformation/loading of the bladder will be outlined next.

Scalars are denoted by plain letters, vectors are bold, and 2nd order tensors are bold underlined. The reference and deformed configurations are referred to by \mathbf{X} and \mathbf{x} respectively. These are related by the deformation gradient shown by Equation (1.2). Modeling soft tissues commonly includes an assumption of incompressibility.²²³ So, the reference and deformed volumes V and v are equal, and the Jacobian of the deformation gradient is equal to 1. Mechanical behavior is often assumed to be quasi-static and passive (i.e., preconditioned, negligible viscoelastic effects, and no active muscle contraction) when modeling the large deformation of the bladder filling and these effects are not being studied directly.^{29,213,214,224}

$$\underline{\mathbf{F}} = \frac{\partial \mathbf{x}}{\partial \mathbf{X}} \quad (1.2)$$

Strain energy is the energy added to a body via deformation. Like other soft tissues, the mechanical behavior of bladder wall tissue is often modeled by using a strain energy density function, which relates mechanical stress and deformation.^{225–228} Since bladder tissue behaves in a highly non-linear way,^{229,230} the strain energy function used to describe its behavior is typically a power or exponential function^{80,113,224} with constants which may have a physical interpretation (phenomenological)^{231,232} or not.^{80,213} Strain energy density functions, $W(\underline{\mathbf{C}})$, are functions of the right Cauchy-Green tensor, which is calculated as $\underline{\mathbf{C}} = \underline{\mathbf{F}}^T \underline{\mathbf{F}}$. These functions define hyperelastic materials.²³³

The general form relating the Cauchy stress $\underline{\boldsymbol{\sigma}}$ and $W(\underline{\mathbf{C}})$ for an incompressible material is given by Equation (1.3):

$$\underline{\boldsymbol{\sigma}} = 2\underline{\mathbf{F}} \frac{\partial W}{\partial \underline{\mathbf{C}}} \underline{\mathbf{F}}^T - p\underline{\mathbf{I}} \quad (1.3)$$

where p is a Lagrange multiplier related to hydrostatic pressure that enforces the incompressibility, and $\underline{\mathbf{I}}$ is the identity matrix.

The three invariants of the right Cauchy-Green tensor are used to describe the deformation of a body, and strain energy functions are often written as a function of these terms.²²² The first invariant I_1 is a measure of stretch in the three principal directions and is an indicator of the shape change due to deformation.²³⁴ The second invariant captures information about the interaction between the principal stretches as a characterization of shear deformation and anisotropy. The third invariant I_3 quantifies the volume change due to deformation. If volume is or is assumed to be constant throughout deformation, this invariant has a value of 1. The formulation of these invariants is given by Equation (1.4). For isotropic materials, strain energy density can be written as a function of the right Cauchy-Green invariants, and Equation (1.3) can be rewritten as shown by Equation (1.5).

$$I_1(\underline{\mathbf{C}}) = \text{tr}(\underline{\mathbf{C}}), \quad I_2(\underline{\mathbf{C}}) = \frac{1}{2} \left[(\text{tr}(\underline{\mathbf{C}}))^2 - \text{tr}(\underline{\mathbf{C}}^2) \right], \quad I_3(\underline{\mathbf{C}}) = \det(\underline{\mathbf{C}}) \quad (1.4)$$

$$\underline{\boldsymbol{\sigma}} = 2 \left(\frac{\partial W}{\partial I_1} + I_1 \frac{\partial W}{\partial I_2} \right) \underline{\mathbf{F}}\underline{\mathbf{F}}^T - 2 \frac{\partial W}{\partial I_2} (\underline{\mathbf{F}}\underline{\mathbf{F}}^T)^2 - p\mathbf{I} \quad (1.5)$$

Two common isotropic hyperelastic models include Mooney-Rivlin material and Neo-Hookean material.^{235–237} Mooney-Rivlin strain energy function and the Cauchy stress are shown in Equations (1.6) and (1.7) where μ and α are material constants. Neo-Hookean is a special case of Mooney-Rivlin where $\alpha = I$.

$$W(I_1, I_2) = \frac{\mu}{2} [\alpha(I_1 - 3) + (1 - \alpha)(I_2 - 3)], \quad \mu > 0, \quad 0 \leq \alpha \leq 1 \quad (1.6)$$

$$\underline{\boldsymbol{\sigma}} = \mu(\alpha + I_1(1 - \alpha))\underline{\mathbf{F}}\underline{\mathbf{F}}^T - (1 - \alpha)\mu(\underline{\mathbf{F}}\underline{\mathbf{F}}^T)^2 - p\mathbf{I} \quad (1.7)$$

Hyperelastic material models may also be functions of the principal stretches $(\lambda_1, \lambda_2, \lambda_3)$. For example, the Ogden model is commonly used for non-linear elastic isotropic materials when Mooney-Rivlin is not well-suited.²³³ The incompressible case is given below by Equations (1.8) and (1.9):

$$W(\lambda_1, \lambda_2, \lambda_3) = \sum_{n=1}^N \frac{\mu_n}{\alpha_n} [\lambda_1^{\alpha_n} + \lambda_2^{\alpha_n} + \lambda_3^{\alpha_n} - 3], \quad N > 0 \quad (1.7)$$

$$\underline{\boldsymbol{\sigma}} = -p\mathbf{I} + \sum_{n=1}^N \mu_n \lambda^{\alpha_n} \quad (1.9)$$

where N , μ_n , and α_n are material constants, and λ is the principal stretch matrix. When $N = I$ and $\alpha = 2$, the equation reduces to a Neo-Hookean model.

More sophisticated models used for soft tissues are anisotropic and account for directional fibers in the material. These typically are a linear combination of a Neo-Hookean term for the ground matrix, and a directional fiber term for the connective tissue embedded in the ground matrix. For example, an arbitrary two-fiber model²³² is given by Equations (1.10) and (1.11):

$$W(I_1, I_4, I_6) = \frac{\mu}{2}(I_1 - 3) + \frac{\gamma}{2}(I_4 - 1)^2 + \frac{\gamma}{2}(I_6 - 1)^2 \quad (1.10)$$

$$\underline{\sigma} = \mu \underline{F} \underline{F}^T + 2\gamma(I_4 - 1) \underline{F} \underline{N} \otimes \underline{F} \underline{N} + 2\gamma(I_6 - 1) \underline{F} \underline{N}' \otimes \underline{F} \underline{N}' - p \underline{I} \quad (1.11)$$

where μ and γ are material constants, \underline{N} and \underline{N}' are the two fiber directions defined by an angle β_1 and β_2 in the reference configuration as shown in Equation (1.12):

$$\underline{N} = \cos \beta_1 \underline{e}_1 + \sin \beta_1 \underline{e}_2, \quad \underline{N}' = \cos \beta_2 \underline{e}_1 + \sin \beta_2 \underline{e}_2 \quad (1.12)$$

and I_4 and I_6 are “pseudo-invariants” which depend on the two fiber directions and are defined by Equation (1.13):

$$I_4 = \underline{F} \underline{N} \cdot \underline{F} \underline{N}, \quad I_6 = \underline{F} \underline{N}' \cdot \underline{F} \underline{N}' \quad (1.13)$$

The constants in a strain energy function are often found by optimizing to experimental data. This parameter optimization may be done with non-linear least squares with algorithms such as Levenberg-Marquardt, dogleg, or Trust Region Reflective methods.²³⁸

The significance of this mechanical theory groundwork is that it allows for mathematical models of soft biological tissues (in the current case, for the bladder wall) which are defined in terms of the physiology. Specifically, that the mechanical stress of the bladder wall is modeled in direct relation to the measured deformations, and in some models (such as the fiber or anisotropic models), prior knowledge about the microstructure. This is the basis for the “mechanical properties” of the bladder tissue. Rather than modeling the stress and stretch relation with any arbitrary good fitting polynomial, exponential, or power function, a primary aim of the field of tissue mechanics is using deformation theory to formulate strain energy density functions that embody the phenomenology of the tissue material behavior. In essence, deformation theory shows how stresses are a direct result of material deformation, and so mechanical models are “constrained” by measured deformation, with fittable parameters which reflect the specific properties of the material in question. Although there is no “universal” mechanical model for soft biological tissues (yet) as each tissue has a unique structure and loading driving its mechanical behavior. So, it is common to use a strain energy equation that has been shown to represent the

tissue being studied, and/or to explore several models to compare their “accuracy” to a tissue. These models are standardized in tissue mechanics because they are based on the material phenomena, and the standardization allows for comparison of the material parameters across publications.

1.8 Digital 3D Reconstruction

Medical imaging has been a popular application of research on 3D reconstruction from 2D images. Digital reconstructions of tissues started in the 1980s, where preliminary work started with the spine, heart, and skull.²³⁹⁻²⁴⁵ Internal organs/tissues are primarily of interest as they cannot be observed/measured directly. Imaging methods such as sonography (ultrasound), computed tomography (CT), or magnetic resonance imaging (MRI) allow internal tissues to be visualized -- however only in 2D.

Converting 2D imaging to 3D requires solving two main problems. The first problem is differentiating the object to be reconstructed from the background. This process is called “segmentation”, as in segmenting the image into foreground and background parts. This can be done manually; however it is time consuming, tedious, and depends on a knowledgeable operator.²⁴⁶ The second problem is the actual reconstruction of these segmentations into a 3D object. This process is highly dependent on the structure of the 2D imaging data. Generally, this involves positioning the 2D data in 3D space and using some form of interpolation to generate the full 3D object. Figure 1.9 shows this process of segmentation and reconstruction.

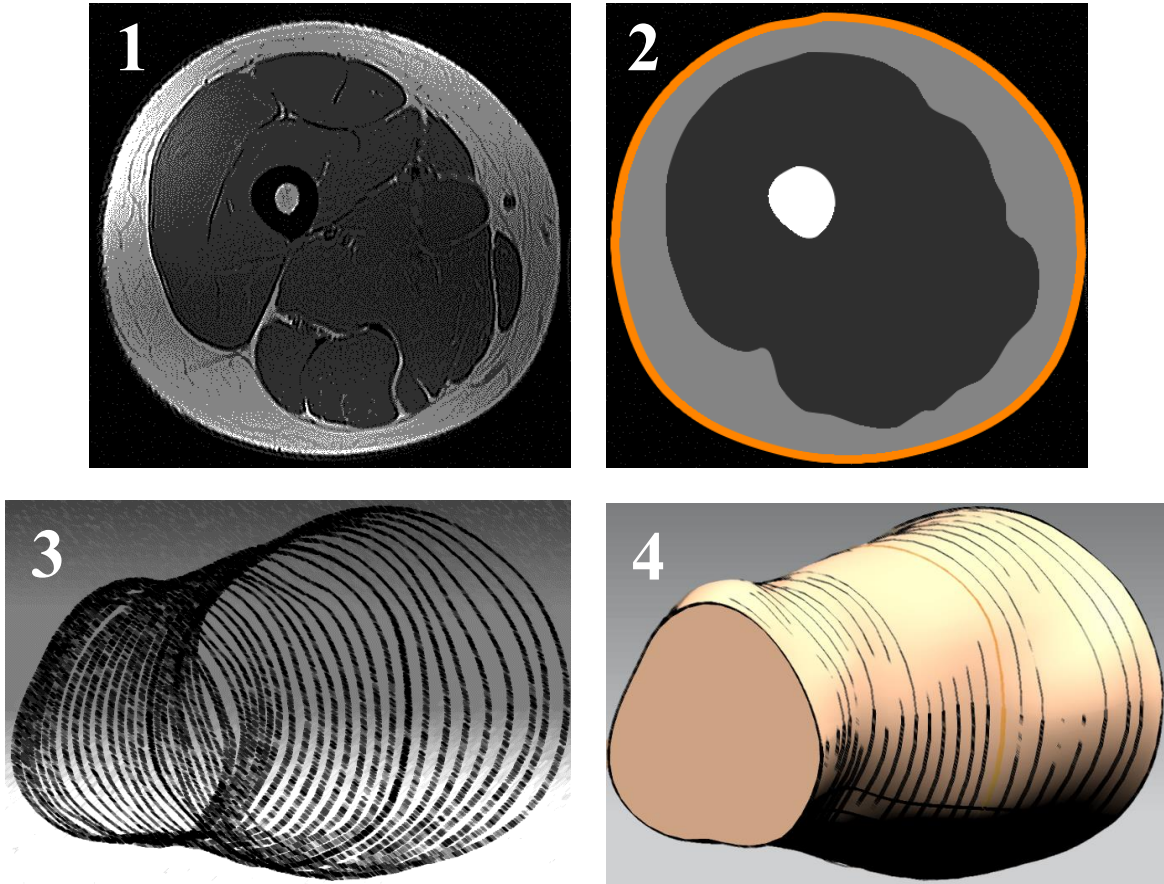


Figure 1.9: Segmentation and 2D to 3D reconstruction. 1: Original image of human thigh cross section. 2: Thigh tissue segmentation with multiple foreground segments for bone (white), muscle (dark grey), and fat (light grey). Orange outline also shows full foreground segment. 3: Stack of 2D thigh segmentations positioned in 3D space. 4: Result of interpolating 2D segments to obtain full 3D object.

The problem of converting 2D segmentations to a 3D object was the main focus of early digital image reconstruction research in the 1980s and 1990s. In the 1980s, most effort was centered on creating computational 3D structures (i.e., storing and rendering 3D data). The concept of a 3D pixel (voxel) became highly popular as an intuitive extension of the pixel.²⁴⁷ 2D images are represented as square picture elements (pixel), so the logical equivalent in 3D is a cubical volume element (voxel). The first work to transform 2D CT scans to a 3D object did so by adding depth to segmented pixels to create voxels and then stacking the voxel layers to form a 3D left ventricle.²⁴⁵ Figure 1.10 shows the results. This method of stacking segmentations is still highly

popular for reconstruction today since ultrasound, MRI, and CT are the most common sources of imaging data and they provide images in the form of slices at a certain distance interval. A significant limitation to this method is related to the Nyquist limit which constrains the spatial-resolution to the sampling rate.^{248,249} Specifically, the more precise detail you wish to obtain from wave-based methods such as MRI and ultrasound, the longer an image must be recorded. The faster an image is obtained, the more errors will be present. Overcoming this limitation is an area of significant research in signal processing for the purpose of reconstructing MRI type data.^{250–252}

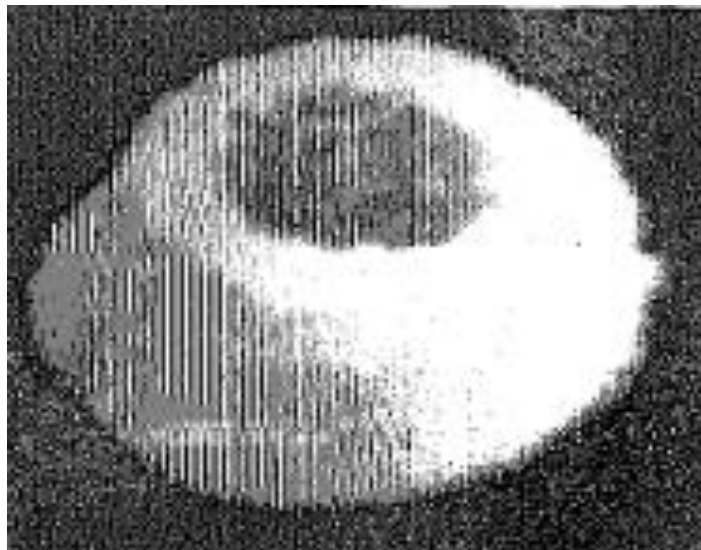


Figure 1.10: First medical digital 3D reconstruction. 3D left ventricle obtained by stacking voxel layers of segmentations. Reproduced from Herman et al. 1978.²⁴⁵

Other methods for converting 2D to 3D were also developed in the same decade. A significant method was called shape-from-silhouette or volume carving.^{253–255} This method is useful in cases where the 2D images are obtained from different orientations and are not planar as in CT slices. It also requires fewer images of the object for reconstruction. In many cases, an image of the object from the top, side, and front views is enough to describe the 3D shape.²⁵⁴ Shape-from-silhouette, as the name implies, uses the silhouettes of the object from different perspectives to carve out the 3D object. Figure 1.11 illustrates how complex shapes can be reconstructed from only 3 images. Numerous other methods of reconstruction emerged that leverage lighting and color information, although these significantly increase complexity and are less useful in medical imaging, which is often grayscale.²⁵⁶ This method has benefits over traditional medical imaging

techniques, as the resolution and sampling frequency of video cameras are still bound by the Nyquist limit, but video cameras are able to achieve higher resolutions and frame rates compared to MRI due to their comparatively reduced complexity.^{257,258} The challenge is that the object of interest must be completely isolated (*ex vivo*) to accomplish the imaging, whereas MRI has the benefit of providing internal imaging.

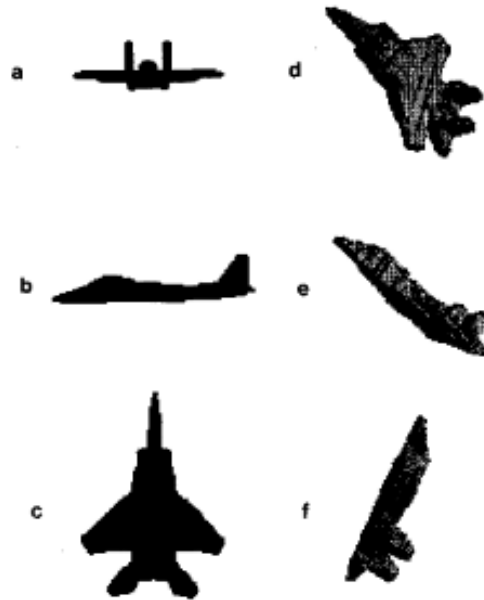


Figure 1.11: Shape-from-silhouette method for 2D to 3D reconstruction. Left side shows three orthogonal segmentations of the object. Right side shows the 3D object reconstructed from only these three images. Reproduced from Chien et al. 1986.²⁵⁴

As digital reconstruction research continued into the 1990s, work next focused on storage and rendering of surfaces rather than voxel volumes. Surfaces were desired over voxels for saving disk space and for aesthetic reasons.²³⁹ One method emerged that efficiently converted voxel volumes into surface meshes, called “marching cubes”.^{259–261} This algorithm scans the entire surface of the voxel volume, and uses a lookup table for all possible 2×2 orientations of voxels to determine a corresponding triangular surface. The original paper presented the results of the algorithm to reconstruct surfaces of the skull, heart, and soft tissue of the head, and was later used to reconstruct the entire human body.^{259,262} The marching cubes algorithm was later improved when it was shown that the lookup table was incomplete.^{260,261} The original algorithm mapped only 15 voxel configurations, which resulted in multiple triangular solutions in certain cases. The

improved version was extended to 33 configurations and has been shown to resolve the multiple solution ambiguities of the original algorithm. Another popular method for surfacing is called variational, where the surface is guided by the voxel volume and an objective function to produce a higher quality surface. Variational reconstruction is typically guided by Voronoi tessellation^{263–265} or a 3D extension of Delaunay triangulation.^{266–269} Variational reconstruction produces meshes that are suited for finite element modeling (FEM) at the cost of higher complexity and computation.

More recently, research efforts have shifted to focus on segmentation. In the past, computation was costly and more prohibitive than the labor of manual segmentation. Now, there are a variety of 2D to 3D methods and computation is cheap.²⁷⁰ Manual segmentation is now the limiting factor, and so automated segmentation has become the primary focus. Automated segmentation is approached in two main ways: classic image segmentation or machine learning.

The first way relies on classical image analysis methods such as boundary detection via image gradients, enforcing smoothness, connectivity, and symmetry, and growth/search algorithms.^{245,271} This way is simple, logical, and formulaic. Although because it is so formulaic, it is difficult to adapt when it produces erroneous results. The algorithms are so hyper-tuned to a dataset that they do not deal well with noise, outlier data, or completely fail when applied to similar-but-different data.^{272,273} Generally, segmentation via classical image analysis is only reliable for very clean, uniform, and predictable data.^{274,275}

The second way to automate segmentation is with advanced machine learning algorithms. These algorithms have significantly increased in popularity and in the last five years used by many researchers to segment the bladder.^{276–283} These algorithms are more robust and reliable than classic image segmentation algorithms, although they are essentially “black boxes”, require significant data and expertise to implement, and are better but still weak when applied to similar-but-different data.^{272,273} In traditional image analysis segmentation, the precise steps map a raw image to the segmentation are strictly specified and known to the researcher. Conversely, in implementing a machine learning method, the algorithm is shown the raw images, and the corresponding expected output segmentation, and the steps in-between are not specified by the researcher. Instead, the algorithm “learns” the image manipulation steps to transform the raw image into the segmentation.

The steps the machine learning algorithm “learns” and use can be more generalizable than classic image techniques, however they are not translatable to human interpretation. In the case of

neural networks, which are the type of machine learning model most often applied for image processing, the transformation between raw and segmented image is a highly interconnected network of “neurons” which transform the data using their learned activation criteria.²⁸⁴ Examining the inner workings of a trained neural network would only reveal a large network of weight and bias values for each neuron having virtually no real-world interpretability, and as such their image transformation methods are black-box like. Although a well suited machine learning algorithm can provide highly accurate results (95%+).²⁸⁵ When the expected output is largely achieved, not understanding how the output was obtained is an accepted trade off. The expertise and amount of data required to develop a machine learning algorithm cannot be understated. However, their power for data processing is increasingly proven to be useful, especially for the medical imaging field.^{272,273,275} Machine learning methods are developed as a part of this dissertation for the purpose of image segmentation, and will be employed in Chapter 2. Examples of 3D bladder reconstruction which employ segmentation are explored next.

Bladder 3D reconstruction is most commonly done to estimate bladder volume/capacity. A common and easy method for reconstruction in humans is with proprietary equipment and software.^{102,286–289} Ultrasound machines from companies, such as GE and Phillips, can be used with their proprietary software which reconstructs the bladder in 3D from the scanning device (shown in Figure 1.12). Researchers have also commonly used custom algorithms to generate 3D bladder from 2D sources such as MRI, CT, or ultrasound (shown in Figure 1.13).^{97,98,101,104,278,290–292} Other novel methods for bladder reconstruction in humans includes surface mapping via internal endoscope^{293,294} and reconstruction via electrical impedance tomography.²⁹⁵ Digital reconstruction of the bladder has also been done in animal models including pigs, rats, and mice with similar methods *in vivo* but also more novel methods *ex vivo*.^{95,99,296}

As discussed earlier, a significant limitation to these techniques is the spatiotemporal resolution in addition to the need for costly medical imaging equipment. In particular, MRI is slow to obtain the images, and only provides good detail in a single plane, with space and time between subsequent image slices. Ultrasound suffers from the same limitations. There is a need for improved imaging methods to study the bladder geometry at higher space and time resolutions. In this dissertation, a novel low-cost imaging method is used to develop high-accuracy geometrical models of the mouse urinary bladder with high spatiotemporal accuracy.

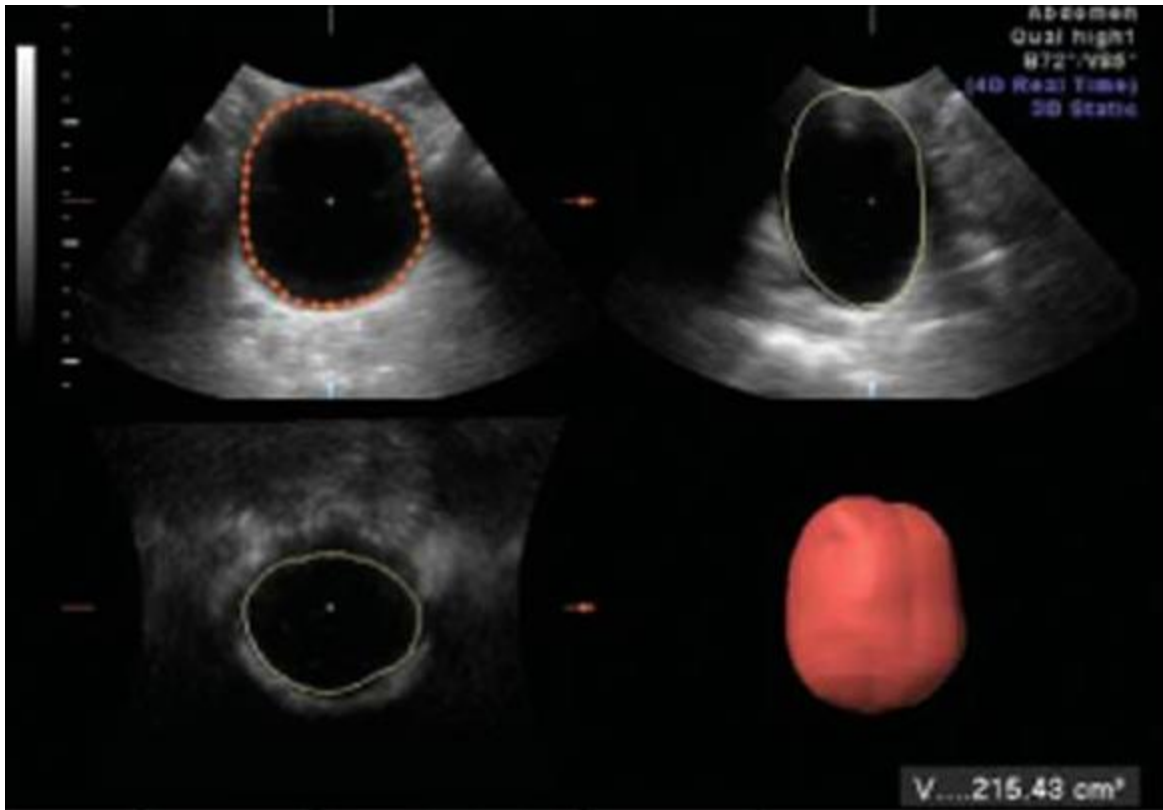


Figure 1.12: Bladder reconstruction from ultrasound via General Electric’s proprietary reconstruction software VOCAL+4D view. Reproduced from Hirahara et al. 2006.¹⁰²

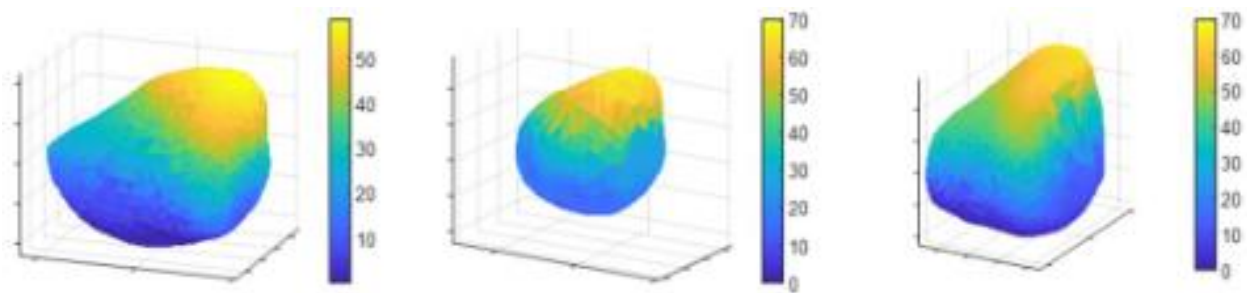


Figure 1.13: Bladder reconstruction via custom algorithms from MRI Reproduced from Pewowaruk et al. 2020.¹⁰¹

CHAPTER 2

MODELING BLADDER MECHANICS WITH 4D RECONSTRUCTION OF MURINE EX VIVO BLADDER FILLING

2.1 Introduction

The urinary bladder is a highly deformable organ with complex mechanical behavior. During filling, the bladder undergoes large stretches while maintaining low pressures. When the organ approaches its elastic limit, the pressure increases significantly and a signal alerts the brain of the need for voiding.^{297,298} Healthy bladder function is poorly defined.⁶⁵ There is a need for more mechanical testing and analysis in order to characterize the healthy bladder as a starting point to understanding the broad category of bladder dysfunctions.

Bladder mechanics are sophisticated in that the bladder wall tissue can be described as a viscoelastic, anisotropic, and inhomogeneous material. These characteristics arise from the bladder wall's complex microstructure, which is tuned to allow the organ to undergo large deformations within a duty-cycle on the order of hours. Better mechanical models that fully capture the sophisticated mechanics of the urinary bladder are needed. It is indeed difficult to capture physiological bladder behavior in terms of its mechanics. Bladder tissue is often tested *ex vivo* to quantify its mechanical properties. The type of mechanical tests available, such as uniaxial or biaxial testing, often require of the tissue to be sectioned before testing.^{113,145,146} While these methods can be useful for characterizing the material, they arguably do not reflect the physiological loading condition the organ undergoes as a whole *in vivo*. From the opposite perspective, *in vivo* bladder pressurization via catheterization is another often used method which gives insight to the function of the organ.^{112,139–142,144} However, quantifying the mechanics with this experimental setup then becomes challenging as accurate mechanical models become more complex compared to tensile testing. There are some novel methods with human, pig, and rat models which were able to quantify mechanics of the pressurized bladder, although these methods of modeling whole-organ bladder mechanics is limited in the literature.^{99,104,148} Knowing this, it is apparent that whole-organ level mechanical modeling of the bladder needs to be further developed to quantify deeper mechanical measures which can be related to organ function.

The most common method for modeling mechanics of the bladder at the organ level is with a thin-walled spherical pressure vessel model.^{72,73,80,82,129,186,213–216} This method uses the thin-

walled assumption with Laplace's law²¹⁸, which asserts that wall tension is proportional to the internal pressure times radius of the vessel. This model is indeed useful due to its simplicity, and it can give similar results to more complex models.²²¹ However, it is still reductive and obfuscates underlying mechanics, such as anisotropy and inhomogeneity, which may be important to understanding the nuances of this organ's behavior. On the other hand, more complex models are not trivial to develop. Implementing non-spherical models requires significantly more data and expertise. As such, work to model bladder mechanics in 3D is often low-resolution in space or time, requires extensive labor, or is cost-prohibitive.^{299,300}

The work here presents a method for mechanical modeling of whole-organ mechanical testing under physiological loading conditions. This work aims to generate datasets for spatially and temporally accurate modeling of the unique tissue mechanics of the urinary bladder. This methodology leverages high-frequency imaging of bladder pressurization with computer vision algorithms to allow for meticulous analyses of geometry and wall stresses from empty to full capacity. This 3D model is compared to the spherical model and the differences and similarities are discussed. Furthermore, the data processing and modeling steps are compiled into a highly automated pipeline which uses data from a low-cost experimental setup.⁶⁷ As such, this work expands our knowledge about the healthy bladder in mice using a novel methodology which is able to generate deeper mechanical models in a highly automated way.

2.2 Methods

All experimental procedures were reviewed and approved by IACUC at Michigan State University. Data were collected from 8 male C57BL/6 mice ages 10-12 weeks old. The complete experimental protocol has been previously described.⁶⁷ Briefly, the bladder was extracted and tested on a custom Pentaplanar Reflective Imaging Microscopy (PRIM) device illustrated in Figure 1 of Hennig et al. 2022.⁶⁷ Each bladder was cannulated in the device and pressurized with three loading-unloading cycles to allow for tissue acclimation. Bladders were filled to a maximum luminal pressure of 25 mmHg at a constant rate of 30 μ L/min. Internal bladder pressure was measured via pressure transducer and synchronized with video imaging, each at a rate of 10 Hz.

The data from the last filling cycle for each bladder was analyzed. All data was processed with *Python 3.7.9* and custom code. Data collected and analyzed included synchronous recording of luminal bladder pressure measurement and video imaging. From each test, data was subsampled

at 0.5 mmHg pressure steps from 0 mmHg to 25.5 mmHg (52 data points for each bladder). For each pressure step desired, the pressure value nearest to the step in the data was used.

The shape-from-silhouette method^{253–255} was used to generate bladder 3D reconstructions at all time points in the subsampled data. Initially, the image data showed 5 views of the bladder.⁶⁷ However, only three orthogonal silhouettes were essential for this reconstruction method, and the two remaining silhouettes were redundant.²⁵⁴ First, silhouettes were obtained by masking three orthogonal bladder views from the background in the image data (Figure 2.1). A U-Net machine learning model³⁰¹ was employed for this binary segmentation task. The U-Net architecture was sourced from an open-source implementation³⁰² and trained on our dataset. For training the neural network, 1,500 individual bladder images were collected from the complete video data, and corresponding segmentation masks were created manually. The training dataset did not intersect with the subsampled data. Data augmentation allowed the dataset to be expanded to 12,000 image-mask pairs via rotations and cropping. The augmented dataset was split 80% for training and 20% for validation with random selection. To optimize the model’s performance for this specific application, various hyper-parameter combinations of learning rate and weight decay were explored. The best model was selected based on lowest training and validation errors, convergence without over-fitting or under-fitting, as well as qualitative assessment of model segmentation results. Final segmentations were reviewed and manually repaired when necessary, before the next steps of the analysis.

Next, the 3D bladder shapes were obtained from the volume intersection of the three orthogonal silhouettes at each time point (Figure 2.2). For each instance of reconstruction, a 3D array with dimensions corresponding to the silhouettes was initiated and populated with ones as $V'(i, j, k) = 1$ (Figure 2.1b). Let $S_x(y, z)$, $S_y(x, z)$, and $S_z(x, y)$ be the binary silhouettes projected on the planes normal to the x-, y-, and z-axes, respectively. The silhouettes allocate a value of 1 to the portion of the image occupied by bladder tissue, and a 0 to the background. Each axis of the V' array was then multiplied by its respective silhouette. Specifically, S_x and S_y were first multiplied element-wise on the array by $V'(i, j, k) \cdot S_x(j, k) \cdot S_y(i, k)$ (Figure 2.1c). However, to overcome the visual hull effect³⁰³, S_z was dynamically modified for each z-axis layer of the array. For each layer k along the z-axis, the bladder cross-section created by S_x and S_y was identified, and S_z had its silhouette region rescaled to correspond to the cross-section dimensions. The rescaling step effectively eliminated sharp corners in the final shape which are inherent to

shape-from-silhouette volume carving from three perspectives. Obtaining the final bladder volume shape can be expressed by Equation (2.1):

$$V(i, j, k) = V'(i, j, k) \cdot S_x(j, k) \cdot S_y(i, k) \cdot S_z^k(i, j) \quad (2.1)$$

where S_z^k be the rescaled S_z for layer k and $V(i, j, k)$ is a 3D array containing ones where there exists bladder volume, and zeros where there exists empty space. This process gave a voxel representation of the bladders at each subsampled time point. Measure of the volume occupied by the bladder in voxels was obtained by multiplying the total sum of the array by the cubed pixel-to-mm scale factor, which is $2.62 \cdot 10^{-4}$ for this specific system.

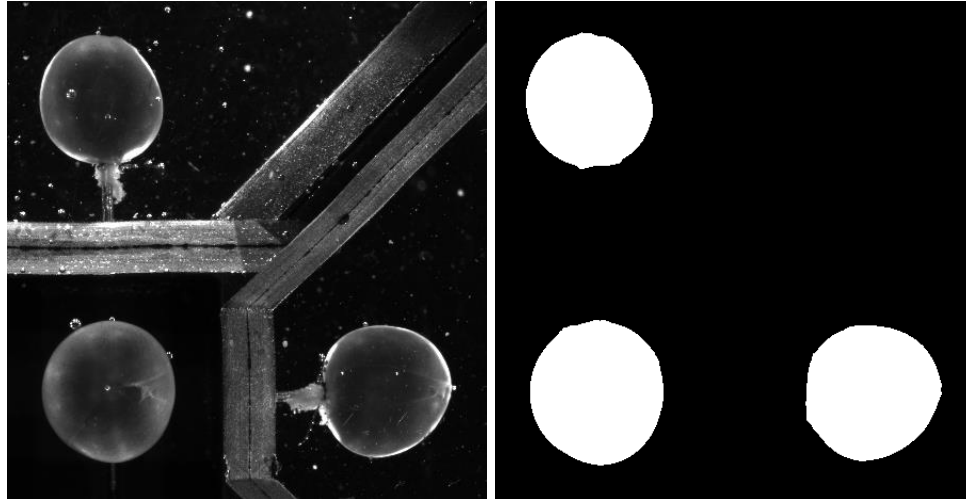


Figure 2.1: Representative result of binary segmentation on three perspectives of the bladder in one image.

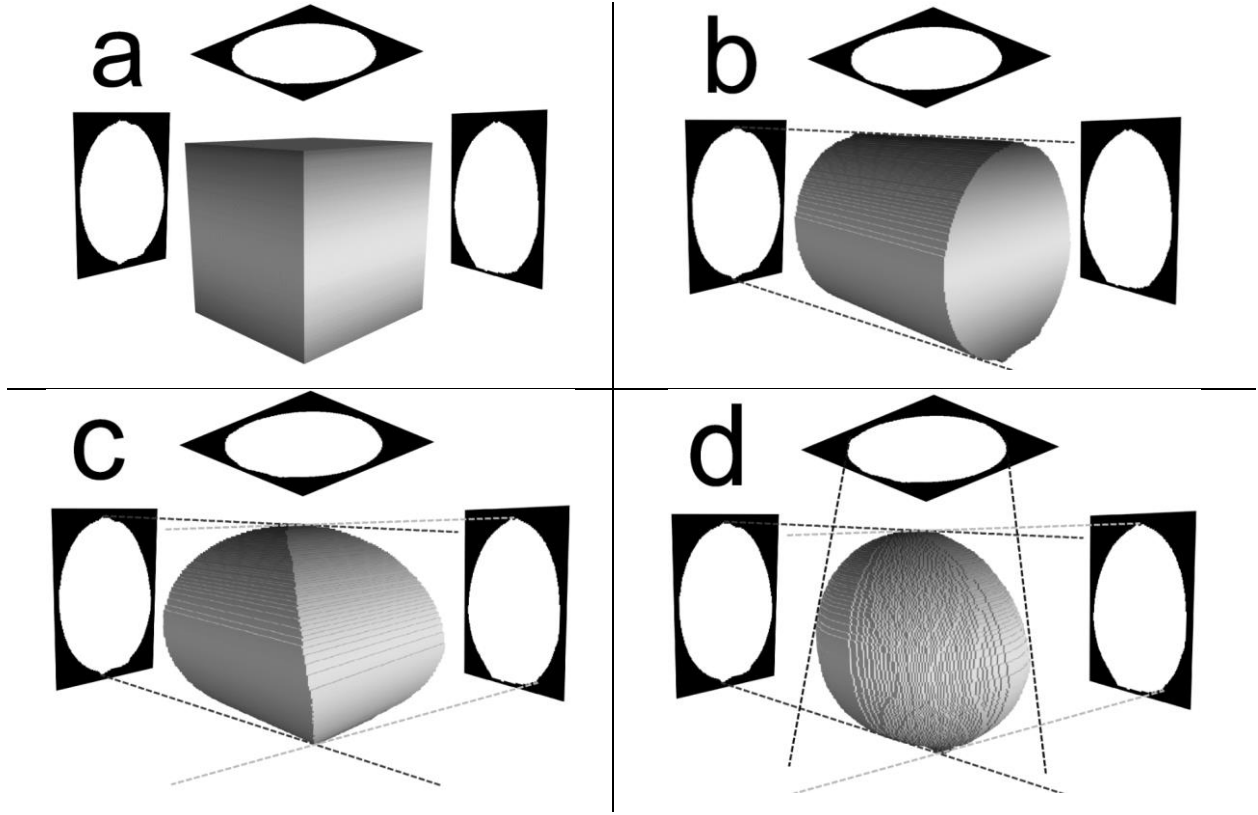


Figure 2.2: Shape-from-silhouette method. a) Silhouettes are projected on their respective axis and solid primitive is initialized. b) Side silhouette is used to carve solid. c) Second side silhouette is used to carve. d) Top silhouette is applied to complete carving.

Finally, the voxellized bladder reconstructions were transformed into triangular surface meshes using a marching cubes algorithm.^{261,304} This allowed the tissue surface to be represented with 3D point coordinates in space, rather than an array. To improve the quality of the mesh generated by the marching cubes algorithm, the outer surface of the bladder in the voxel array was labeled first. In essence, for each reconstruction, each voxel which did not have an empty voxel in its 26 neighbors was deemed a non-surface voxel and had its value incremented. More specifically, a new 3D array was initialized as $V_s(i, j, k) = V(i, j, k)$. Then, for each solid voxel, where $V(i, j, k) = 1$, the sum of values in its $3 \times 3 \times 3$ neighborhood, was computed as Equation (2.2):

$$\Sigma(i, j, k) = \sum_{a=-1}^1 \sum_{b=-1}^1 \sum_{c=-1}^1 V(i + a, j + b, k + c) \quad (2.2)$$

V_s was then updated such that $V_s(i, j, k) = 2$ if $\Sigma(i, j, k) = 27$. This resulted in V_s being zero where there is empty space, one at outer surface of the bladder, and two inside the bladder. The marching cubes algorithm was then used to generate surface meshes for each voxel array at the boundary, i.e., where $V_s(i, j, k) = 1$. Constructing V_s allowed the algorithm to generate meshes with nearly half the number of vertices and faces and minimal topological differences compared to running the marching cubes algorithm on the binary V array. Note that the V arrays were padded with zero on all sides to ensure Equation (2.2) is always valid, and to provide the marching cubes algorithm a clear transition boundary to develop the surface from. As a last step, the meshes, which were originally quite faceted, were smoothed with Laplacian smoothing^{305,306} using a lambda of 0.9 and 50 iterations.

After creating surface meshes for the data of interest (i.e., all bladders at subsampled time points), several metrics for assessing the shape of the bladders were obtained. These include: fitting an effective sphere, sphericity³⁰⁷, and principal curvature.

The radius of the effective sphere was obtained by minimizing the difference between the surface mesh vertex points of the reconstructed geometry and a sphere. The general equation to describe the surface of a sphere centered at the origin is $x^2 + y^2 + z^2 = a^2$ where a is the sphere radius. The radius of the best fitting sphere, \bar{a} , can be calculated analytically as the average distance of all vertices on the mesh surface from the centroid. To simplify this process, the meshes were translated such that their centroid was aligned with the coordinate system origin. Thus, for N vertices on a mesh, the distance from the origin was found as $d_i = (x_i^2 + y_i^2 + z_i^2)^{1/2}$ and the effective radius was

$$\bar{a} = \frac{\sum_{i=0}^N d_i}{N} \quad (2.3)$$

To calculate the goodness-of-fit for the sphere we quantified a surface deviation parameter as the root-mean square deviation (RMSD) of d_i and \bar{a} of the fitted sphere as

$$RMSD = \sqrt{\frac{\sum_{i=1}^N (d_i - \bar{a})^2}{N}} \quad (2.4)$$

Sphericity³⁰⁷, a measure of how spherical a surface is, is defined as a ratio of volume V and surface area A as

$$\Psi = \frac{\pi^{1/3}(6V)^{2/3}}{A} \quad (2.5)$$

Both of these metrics can be interpreted as quantifying how spherical the bladder surfaces were. The RMSD of the best fitting sphere provided a more localized assessment since it is based on specific surface irregularities at each point in a mesh. Sphericity gave a more global assessment of the surface since it derives from the total volume and surface area.

Principal curvatures of each surface mesh (i.e., κ_1 and κ_2) were quantified using an established algorithm.^{308,309} In short, at each vertex in a mesh, a local quadric surface is fit to nearby vertices and the principal curvatures of the quadric were found with differential geometry. Essentially, the eigenvalues and eigenvectors of the negative differential of the fitted quadric surface's normal vector field give the principal curvatures and principal directions at the vertex.³¹⁰ Quantifying curvature of the bladder surface provides localized geometrical data, as well as informing a non-spherical mechanical model of pressurization.

Mechanical analyses were formulated for the full 3D meshes and the spherical approximation. Generally, at each point, the Cauchy stress tensor is defined as

$$\underline{\sigma} = \begin{bmatrix} \sigma_r & 0 & 0 \\ 0 & \sigma_1 & 0 \\ 0 & 0 & \sigma_2 \end{bmatrix} \quad (2.6)$$

where σ_r is the principal stress in the radial direction, and σ_1 and σ_2 represents the principal stresses along the in-plane principal directions defined at each point. For a thin-walled, axisymmetric membrane with negligible bending stiffness, we can define the principal stresses following the generalized Laplace's law³¹¹ as

$$\sigma_r = -\frac{P}{2}, \quad \sigma_1 = \frac{P}{2h'\kappa_2}, \quad \sigma_2 = \frac{P}{h'\kappa_2} \left(1 - \frac{\kappa_1}{2\kappa_2}\right) \quad (2.7)$$

where κ_1 and κ_2 are the in-plane principal curvatures, P is the luminal pressure, and h' is the wall thickness in the current configuration. Principal curvatures κ_1 and κ_2 were found as described previously.

The effective sphere was also used to model the mechanical stresses under the spherical approximation with Laplace's law. In this case, the principal stresses become

$$\sigma_r = -\frac{P}{2}, \quad \sigma_1 = \sigma_2 = \frac{Pr'_{mid}}{2h'} \quad (2.8)$$

where r'_{mid} and h' are the mid-wall radius and wall thickness calculated for all subsampled time points (i.e., current configuration). The method for quantifying wall thickness is described in the Supplementary Material section. The von Mises stress σ_v was also calculated as

$$\sigma_v = \sqrt{\frac{1}{2}[(\sigma_r - \sigma_1)^2 + (\sigma_r - \sigma_2)^2 + (\sigma_1 - \sigma_2)^2]} \quad (2.9)$$

2.3 Results

The bladder volumes quantified using this novel method of 3D reconstruction were validated by comparison to experimental parameters and a manual volume estimation. Specifically, the volume of the 3D bladder meshes was highly linearly dependent upon time, which is in agreement with the constant infusion rate employed during the experiments. Figure 2.3a shows the reconstructed volume for each bladder as a function of time during filling. The best fit line was found to have a slope of 25.13 $\mu\text{L}/\text{min}$ while the experimental slope (i.e., infusion rate) was 30 $\mu\text{L}/\text{min}$. Figure 2.3b shows the comparison between the volumes obtained from this reconstruction method to the volume obtained with a manual method, as previously described in Hennig et al. 2022.⁶⁷

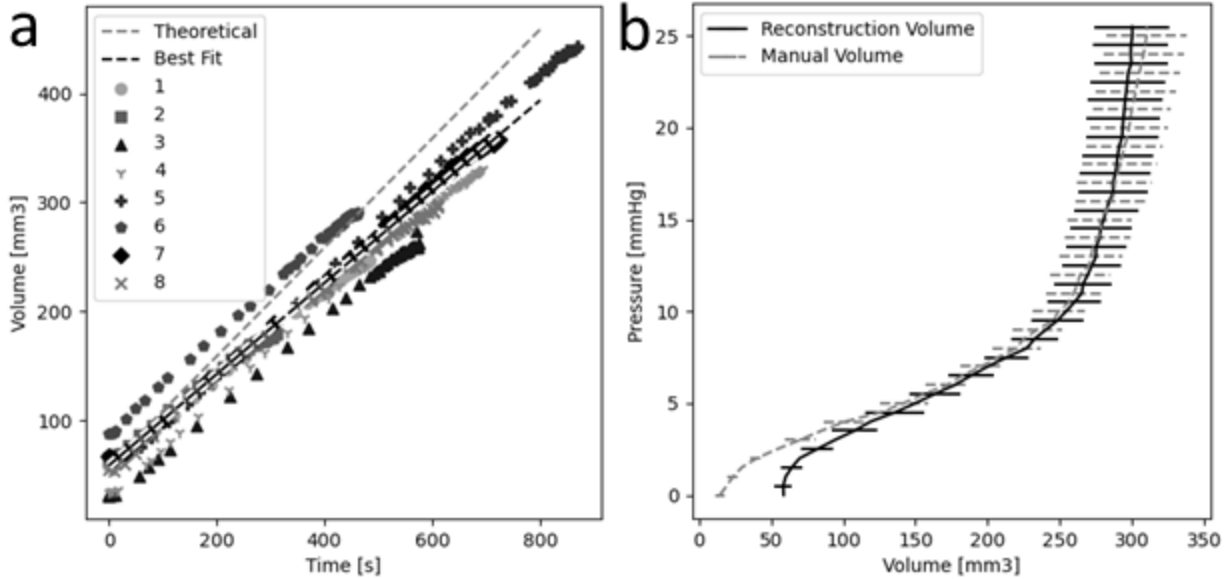


Figure 2.3: a) Reconstructed bladder volume over time from 0 mmHg to 25 mmHg internal bladder pressure. Experimental fill rate was 30 $\mu\text{L}/\text{min}$ (gray line), and the average fill rate observed from volume reconstruction was 25.13 $\mu\text{L}/\text{min}$ (black line). The best fit line had an R^2 of 0.96, and RMSE of 20.74 μL . b) Pressure-Volume plot for the volume obtained from the reconstruction method, and a manual method by which final volume was estimated by measuring ellipsoidal axis lengths in the images, and all other volumes were based on the constant infusion rate.⁶⁷ Standard errors shown.

This reconstruction method leads to a more accurate description of the bladder geometry. Figure 2.4a illustrates the 3D mesh geometry overlaid on the effective sphere, for a representative bladder at luminal pressure 25 mmHg. This figure highlights how the shape of the bladder can deviate quite significantly from the effective sphere, even if the difference between the two volumes is small. The average difference between the 3D bladder mesh volume and effective sphere volume across samples was 4.93 mm^3 for all pressures, and 6.05 mm^3 at 25 mmHg. Figure 2.4b shows the RMSD of mesh geometry from the effective sphere for all samples, as a function of luminal pressure. For most samples, the RMSD was largest at low pressures, and the spherical approximation became more accurate as the pressure increased.

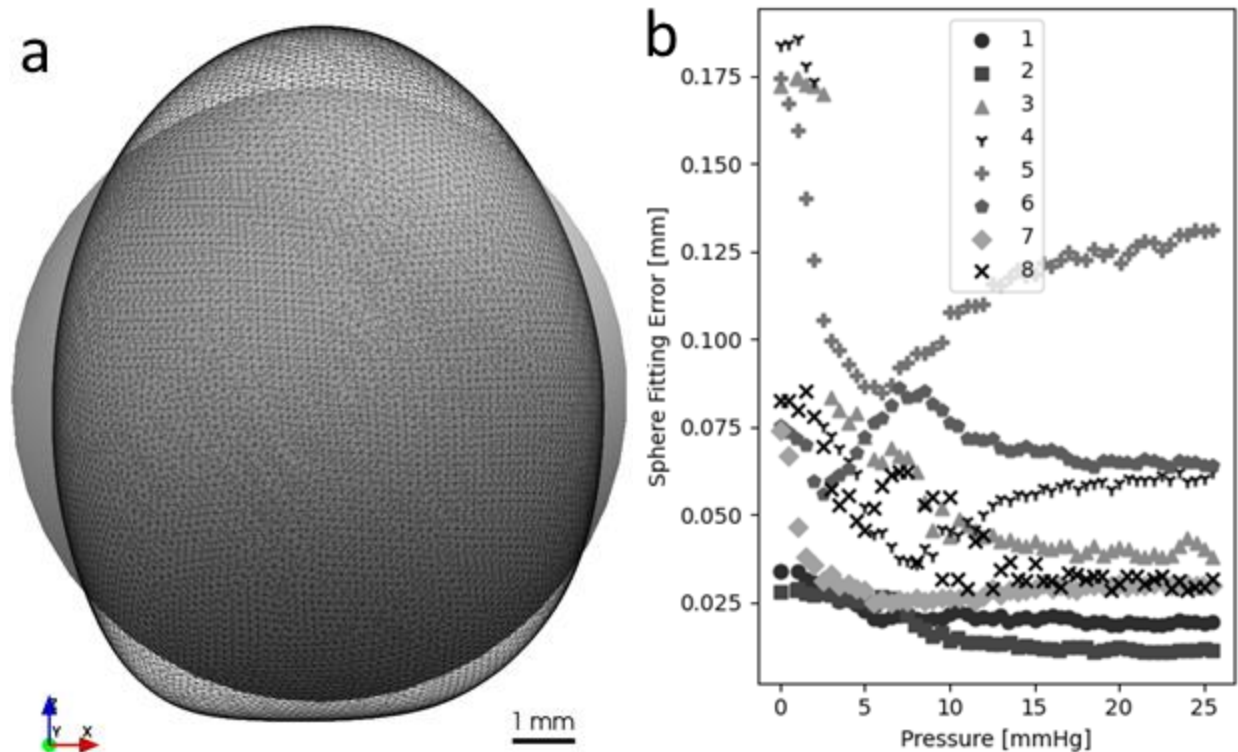


Figure 2.4: A) Wireframe mesh of a reconstructed bladder #5 at 25 mmHg pressure overlaid with the fitted sphere for this geometry. The sphere may be able to approximate the volume as the average difference between mesh and sphere volume was 4.93 mm^3 , however the reconstruction gives more accurate geometry. B) Effective sphere RMSD. Error was defined as the average distance between the best fitting sphere surface and the reconstructed surface. Sphere error generally decreased with pressure.

Analyzing sphericity also revealed that, at low volumes, the bladder is poorly approximated by a sphere (Figure 2.5).

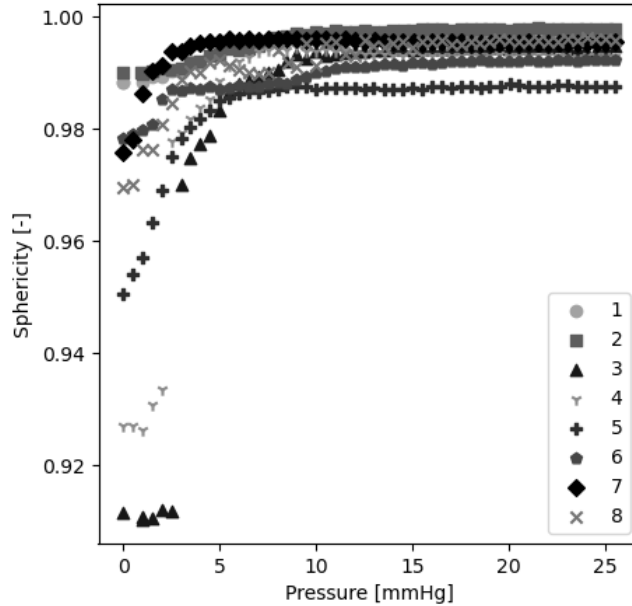


Figure 2.5: Sphericity of bladder reconstructions throughout pressurization. Low pressures had the lowest sphericity across all samples before plateauing.

The stress analysis formulated using the 3D reconstruction provides a novel location-specific mapping of the bladder wall stress. To better visualize the stress distribution, the 3D bladder surface was flattened to 2D. The highest z-coordinate in the mesh (i.e., the dome) was set as the origin, and the distances to all other vertices on the mesh were calculated using an established algorithm.³¹² The mesh vertices were then remapped to the 2D representation at their respective distance and angle relative to the dome. For the following figures, the origin of the plot corresponds to the bladder dome, and the outer circumference corresponds to the bladder neck. Figure 2.6 illustrates this remapping and gives the stress map as pressure increases from 5 mmHg to 20 mmHg, and the respective 3D representations. From these plots, it can be seen that the stress distribution is non-uniform over the surface, but the non-uniformity is preserved with increasing pressure. Figure 2.7 shows the mapping of the principal in-plane Cauchy stresses, the von Mises stress, as well as the spherical approximation for comparison. This representation allows appreciation of how both the in-plane principal stresses, as well as the von Mises stress varies in a localized manner. This in contrast to the spherical model, in which the stress is uniform across the entire surface, shown by Figure 2.7.

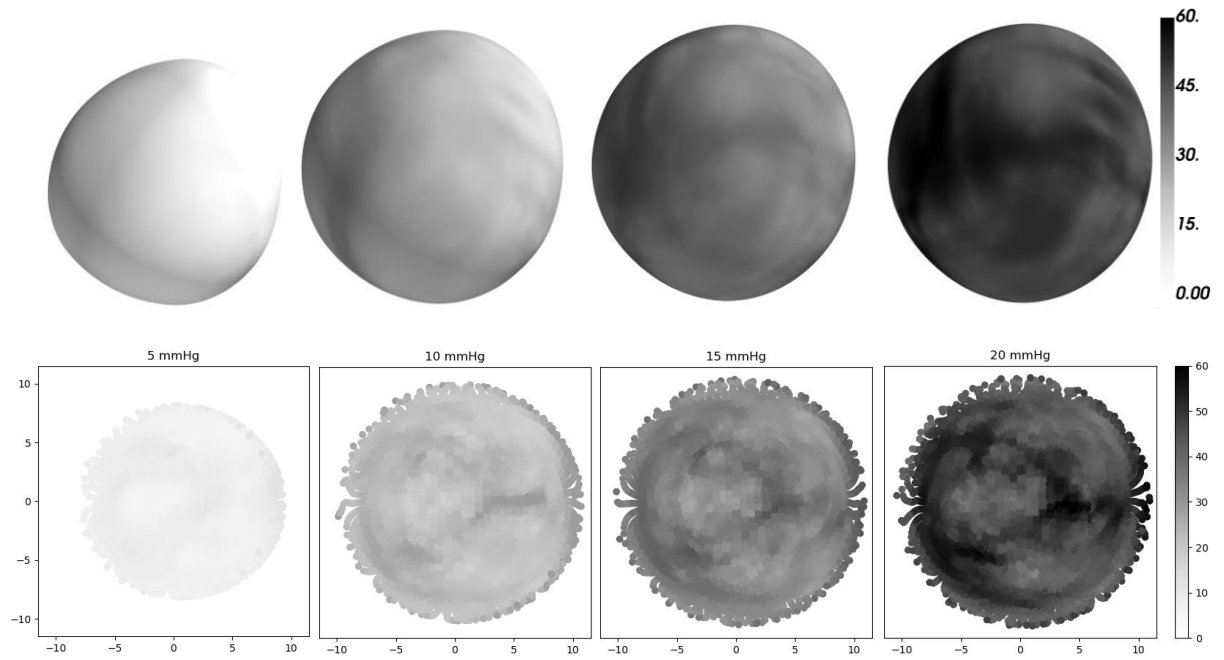


Figure 2.6: von Mises stress distribution for a bladder at 5, 10, 15, and 20 mmHg. Top) 3D mapping of the stress distribution on the bladder surface. Bottom) Equivalent stress distribution displayed in 2D. The 3D vertices were flattened such that the center of the plots corresponds to the dome of the bladder, and the outer circumference corresponds to the bladder neck. Axes are mm. Scale bar is in kPa. Same stress scale.

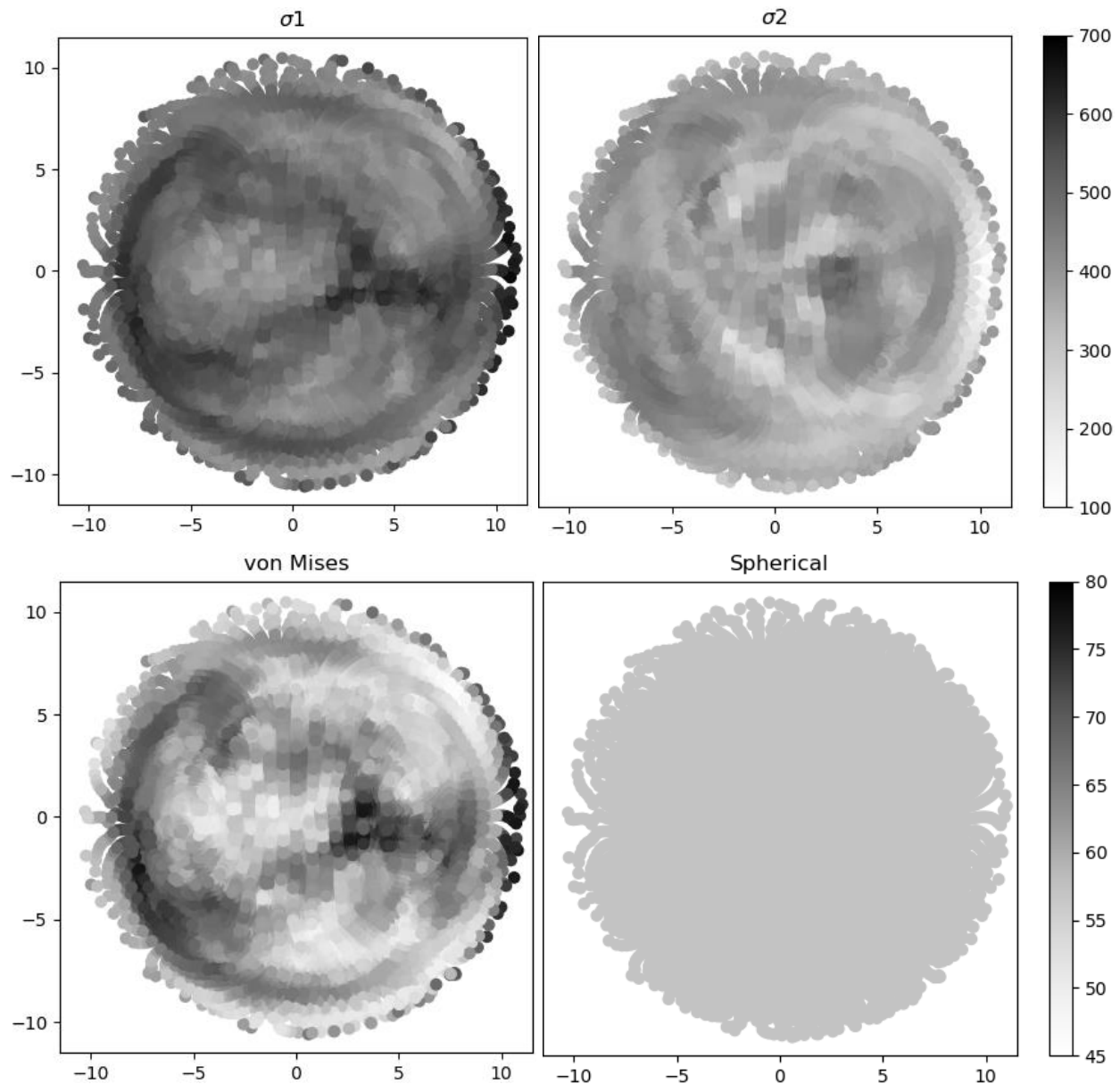


Figure 2.7: Stress distribution on a bladder surface at 25mmHg. Principal stresses, von Mises stress, and spherical stress shown. Spherical stress was 57.29 kPa, while the average von Mises stress over the surface was 60.35 kPa. The 3D vertices were then flattened such that the center of the plots above corresponds to the dome of the bladder, and the outer circumference corresponds to the bladder neck. Axes are mm, scale bars are kPa. This is a 2D remapping of the 3D bladder surface/stresses. The 3D mesh vertices were remapped to the 2D representation at their respective distance and angle relative to the dome. The origin of the plot corresponds to the bladder dome, and the outer circumference corresponds to the bladder neck.

From these stress maps, it was found that stresses were highest near the bladder neck (outer circumference of the plots in Figure 2.7), and across the rest of the surface, the stress distribution was non-uniform. Although, it was also found that when the von Mises stress over the entire surface was averaged, the result was on the same magnitude as the uniform spherical stress at the same pressure. This is illustrated below by Figure 2.8a.

The ratio of σ_1 to σ_2 provides more insight into the distribution of stresses in the bladder wall. Figure 2.8b illustrates this ratio for a bladder at 25 mmHg. It was found that the distribution of stresses visualized this way was not uniform, with potential stress concentrations around the bladder neck and around the dome.

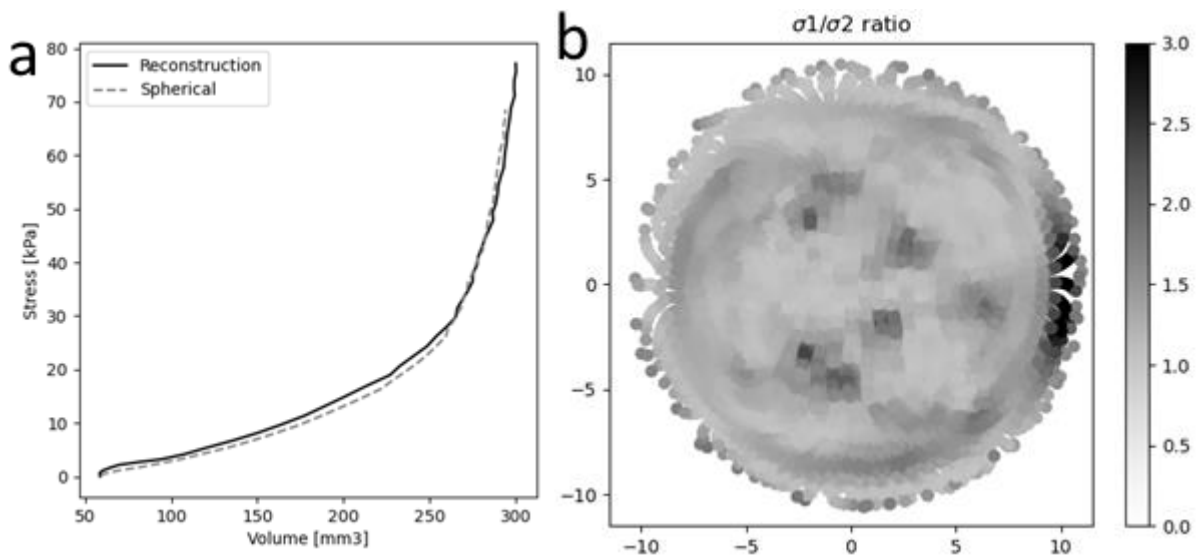


Figure 2.8: a) Volume vs stress averaged across pressures. Reconstruction data is the average Von-Mises stress across the entire surface vs the reconstructed volume. Spherical data is the spherical volume vs the spherical volume. Results shown are averaged over the pressures from 0 to 25 mmHg. b) Ratio of σ_1 to σ_2 for a bladder at 25 mmHg. The ratio was non-uniform. Axes in mm.

2.4 Discussion

The method of reconstruction proved to be accurate based on the linear volume results shown by Figure 2.3a. Volume reconstruction allows the actual shape and deformations of the bladder wall to be analyzed. Shape analysis presented here showed that the spherical model is more accurate at higher pressures, but less accurate at lower pressures. When the bladder is at a low volume/pressure, the organ can appear more collapsed which leads to a more non-spherical shape, and may even be non-convex. Furthermore, Figure 2.4B shows that the bladder is more poorly approximated by a sphere at low pressures, but approaches a more spherical shape as pressure/volume increase. Quantifying bladder shape may be relevant as a non-spherical bladder may indicate functional deficiencies or irregularities in the bladder wall microstructure. Tissue stiffening, as seen in bladder fibrosis, can also alter the elasticity of the tissue and drive non-spherical deformation. A non-spherical bladder may also present altered emptying characteristics compared to a more spherical bladder.^{102,106,313} Furthermore, diseased conditions such as diabetes have shown increased bladder capacity, and can present altered bladder shapes compared to healthy subjects.^{314,315} Although this work does not include a model of bladder dysfunction, the methodologies demonstrated here lay the groundwork for assessing dysfunction in terms of the mechanical behavior of the healthy bladder. The literature is lacking in consensus data on measures of bladder health, and deeper understanding of the bladder mechanics may be the bridge to this gap.

Mechanical stress in the bladder wall was modeled via the local curvature of the reconstructed volume, and also via Laplace's law as a thin-walled spherical pressure vessel. The results of both stress models were of the same magnitude. The agreement between the two models indicates that the spherical approximation is comparable to the average wall stress based on surface curvature. However, the spherical model can only provide an average uniform stress across the entire surface. Modeling the stress using local curvature allows the wall stresses to be discretely mapped over the entire surface which can be of value to study the anisotropic behavior observed in bladders.

Comparing the pressure-volume results shown by Figure 2.3B, the methods of estimating bladder volume via a manual method and the reconstruction method showed significant overlap. This validates the reconstruction method with a method that is commonly used to estimate bladder volume in the clinical setting.³¹³ There was some difference at low volumes, which is likely due

to the manual methodology by which only the final volume was estimated, and all preceding volumes were inferred from the infusion rate. This discrepancy may be due to the infusion rate being affected by the bladder reaching max capacity. Near capacity, there may be more system losses or leakage which would reduce the filling rate. This can be seen in Figure 2.3A, where the volume with respect to time is highly linear for the majority of the filling, but at higher volumes, the trend became non-linear as shown by the plotted data falling away from the linear trend.

The reconstruction method involved generating voxellized representations of the bladders as the geometries were sourced from the pixelated image data. The conversion from voxel to mesh representation has many benefits. Meshes are a more standard 3D data representation than voxels since they are much more efficient in memory usage and graphical rendering.^{316,317} In this work, converting the voxel data to mesh data reduced the memory footprint by an order of magnitude while retaining data resolution, and rendering time was reduced by 72%. Creating meshed geometries also lend the data to future analysis by integration with finite element methods. A limitation that must be overcome however is that the meshes are all created independently from each other. In other words, the faces and vertices for a mesh at a given time point in the experiment have no connection to the faces and vertices of the mesh at the previous or following time point. Furthermore, each mesh has a different number of vertices and faces since they are independent of meshes of the same bladder at different time points. This limitation may be overcome by development of a method in which the vertices of the final mesh are projected onto the preceding mesh, and repeating this projection for all meshes back to the first bladder mesh surface.

Another limitation of this work is the shape-from-silhouette method. The shape-from-silhouette method is limited in that it does not completely capture the whole geometry of the bladder surface. This is a known drawback known as the visual hull effect.³⁰³ To overcome the visual hull problem, the silhouette on the z-axis was scaled for each z layer of the reconstruction. This effectively solved the hull issue, but imparts an assumption that the geometry across the entire z-axis is characterized by a single silhouette of the bladder from this top-down perspective. Overcoming this limitation is difficult, as more accurate shape-from-silhouette reconstruction would require many more imaging perspectives of the bladder. Where experimental setups allow, this is accomplished with more cameras, or by rotation of the object being reconstructed. Neither of these approaches is applicable to the experimental setup used for data collection here. There are other reconstruction methods in the literature, such as texture mapping where the lighting

conditions of the object are included rather than simply the object silhouette, or more advanced machine learning methods. These methods may be applied to bladder reconstruction method in future work as they require more development and expertise.

Other limitations include the amount of data generated from reconstruction and mechanical modeling, and visualizing this substantial amount of 4D data. For the data presented here, which includes 8 samples each including 52 data points, the total size of the mesh data alone was 7 gigabytes (GB). Each sample had significantly more than 52 data points in the raw data, with the average being 6300. Extrapolating, reconstruction of the full data set would size up to 100+ GB per sample. It is possible to reconstruct and model the full data, but it was beyond the scope of the current work. Additionally, the computational methods developed here were significantly optimized. Initially, the data processing pipeline for the data presented here took 14 days, and was reduced down to 2 hours after optimization and parallelization was implemented. Extrapolating again, processing the full data set would take 10 days with this optimized pipeline run on a typical workstation desktop. Neither the size of the data or processing time exceed the computational capacity available for this research, however it was beyond the scope of the current work. Specifically, the full data processing was out of scope largely due to the limited visualization methods developed. Significant time was dedicated to development of the reconstruction method. Methods for visualization were developed as shown by the figures in this chapter, however they leave much to be desired in terms of data analysis. Improved visualization is a subject of future work, and integrating the mesh and mechanical data into existing 3D visualization software may be a potential route to explore in the future. Nonetheless, the geometry and mechanical modeling of the bladders throughout pressurization were still able to be created and useful for the analyses here.

The mechanical model presented from the 3D reconstruction is useful since, due to the mechanics and material properties of the bladder wall, stresses are not expected to be uniform across the surface, and with this method, the distribution of stresses can be quantified and studied. This is an indication that the material properties at these regions may be different than the rest of the bladder wall. Analyzing the stress distributions in this way with dysfunctional bladders may provide even more insight into how the mechanics may be altered as a consequence of disease.

2.5 Conclusion

It is possible to create 3D models of *ex vivo* bladder filling accurately with low-cost laboratory equipment and open-source code. These methods can be used to inform better models of the mechanics of bladder filling. In this work, a detailed 3D model of the bladder was compared to a spherical approximation of the bladder. Results for average stress on the wall were similar. However, the full 3D model allowed for more in-depth analysis which is relevant to study the non-isotropic nature of the bladder as it deforms. Next steps will use these methods to compare the effects of sex on the mechanics and shape of the murine bladder.

2.6 Supplementary Material

An algorithm was developed which estimates the thickness of the bladder wall from the image data. The thickness was observable in the image data as the brighter pixels along the edge of the bladder due to dark food dye being added to the infusion solution. The contrast between the edge and the interior of the bladder in the images was marked enough that it allowed the thickness of the wall to be quantified as the radial depth of brighter pixels on the edge of the bladder.

This algorithm estimates the wall thickness by averaging the sum of bright pixels within a threshold around the edge of the bladder. First, the background was subtracted from the image using the segmentation mask. Bladder pixel values below the 5th and above the 95th percentiles were also dropped to remove dark and over-exposed spots. Remaining pixel values were then normalized. Next, two regions were obtained: the inner region, which was the set of normalized pixels not within a 4 pixel distance from the edge of the segmentation mask, and the edge region, which was the set of normalized pixels within 4 pixels from the edge of the segmentation mask. The inner region was the result of eroding the normalized pixels with 4 iterations and a 3×3 kernel. The edge region was obtained by masking out the inner region from the normalized set. The average pixel intensity on the inner region of the bladder (\bar{I}) was then calculated. Finally, the thickness was calculated as the sum of edge pixel values which were greater than \bar{I} divided by the circumference of the bladder in the image and then multiplying by the pixel-to-mm factor. The final thickness estimate was the average of both side view results. The thickness algorithm was applied to the two side view images, since these views had better contrast than the superior view. This thickness estimation was completed for each bladder on only the image at maximum

subsampled pressure. Finding the wall thickness at lower pressures using this method was less feasible since the wall was less visible having less contrast solution infused.

After estimation of final wall thickness (h), the thickness at all other subsampled time points (h') was calculated employing the hypothesis of material incompressibility (i.e., isochoric deformation) during filling. First, the volume of each mesh at max pressure was found using an established method^{306,318} and was declared v_{outer} as the outer volume of the bladder. Second, all vertices on the mesh were translated inward (i.e., direction opposite to the outward-facing vertex normal vector) by a distance h . This allowed quantification of the inner luminal volume (v_{inner}) at max pressure. Volume of the bladder wall was then quantified as $v_{wall} = v_{outer} - v_{inner}$. Once v_w was found, the wall thickness at all other time points h' was found by the inverse process. For each reconstructed mesh in the subsampled data, the wall thickness was found via a minimization function given by

$$\min_{h'} |v_{wall} - (v'_{outer} - v'_{inner})| \quad (2.10)$$

where v'_{outer} and v'_{inner} are the outer and inner volume for each value of pressure, as a function of h' . The optimized thickness is calculated as the first that results in an error below $1e^{-5} \text{ mm}^3$. This is possible only under the condition that the outer volume quantified for the minimum pressure was larger than v_{wall} .

The results of this thickness estimation algorithm were compared to manual thickness measurement (Table 2.1) completed in ImageJ as previously described.⁶⁷ The accuracy of the manual measurement was also previously validated with direct measurement of the bladder wall thickness via confocal microscope, and the error was between 1-4% (not shown).⁶⁷

Table 2.1: Comparison of methods for determining bladder wall thickness. RMSD = 0.018.

Sample	Manual Measure	Algorithm Estimation	Percent Error
1	0.112	0.114	2%
2	0.129	0.133	3%
3	0.127	0.138	9%
4	0.082	0.115	40%
5	0.132	0.126	-4%
6	0.121	0.128	6%
7	0.160	0.127	-20%
8	0.144	0.132	-8%
Mean			3%

The wall volume for the spherical model was found as

$$v_{wall} = \frac{4}{3}\pi[r_o^3 - (r_o - h)^3] \quad (2.11)$$

Knowing the volume of the wall, and outer radii at all other time points of interest, the thickness at other time points can be found as the difference between v_{outer} & v_{inner} , where v_{inner} can be calculated as

$$r_i' = \frac{3}{4\pi} \left(\frac{4\pi}{3} r_o'^3 - v_w \right) \quad (2.12)$$

CHAPTER 3

ADVANCED MODELING TO REVEAL SEX-SPECIFIC DIFFERENCES IN WHOLE BLADDER FILLING MECHANICS

3.1 Introduction

The mechanical behavior of the bladder is not well explored but is crucial for understanding the proper functioning of the lower urinary tract. Research on bladder mechanics is essential for creating better context for bladder dysfunctions which affect millions worldwide.¹⁻⁵ Despite the impact of urological conditions on quality of life and healthcare costs,³¹⁹⁻³²³ mechanical models of bladder filling which account for sex-specific differences are scarce in the literature.

The bladder functions through the interaction of neural, muscular, and connective tissues. Mechanical modeling of the bladder allows these physiological aspects to be studied and simulated in order to understand how these structures play a role in bladder health and dysfunction. This type of modeling has been effective in providing breakthroughs in our understanding of other organs such as the heart, brain, and lungs.^{62,324,325} There is a need for more accurate models of bladder mechanics using advanced computational and biomechanical techniques, as well as an increased awareness of biological sex differences as a contributing factor. Although the functional and anatomical sex differences are well-known in the literature, the effect of sex in regard to bladder mechanics during filling has not been investigated substantially.^{47,142} Unraveling this nuance in bladder mechanics is crucial for developing more appropriate gender-specific treatments and therapies for lower urinary tract dysfunctions.

This study aims to fill these gaps by comparing mechanical models of the bladder during the filling phase for male and female mice. By using a novel experimental method and advanced computational biology techniques, anatomically precise geometrical and mechanical models were developed to identify sex-specific mechanical behavior that may drive differences in urological outcomes. This work highlights that contemporary methods allow the ability to create such advanced models, and that bladder mechanics and sex differences can provide insights to bladder function that previous methods have not captured.

3.2 Methods

Mouse bladder experiments and 3D bladder geometry reconstructions were done as previously described [Chapter 2]. Briefly, mouse bladders were extracted, cannulated, and

pressurized in a novel experimental testing device.⁶⁷ The bladders were imaged simultaneously with pressure recordings. Bladder pressurization was done with a fill rate of 30 uL/min, and pressurization was repeated 3 times for each bladder to allow tissue acclimation. A pressure of 24 mmHg was reached for all bladders tested. Male (N = 17) and female (N = 12) animals (aged 10-12 weeks) were used. 3D reconstruction involved taking three orthogonal views of the bladder from the imaging, and using the shape-from-silhouette method^{253–255} to generate triangular surface meshes of the bladder at 0.5 pressure intervals from 0 mmHg to 24 mmHg.

An analysis of bladder shape and mechanical behavior was done as previously described [Chapter 2]. Surface curvatures were found and used to inform a pressure vessel mechanical model. The 3D bladder meshes were also modeled with an effective sphere. This provided information on how well the bladder is approximated by a sphere throughout filling, and also informed a spherical pressure vessel mechanical model.

This study builds on the previous analysis methods by extending the shape fitting to examine the best-fitting spheroid for the 3D bladder meshes. This was explored as the true shape of the bladder is often non-spherical.^{102,106,313–315} Building mechanical models which can account for the anisotropic characteristic of the bladder wall can provide deeper understanding of the bladder mechanics. In this approach, a least-squares fitting was done to find the best fitting spheroid for each bladder mesh. First, the moment of inertia tensor was found for each mesh, and then the mesh was rotated such that the principal axes of inertia aligned with the global coordinate axes. This was done to simplify the spheroid fitting process, as it eliminates the need to account for off-axis rotation of the mesh. For the least squares fitting, the axes for the best fitting spheroid are found as an optimization of the squared Euclidean norm as given by Equation (3.1).

$$\min_x \|Ax - b\|_2^2 \quad (3.1)$$

Where A contains the rotated mesh vertex coordinates with size $n \times 2$ with n being the number of vertices, x contains the two target spheroid coefficients (a and c for the circumferential and longitudinal directions, respectively), and b is the matrix of ones with the size $n \times 1$. Equation (3.2) shows the structure of these matrices. The structure of Equation (3.2) is based on the equation for a spheroid, given by Equation (3.3).

$$A = \begin{bmatrix} x_1^2 + y_1^2 & z_1^2 \\ \dots & \dots \\ x_n^2 + y_n^2 & z_n^2 \end{bmatrix}, \quad x = [a \quad c], \quad b = \begin{bmatrix} 1 \\ \dots \\ 1 \end{bmatrix} \quad (3.2)$$

$$\frac{x^2 + y^2}{a} + \frac{z^2}{c} = 1 \quad (3.3)$$

This only represents spheroids with z as the symmetry axis. To account for either x or y potentially being the symmetry axis in the best fitting spheroid, the fitting was repeated twice again to reflect the other symmetry axes. Specifically, least squares fitting was repeated to find the best fitting parameters with all three variants of A with the additional two shown by Equation (3.4).

$$A = \begin{bmatrix} z_1^2 + y_1^2 & x_1^2 \\ \dots & \dots \\ z_n^2 + y_n^2 & x_n^2 \end{bmatrix}, \quad A = \begin{bmatrix} x_1^2 + z_1^2 & y_1^2 \\ \dots & \dots \\ x_n^2 + z_n^2 & y_n^2 \end{bmatrix} \quad (3.4)$$

Then, after fitting the three possible orientations of a spheroid to each bladder mesh, the best fitting parameters (axis lengths a and c) were taken from the fitted orientation with the lowest residual error. Once the best fitting spheroid parameters were found for each bladder, it was manually verified that the parameters corresponded to the longitudinal and circumferential directions of the bladder as previously described.

Lastly, the spherical stress and stretch data were analyzed as previously described.¹¹³ Briefly, a low stiffness and high stiffness region was identified for the stress-stretch data of each sample, and the slope of the stress-stretch curve in these regions were quantified as k_{low} and k_{high} . The upper boundary of the low stiffness region was defined by the stress and stretch at this point, σ_1 and λ_1 . Similarly, the lower boundary of the high stiff region was located as the stress and stretch at this point, σ_2 and λ_2 . The intersection point of the low and high stiffness regions was defined by the point σ_{int} and λ_{int} . These parameters are visualized by Figure 3.1, which is reproduced from Zwaans et al. 2022.¹¹³ Note that t in Figure 3.1 is called σ in this work. Statistical comparisons were done with ANOVA with a significance level of $P < 0.05$ for pressure-volume, stress-stretch. Student's t-test with a significance level of $P < 0.05$ was used for statistical comparisons of compliance and stiffness parameters.

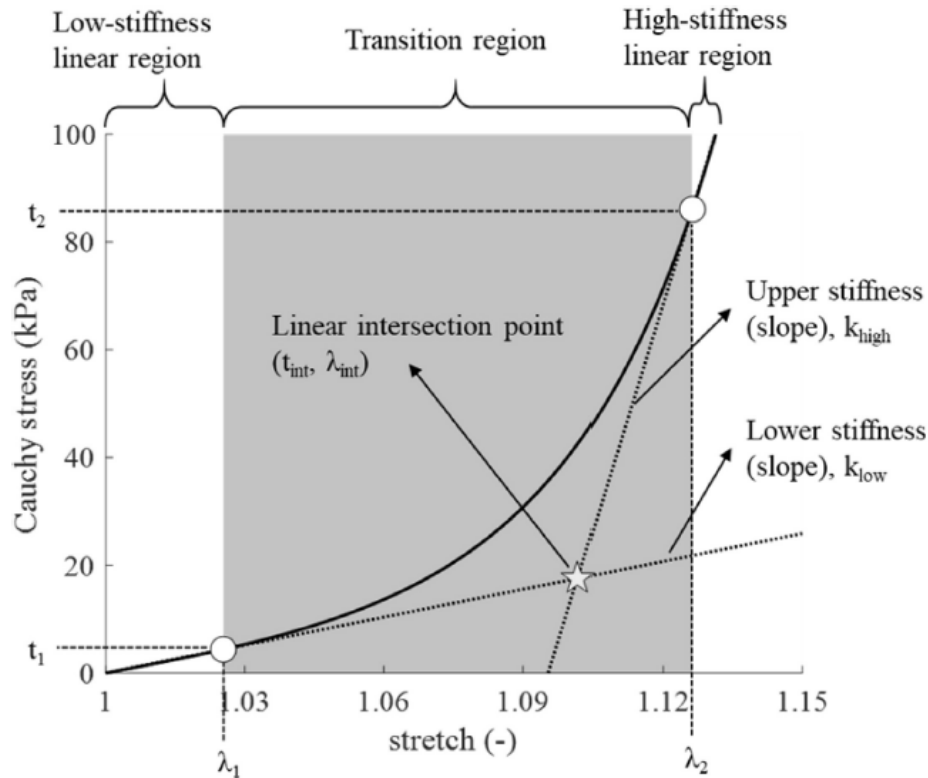


Figure 3.1: Stiffness regions and parameters obtained for the spherical model stress-stretch data for each sample. A low stiffness region, high stiffness region, the boundaries of these regions, and the intersection of the low and high stiffnesses were located and compared between the two sexes. Reproduced from Zwaans et al. 2022.¹¹³

3.3 Results

Plotting the volume data averaged across pressures for each sex revealed significant differences between male and female bladders as shown by Figure 3.2. A 2-way ANOVA with factors of sex and pressure and an interaction term showed that female bladders were significantly smaller in size compared to males on average.

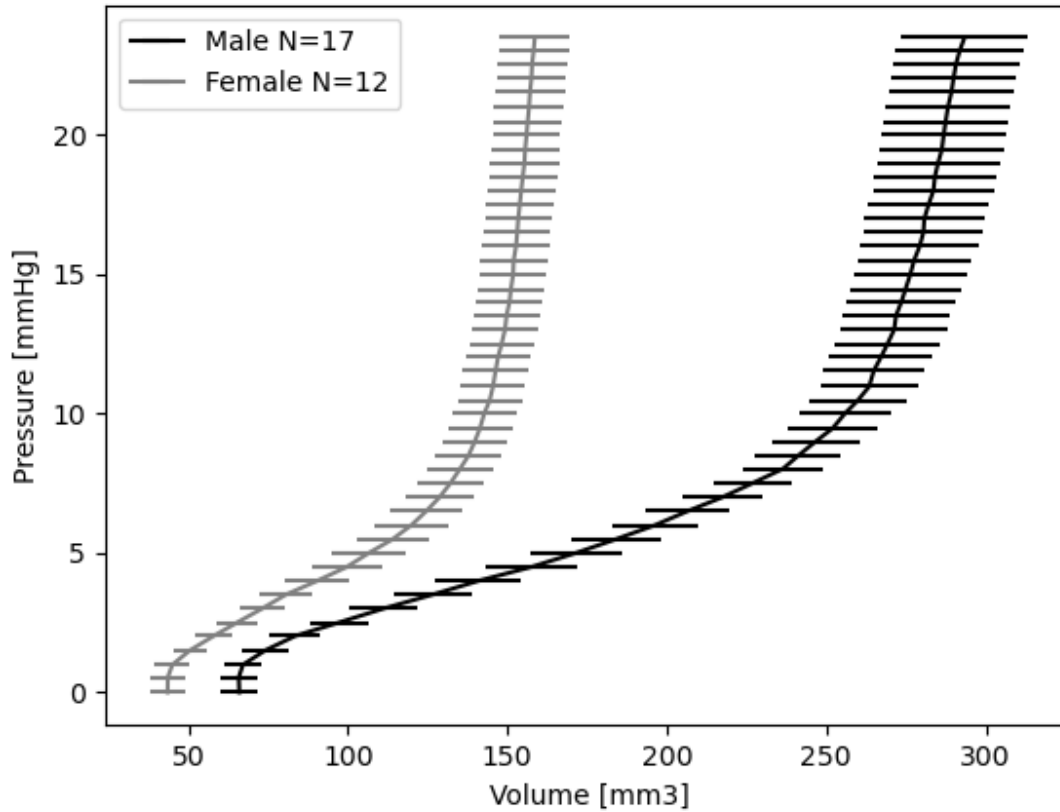


Figure 3.2: Pressure-volume graph. Volume at each pressure step was averaged across groups. Female bladders had significantly smaller volumes compared to males on average ($P < 0.05$). Standard errors shown.

Plotting the spherical stress and stretch revealed similar significant differences in bladder mechanical behavior between the two sexes, shown in Figure 3.3. In addition to female bladders being smaller, a 2-way ANOVA with factors of sex and stress and an interaction term showed that sex was a significant factor in the amount of stress for equivalent pressures.

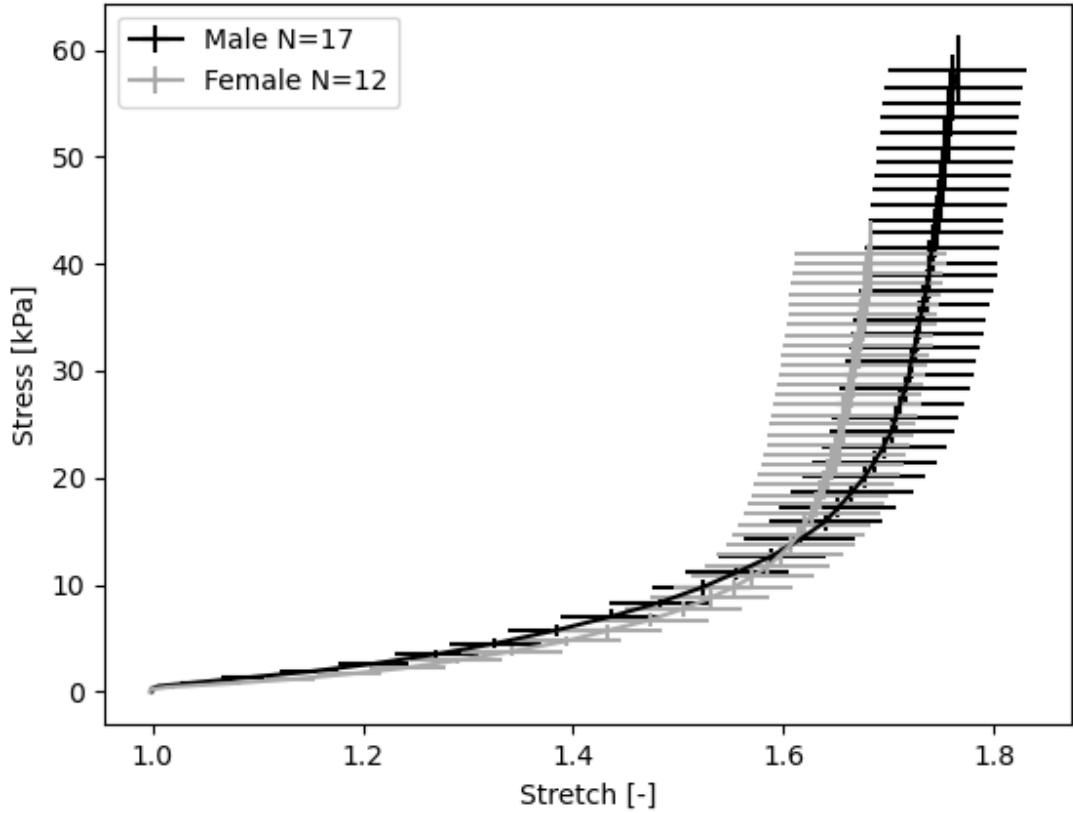


Figure 3.3: Spherical model of stress and stretch. Stresses calculated at equivalent pressures and averaged for male and female groups. Bladder wall stress was significantly lower in females compared to males on average. Standard errors shown.

Next, the stresses calculated from the spherical model, and the average von-Mises stress across the entire surface were compared following the methods outlined in Chapter 2. Figure 3.4 shows the stress-volume results from the 3D model compared to the spherical model. Volume for the 3D model was quantified as the volume of the mesh, and volume of the spherical model was calculated as the spherical volume using the radius of the effective sphere.

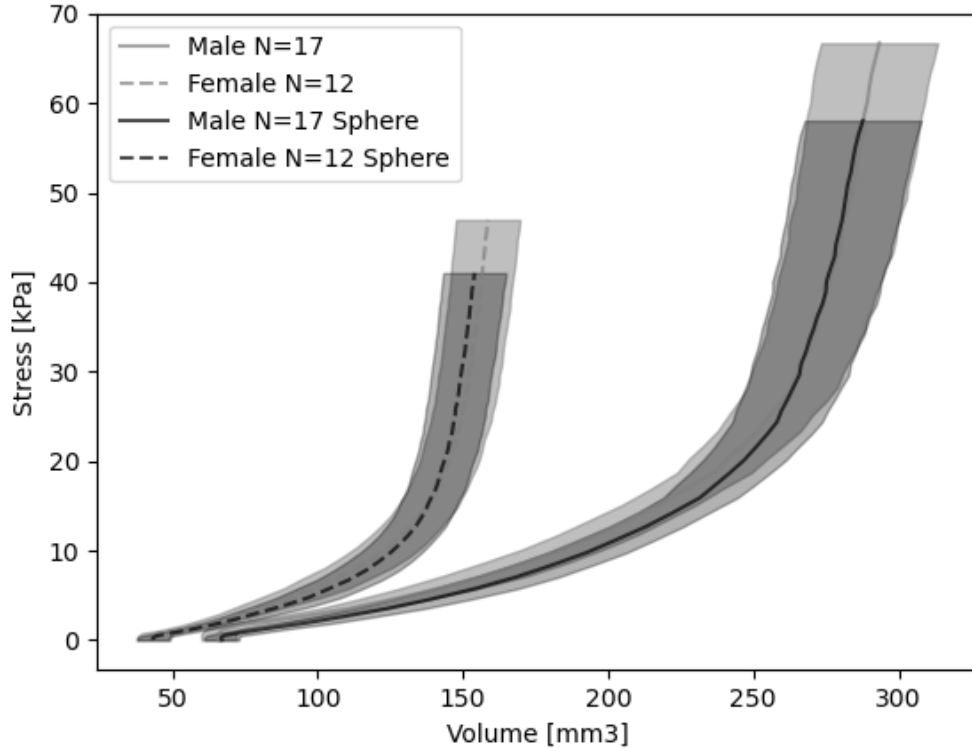


Figure 3.4: Average stress-volume between the two groups using the 3D model and spherical model. For the 3D model, volume was obtained as the volume of the bladder mesh, and stress was the average von-Mises stress across the entire surface of the bladder. For the spherical model, stress was obtained from the thin-walled spherical Laplace equations, and volume was obtained as the spherical volume using the radius of the effective sphere. Standard errors shown by the filled regions.

An analysis of bladder shape is presented next. Figure 3.5 shows quantifications of spherical measures. Specifically, the RMSD between the effective sphere and mesh, and sphericity. Both measures showed that at low pressures, the bladder is more poorly approximated by a sphere compared to higher pressures. Figure 3.6 shows geometrical analysis of spheroid fitting to the bladder meshes. It was found that the rate of change of both spheroid axes appeared similar, but since the circumferential axis was shorter than the longitudinal, the stretch in the circumferential direction was larger.

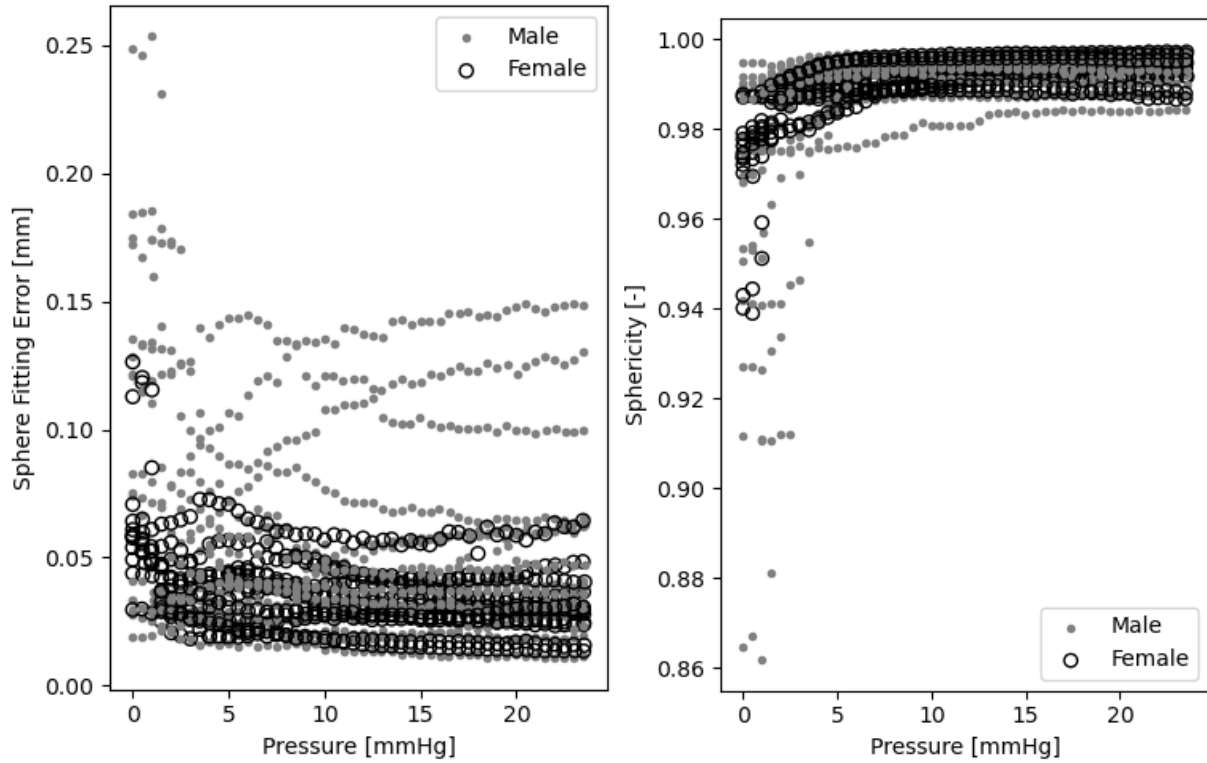


Figure 3.5: Bladder shape spherical measures. Left) RMSD of the effective sphere fitted to the bladders throughout filling. There was larger error between the effective sphere and mesh at lower pressures, which decreased as pressure increased. Right) Sphericity of the bladders throughout filling. Lower pressures showed lower sphericity. As the bladder filled, this measure indicates that the bladders become more spherical as the pressure increased.

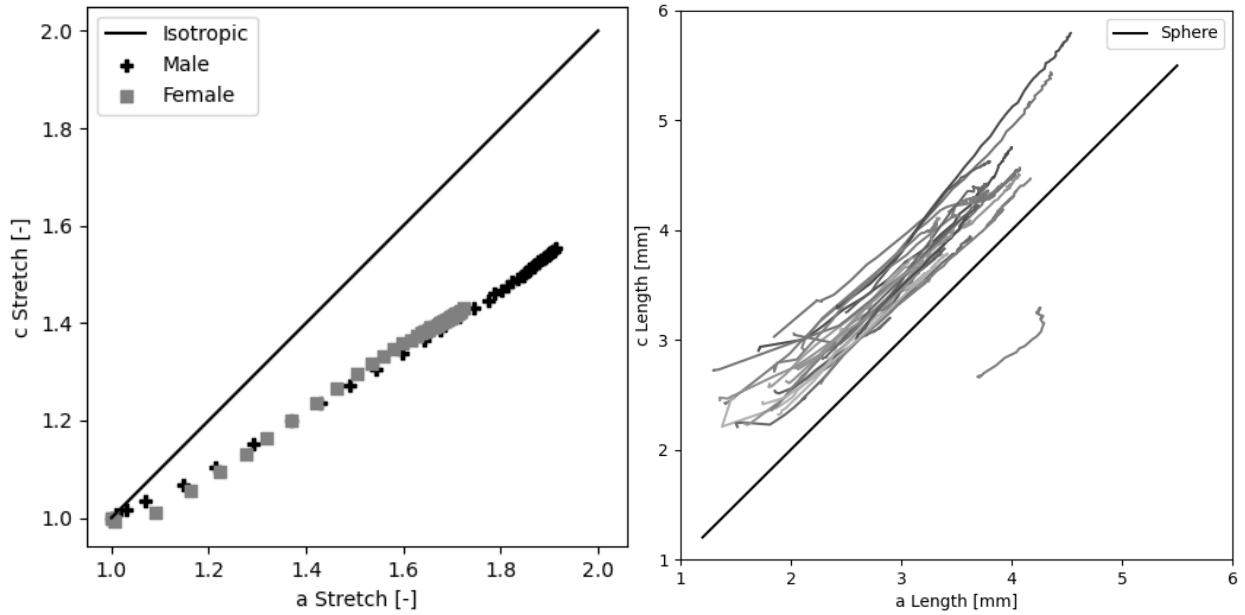


Figure 3.6: Fitted spheroid geometry results. Left) Longitudinal (c) and circumferential (a) stretches averaged between the groups. Both groups showed larger stretch in the circumferential direction. Right) Spheroid axis lengths for all samples. The rate of change for each axis was relatively equivalent, but since the circumferential axis was shorter than the longitudinal axis for the samples, it showed larger amount of stretch as given in the left plot.

The stress distribution on the 3D bladder geometry was visualized by flattening the mesh as previously described, normalizing the dimensions, and then creating a heat map of the average von Mises stress across each group over the normalized plot. This is shown in Figure 3.7 for two levels of pressure (10 and 20 mmHg) for both sexes. The plots revealed that the male and female bladders had unique non-uniform stress distributions, and the distribution appeared to be preserved between the pressure levels analyzed.

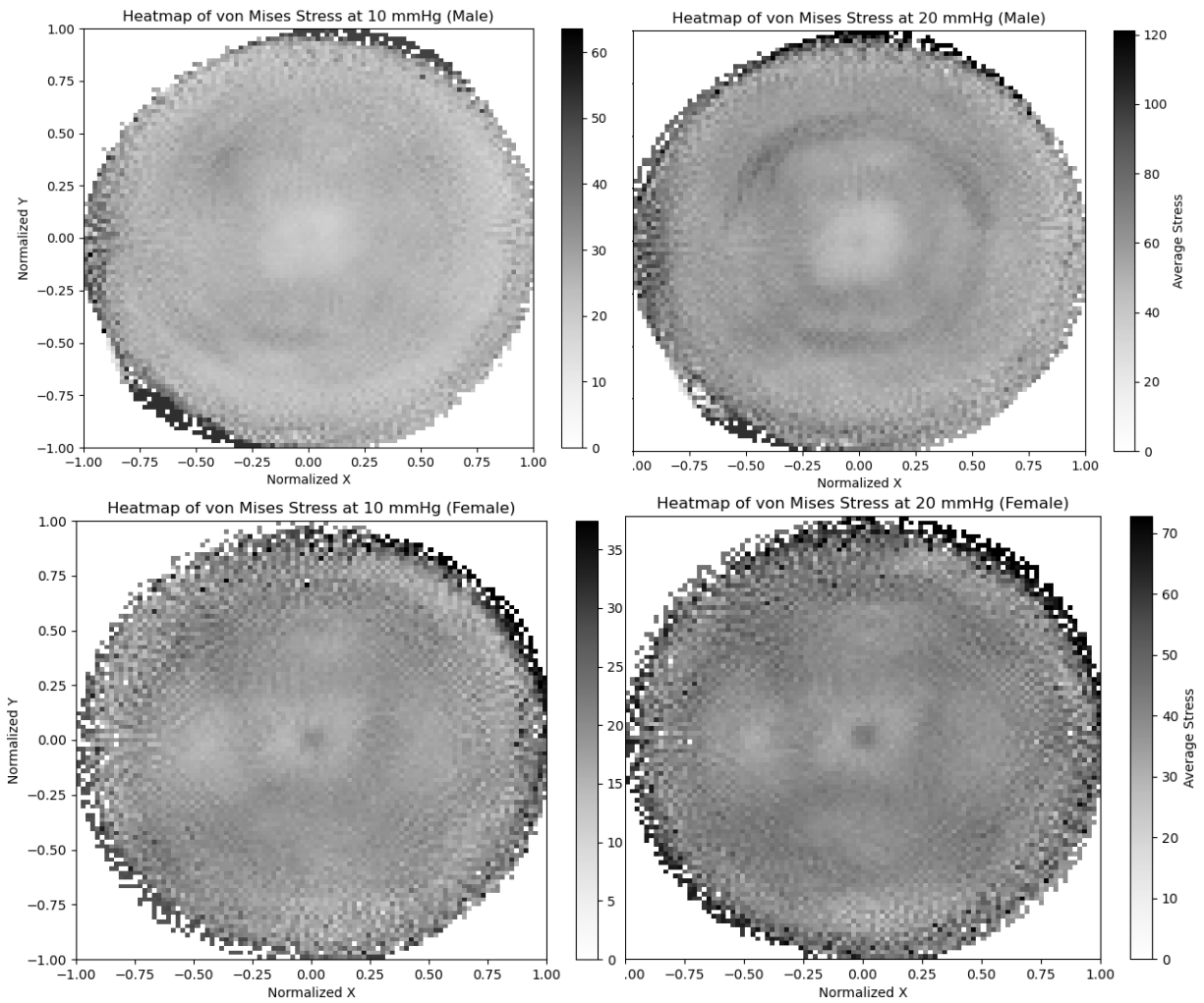


Figure 3.7: Average von Mises stress distribution at 10 and 20 mmHg for male and female. The stress distributions between the two sexes were non-uniform and showed different patterns between male and female sex. The non-uniformity unique to each sex appeared to be preserved throughout these pressures analyzed. In these plots, the center of the heat map corresponds to the top of the bladder (dome), and the outer circumference corresponds to the bladder neck.

Bladder compliance is defined as the change in volume by the change in pressure during filling as a measure of distensibility. Compliance was calculated for several pressures (5, 10, 15, 20 mmHg) and averaged for male and female groups. The results are shown by Figure 3.8. Compliance was significantly higher in males compared to females at all pressure levels analyzed ($P < 0.05$). This is likely due to the fact that the female bladders exhibited a smaller volume compared to the males (Figure 3.2) at all pressures.

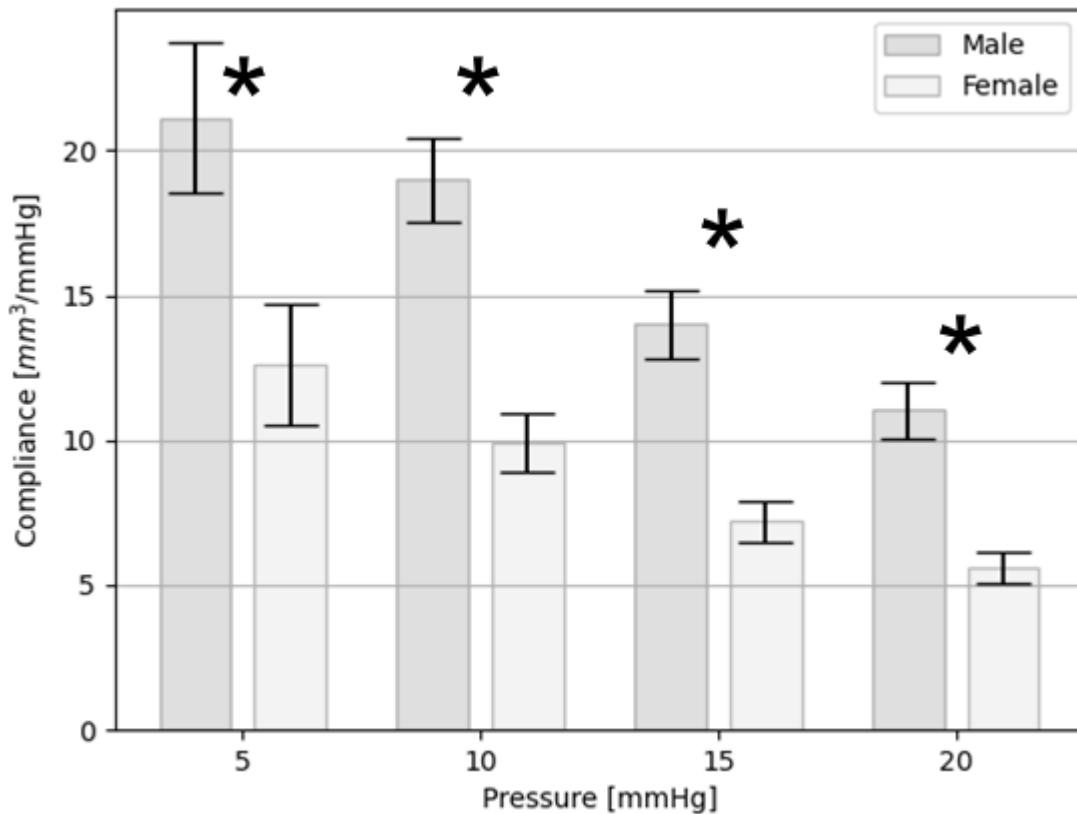


Figure 3.8: Bladder compliance ($\Delta V/\Delta P$) at 5, 10, 15, 20 mmHg pressure levels. Compliance was significantly different between the two groups at all pressure levels analyzed. This difference is likely driven by the smaller volume of the female bladders shown by Figure 3.2.

Finally, the low and high stiffness parameters described in the methods are presented as group averaged in Table 3.1. Comparing the parameters between the two groups, only the upper boundary for the low stiffness region, λ_1 , was significantly different between the two groups.

Table 3.1: Spherical Stress-Stretch Stiffness Region Parameters & Constitutive Parameters.

Parameter	Male Average	Female Average	P value
k_{low}	11.015	6.609	0.417
k_{high}	961.088	676.147	0.396
σ_1	4.216	2.047	0.290
σ_2	89.034	88.588	0.775
λ_1	1.325	1.234	0.045 *
λ_2	1.787	1.759	0.640
σ_{int}	6.527	4.616	0.637
λ_{int}	1.596	1.641	0.418

3.4 Discussion

The reconstruction method applied to experimental data collected on male and female mouse bladder pressurization was able to show geometrical and mechanical differences between the sexes.

As expected, the bladders collected from female animals were found to have a smaller volume when compared to those collected from male animals (Figure 3.2). Furthermore, shape analysis of the 3D bladder geometries revealed that the sphere represents a reasonable approximation at high pressures (and infused volumes) for both sexes. However, it also highlighted that bladders from both male and female animals are poorly approximated by an effective sphere at low values of pressures, in a range relevant to the *in vivo* condition (Figure 3.5). Approximating the bladder as a spheroid can capture the unique shape of the bladders better than a simple sphere. It was found that the rate of change of the bladders in the longitudinal and circumferential directions appeared similar. However, the circumferential direction exhibited greater stretch than the longitudinal direction (Figure 3.6). This could be due to the circumferential axis being shorter than the longitudinal when the bladder was empty. The anisotropic stretch behavior shown by Figure 3.6 is worth highlighting, as this behavior can only be captured by non-spherical modeling of the bladder.

The spherical stress analysis showed that bladder from female animals exhibited lower mechanical wall stresses for the same level of pressure compared to the male group (Figure 3.3).

This suggests that the bladders from female animals are more distensible when compared to male animals. This is also confirmed by the parameter of compliance which was quantified here at various pressure intervals and was found to be significantly lower in bladders collected from female animals compared to male at all pressures (Figure 3.8). Bladder compliance is a metric commonly used clinically to assess bladder distensibility. This difference seems to be due to a combination of geometrical and structural characteristics of the bladder wall as the female bladders were already found to have volumes (Figure 3.2) as well as reach lower stresses for equal pressures (Figure 3.3) compared to males. In addition, our results confirm what observed by other research who have also shown that female bladders have a lower compliance than male bladders.³²⁶ Furthermore, the 3D mechanical model was able to reveal significant differences between sexes in a few ways. First, it revealed the existence of sex-differences between directional stretches, which is a measure of tissue anisotropy, as the bladders were pressurized (Figure 3.6). Second, the comparison of the von Mises stress pointwise average based on animals' sex over the normalized plot (shown in Figure 3.7) showed, for the first time, a unique non-uniform distribution within each group. Specifically, across the bladder surface, the low and peak stress areas were ascribed to different anatomical locations between male and female groups. Furthermore, these locations were consistent across pressure levels. At the bladder neck, which corresponds to the outer circumference of the plots of Figure 3.7, were the highest stresses for both groups. This seems to confirm that the bladder neck is stiffer than the rest of the bladder wall which has also been shown in other studies.^{93,186}

Lastly, several parameters to characterize the stress-stretch curves of the spherical model previously shown,¹¹³ were quantified in this research. While the spherical stress-stretch curves showed some significant differences, primarily in the lower amount of stress in female bladders (Figure 3.3), the majority of the stiffness parameters assessed from this analysis did not reveal any differences between the groups (Table 3.1). The single parameter that showed a significant sex-dependent difference was the stretch defining the upper boundary of the low-stiffness region (λ_1). This supports the idea that the differences between mechanical behavior of the male and female bladder wall is concentrated in the low stress region. In addition, it is important to point out that our results highlighted how the spherical analysis may not be the most appropriate in this low-stress, low-pressure region (Figure 3.5). In other words, sex-dependent differences in the low-pressure region (i.e., the most relevant to the *in vivo* filling behavior) might be lost in applying the

simplified and “averaged” spherical analysis. Finally, the results of Figure 3.3 as well as 3.7 show that the high-stress high-pressure mechanical behavior of the bladder may also contain sex-differences, which are similarly lost when applying the spherical approximation.

Finally, this analysis is not without limitations. The main limitation is represented by the possibility of geometrical artifacts derived from the 3D reconstruction method. The reconstructed bladder surfaces were heavily smoothed as a processing step to minimize these geometrical artifacts (e.g., sharp edges in the meshes). However, the bladder neck is a transition region which is difficult to capture consistently from the imaging and reconstruction method. Due to variation in the bladders’ tissues, some of the bladders had a clearly defined neck region in the imaging throughout pressurization, while in other bladders the neck was not clearly visible in the imaging. This introduces the possibility of the existence of geometrical artifacts around the neck which may be confounding factors in the point-wise stress analysis. Nonetheless, the focus of this research is mainly on the mechanics of the bladder wall as a whole, so this does not take away from the value of the stress distributions shown here.

3.5 Conclusion

The differences in mechanical stress and stretch behavior between male and female bladders as modeled here highlights that biological sex is an important factor to consider when studying the bladder. This has implications for bladder treatments and interventions, as well as establishment of standards for measures of healthy bladder between the sexes. Previous research has shown that the male and female bladders have different filling and emptying characteristics.^{47,79,142,289,327,328} These differences may be driven by microstructural differences in the bladder wall between the sexes. The work here primarily analyzed the bladder mechanics based on an accurate macro-level geometrical information. The results presented here indicate that future work should focus on inclusion of microstructural information of the bladder tissue for deeper insight into the drivers of sex differences within the bladder. Furthermore, this research lays the groundwork for inspection of the stress distributions throughout the bladder wall. Microstructural differences between male and female tissue may also alter the distribution of stresses in the bladder wall, which may play a role in the higher stresses observed in male bladders. This level of detail in mechanical modeling can only be captured by these advanced methods, and are completely lost when the bladder is modeled as a sphere. While the spherical model has value in its simplicity and that it may provide a reasonable estimate of overall stress in the bladder wall, the advanced

experimental and computational methods available today are able to be utilized for deeper understanding of the mechanics of the bladder wall. Further development of more sophisticated bladder modeling is imperative to understanding bladder health in terms of the tissue mechanics. Pairing sophisticated mechanical models with metrics of bladder health in future work may reveal underpinnings of bladder functions which are currently not well understood.

This work contributes to the literature of sex differences in bladder function and mechanics. The female bladder exhibits lower volumes and stresses at similar pressure compared to the male bladder. The detailed geometrical and mechanical models of the bladder presented here for a mouse model has not been shown in the literature before. The results presented in this research highlight how more advanced mechanical models provide deeper insight to the mechanical functioning of the bladder wall. Specifically, understanding the anisotropic characteristics of bladder deformation, and the non-uniform stress distributions can aid in understanding of bladder functioning that is not often shown in the literature. The spherical approximation of the bladder for modeling pressurization mechanics is often relied upon where advanced methods have not been developed. However, this model is simplistic and dated. Modern experimental methods and computational resources provide the tools to advance bladder mechanics models and have not been appreciably leveraged for their utility. The methods developed and used here to analyze sex differences in bladder mechanics contribute to pushing forward the standards for analyzing bladder filling behavior at a more detailed level.

CHAPTER 4

UNIAXIAL BLADDER RING TESTS REVEAL SEX-SPECIFIC DIFFERENCES IN BLADDER TISSUE MECHANICS

4.1 Introduction

Uniaxial stretching tests were done on bladder tissue sections from the same cohort of specimens used for the 3D reconstructions. In these tests, the effect of sex (male vs female) and decellularization was analyzed. It has been previously shown in mice that sex effects filling and voiding behavior.¹³⁸ Uniaxial stretching of bladder tissue can reveal if mechanical behavior of the tissue plays a role in these differences. Although this type of testing is different from the loading conditions of the whole organ *in vivo* by pressurization, uniaxial loading is a valuable mechanical test which provides information about the mechanical characteristics of the biological material.^{113,329,330} The testing protocol implemented here is also conducted with the tissue samples submerged in a thermo-chemical environment comparable to the physiological state. Furthermore, comparing the results of tissue with intact cellular structure vs decellularized tissue allows the mechanical contribution of the cells/extracellular matrix (ECM) to be analyzed. Since the bladder wall has a muscular component (the detrusor) which can be active *ex vivo*, it is important to consider that the tissue mechanics can have contributions from both the ECM (passive) and muscle cells (active).³¹ Previous studies have compared the bladder mechanics between cellular and decellularized tissue in rats³¹, however the decellularization effect on bladder mechanics in mice has not been shown before. In the experiments described here, significant differences were found in the bladder geometry due to sex and decellularization, and the interaction of sex and decellularization showed significant effects on the mechanical behavior of the tissue.

4.2 Methods

For these mechanical tests, the bladder was excised and transported to the lab in the same way as described in Hennig et al. 2022.⁶⁷ Once the tissue was received, the bladder was sectioned into three sections. The bladder was flattened on its side, and two cuts were made longitudinally (Figure 4.1). The cuts were done such that two rings of equivalent thickness were obtained, and the dome of the bladder was stored for other experiments. The lower ring, containing the neck of the bladder, was mechanically tested immediately. The upper ring was tested after a decellularization protocol. This was done so that the results could be compared between the

cellular and the decellularized tissue.³¹ Bladder tissues were collected from male (N = 7) and female (N = 7) animals so that the effect of sex (if any) on the mechanical results could also be assessed.

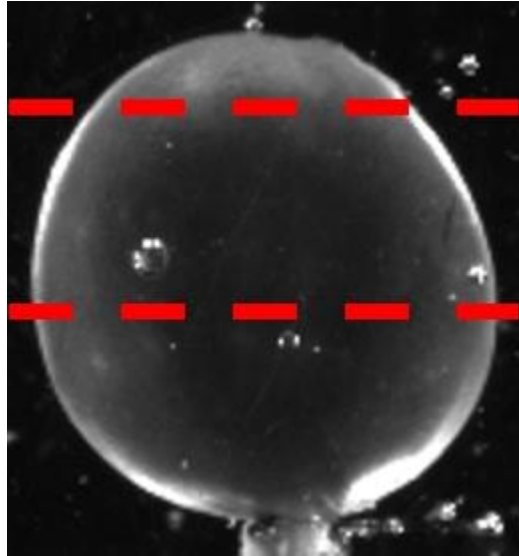


Figure 4.1: Representation of bladder ring sectioning method. Two cuts are made, one roughly below the midline of the bladder, and another near the dome of the bladder. Gave two rings of comparable size, and the dome tissue was disregarded for these experiments.

The lower ring was tested immediately, and the upper ring was tested after decellularization.

The decellularization protocol is as follows. The tissue is submerged in Phosphate-buffered saline (PBS) containing 0.2% heparin for 15 minutes, then a 1% Sodium dodecyl sulfate solution for 48 hours, then deionized water for 15 minutes, and finally a 1% Triton-X100 solution for 30 minutes, all at room temperature. Decellularization leaves only the extracellular matrix (ECM). Figure 4.2 shows a collection of some of the bladder tissue rings with intact cellular structure vs isolated ECM tissue.

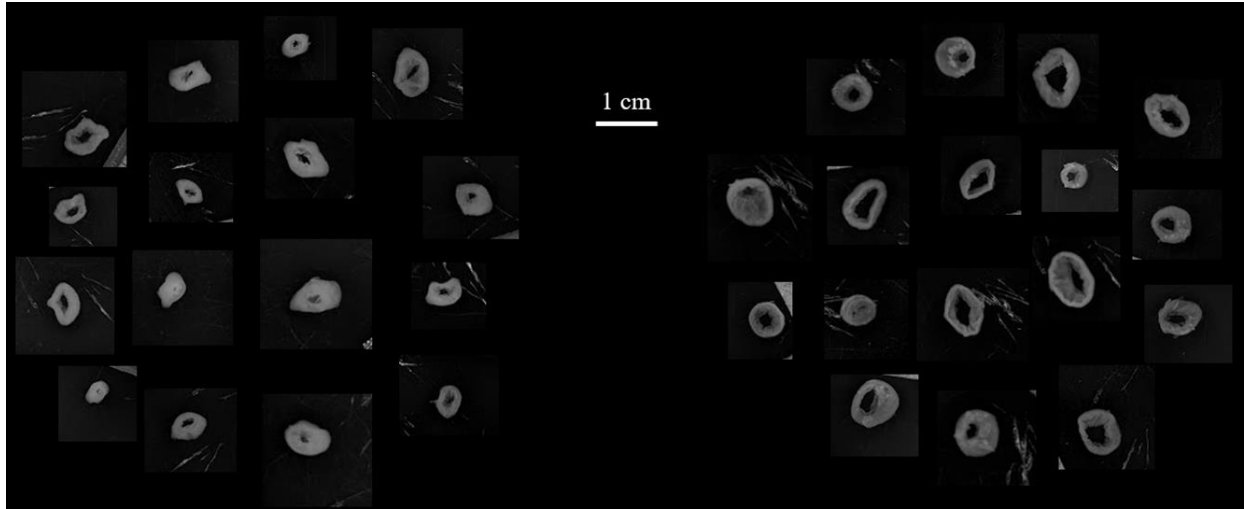


Figure 4.2: Left) Cellular bladder tissue rings. Right) Decellularized bladder tissue rings.

The mechanical testing protocol is as follows. The ring was mounted on the uniaxial testing device via two loops of thread. One of the threads looped through the ring and attached to a rigid hook, and the other thread looped through the ring and attached to a load cell (Futek LSB200, 250g capacity). The sample was submerged in a Krebs bath (36°C, 7.4 pH) during setup and testing.³³¹ A camera (Hitachi KP-M2A, grayscale, 2592×2048 resolution) was positioned in front of the tissue to capture the deformation during stretching. Custom LabVIEW code was used to collect data from the load cell and camera simultaneously during testing. The code also drives a motor which stretches the tissue by changing the distance between the two plates which the load cell and rigid hook are attached to. Within this setup, the code allows control of load applied to the tissue by either specifying a change in distance between the plates, or by setting an amount of stretch based on the height of the ring within the testing device. Figure 4.3 shows the testing device setup with the neck of a balloon in place of the ring sample for visibility.

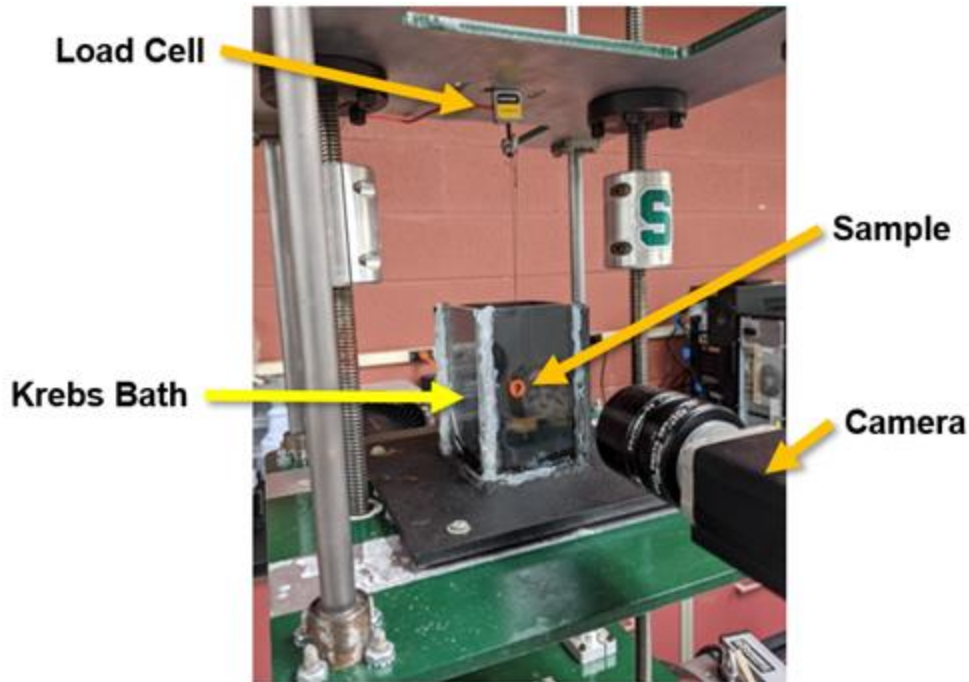


Figure 4.3: Testing device setup. The bladder ring sample (represented by the neck of an orange balloon here) was tied to a rigid hook in the Krebs bath (black chamber) and the load cell. A camera positioned in front of the chamber captured the bladder geometry during testing. The tissue was stretched by increasing the distance between the two plates which the rigid hook and load cell are fixed to.

A temperature regulation device was developed for these experiments. Although the tissue is excised and sectioned in these tests, there was still an aim to simulate the physiological environment that the tissue typically functions in *in vivo*. The Krebs bath is a physiological salt solution which mimics the fluid environment of physiological tissue by offering similar electrolyte concentrations, osmolarity, and pH.³³¹ Biological tissues operate within a specific chemical environment, but also a thermal environment (i.e., body temperature). The resting body temperature of the mouse is near 36°C.³³² So, to further simulate the typical tissue environment, a temperature-regulated heating element was added to the testing device to maintain the Krebs bath at this temperature. To accommodate the heating element, a new chamber was added to the bath setup shown in Figure 4.3. The heating element (50W hygger Pinpoint Saltwater Aquarium Heater) was fixed in the lower chamber, with the power cord routed out the back and sealed with silicone. The heater power was plugged into a temperature regulator which monitored the bath temperature

via a thermometer probe placed in the upper chamber throughout testing. The regulator cycled power to the heating element to maintain the specified temperature. The main bath was modified with holes which allowed the heat from the element to rise to heat the main chamber and the tissue sample (Figure 4.4). After the tissue was mounted in the device, the heating device was powered on, and time was allowed for the bath to get up to temperature. This setup was found to reliably maintain the temperature within the bath at $36^{\circ}\text{C} \pm 0.1^{\circ}\text{C}$.

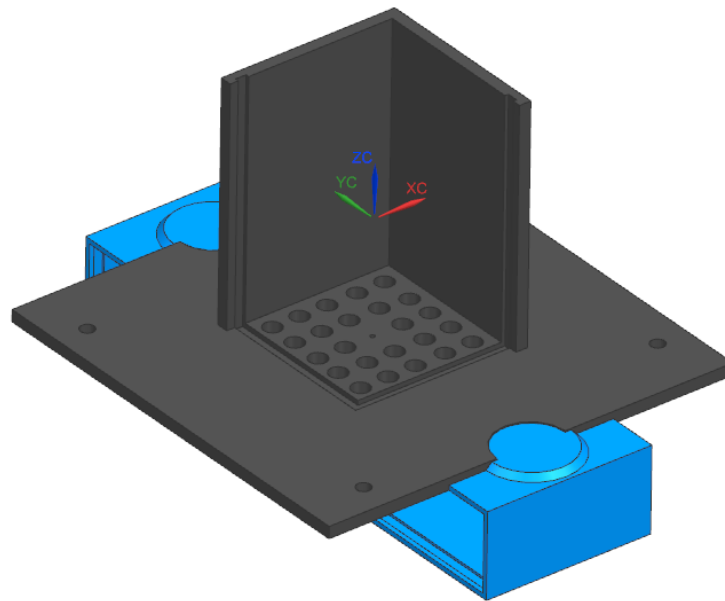


Figure 4.4: 3D schematic of temperature regulation bath. Acrylic walls are added to the device to enclose the main chamber (black) and heating element chamber (blue). The heating element is fixed in the blue chamber. Both chambers are filled with Krebs solution, and the heat generated by the element rises to heat the main chamber via the holes in the bottom of the black chamber.

Once the tissue was loosely mounted in the device and the temperature was equilibrated, a one-gram preload was applied continuously to the tissue for 10 minutes. This was a continuous process of incrementally increasing the distance between the boundaries (load cell and rigid hook) since, due to the viscoelastic nature of the tissue, the load on the tissue decreases as the tissue relaxes and acclimates to its current condition.^{29,31} It was found that after 10 minutes at the one-gram preload, the tissue relaxation was diminished. After the preloading step, the tissue was

subjected to cyclical and incrementing stretches. The stretching protocol included 10% stretch for 10 cycles, and 20%, 30%, and 40% stretches for 5 cycles each. Figure 4.5 shows the cyclic loading and unloading for a sample tested at 40% stretch. Stretch was applied at a constant rate of 1%/s to the specified stretch, and then in reverse back to 0% stretch. This was repeated in cycles so that the mechanical behavior of the tissue in this test became repeatable. Between each group of stretch cycles, a one-gram preload was reapplied for 90 seconds. The preload was able to be applied for a shorter amount of time between stretching due to the tissue being sufficiently acclimated and having minimal relaxation throughout the testing. The last loading cycle was used for analyzing mechanical stress and stretch of the tissue.

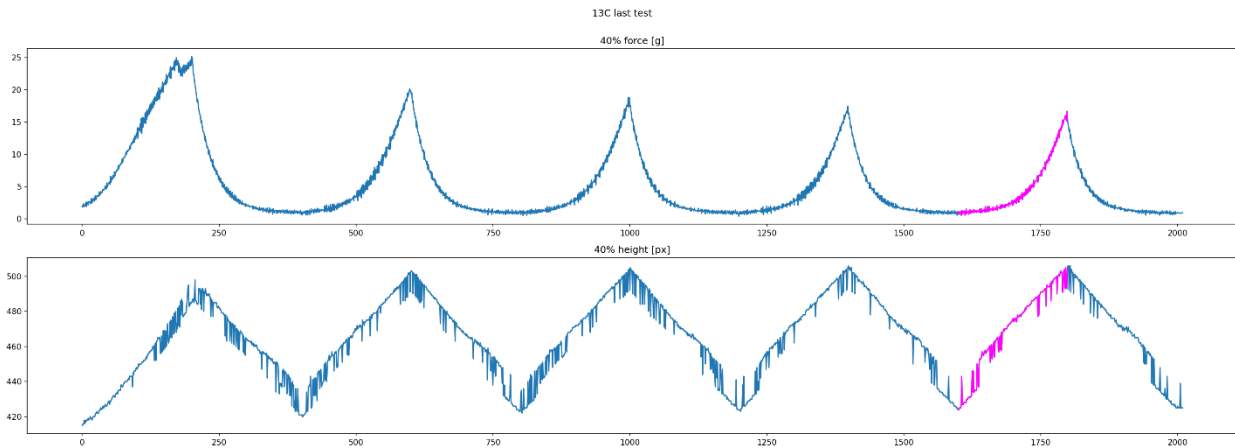


Figure 4.5: Data recorded during a stretch cycle group. Representative sample being stretched to 40% stretch for 5 cycles. The first loading cycles appear unique, however as the cycles progress, the loading graph becomes repeatable. Pink represents the last loading cycle which was used for the mechanical analyses.

Throughout testing, the load applied to the tissue was recorded via the load cell, and an image from the front camera was captured simultaneously at 5 Hz. The front images were used to quantify the height and width of the tissue using thresholding in LabVIEW (Figure 4.6, bottom). The tissue in the image was thresholded into a binary image, and height was quantified as the average vertical height of white pixels, and width was the average horizontal width of white pixels. A separate side camera was used to capture an image of the bladder from the side at the start of each group of stretch cycles. The thickness of the bladder tissue (Figure 4.6) was quantified as the

average width of white pixels in the thresholded side view image. This thickness could only be quantified for the reference configuration since it was only captured at the beginning of each cycle of tests. However, with the assumption of isochoric deformation (i.e., incompressibility), the volume at the reference configuration was calculated, and was used to calculate the thickness of the tissue throughout stretching as the height and width at all configurations is known from the front images. The incompressibility hypothesis is often used for mechanical modeling of bladder tissue.^{28,99,113,148,213} The load was measured in grams, and the tissue geometry obtained from images of the tissue was converted from pixels to mm with the pixel-to-mm factor of 1/39 for this specific setup. Figure 4.6 shows the dimensions of the bladder ring and how they are obtained by measuring the thresholded images of the front and side views of the bladder in the testing setup.

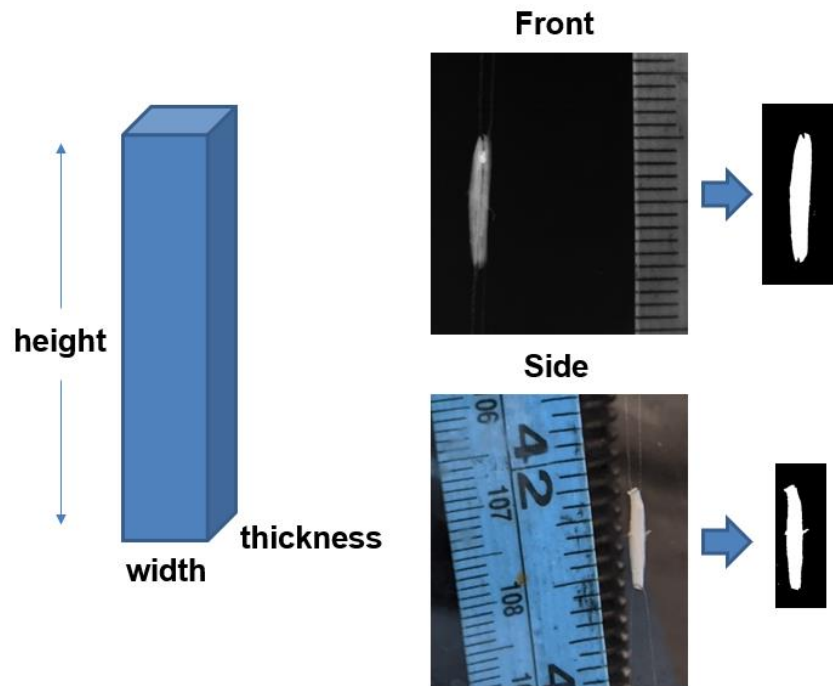


Figure 4.6: Bladder dimensions obtained from thresholding front and side views images.

The front image gives the height as the average vertical number of white pixels in the thresholded image, and the width as the average horizontal number of white pixels in the same image. Thickness is quantified as the average horizontal number of white pixels in the thresholded side image at the reference configuration. The isochoric deformation assumption allows the thickness to be calculated for all other configurations from the front view dimensions. The pixel dimensions are converted to mm with the scales in the images.

A post-processing method was developed to find the best thresholding value for each bladder ring tested to allow for more accurate geometrical measurements. This was approached as an optimization problem for the thresholding parameter that led to the most linear measure of height throughout stretching. That is because the height is expected to increase linearly since experimentally the stretch was applied at a constant rate (1%/s). Briefly, all the image data obtained from the stretch test was loaded, and a range of thresholding parameters from 40 to 100 (min 0, max 255) were applied to the images for each tissue sample. The height was then quantified from the thresholded images as described above. An error term was quantified for each threshold value as the root-mean squared deviation (RMSD) divided by the slope of the best fitting line for the height of the last stretch cycle (pink in Figure 4.6). The optimal thresholding parameter was chosen as the one minimizing the error. The structure of the error term was to minimize RMSD to ensure a good linear fit while maximizing the slope of the fitted line. Maximizing the slope term was done to prevent the optimization algorithm from selecting a threshold value that gave a low RMSD but a little increase in height as the tissue is stretched. During development, it was found that only optimizing for low RMSD often resulted in overly aggressive thresholding which gave a near-flat height measure as the tissue was stretched. This optimization method gave an optimal thresholding parameter per sample for measuring the tissue dimensions from the front images. After each image was thresholded with the optimal parameter, the height was quantified as the average of the sum of vertical white pixels, and the width was quantified as the average of the sum of horizontal white pixels. Since the side images were obtained with a different camera and different lighting conditions, these images were thresholded manually, and the thickness at the reference configuration was similarly found as the average of the sum of the horizontal white pixels. In a uniaxial testing condition, the deformation gradient tensor is defined as

$$\mathbf{F} = \begin{bmatrix} \lambda_1 & 0 & 0 \\ 0 & \lambda_2 & 0 \\ 0 & 0 & \lambda_3 \end{bmatrix} \quad (4.1)$$

where λ_1 , λ_2 , and λ_3 represent the principal stretches and x_1 represents the direction of testing. The mechanical stretches are defined as

$$\lambda_1 = \frac{h}{h_0}, \quad \lambda_2 = \frac{w}{w_0}, \quad \lambda_3 = \frac{t}{t_0} = \frac{1}{\lambda_1 \lambda_2} \quad (4.2)$$

where h , w , and t represent the height, width, and thickness in the current configuration, h_0 , w_0 , and t_0 represent the height, width, and thickness in the reference configuration (i.e., at the start of the last loading cycle) in mm. The incompressibility hypothesis imposes $J = \det(\mathbf{F}) = 1$, which allows to calculate λ_3 as a function of λ_1 and λ_2 .

Next, the Cauchy stress tensor was calculated. The force F measured during the test was first zeroed by subtracting the minimum value measured, and then converted from grams to Newtons. The average cross-sectional area in the current configuration was quantified as $A = w \cdot t$ (units mm²). The Cauchy stress tensor was then defined as

$$\boldsymbol{\sigma} = \begin{bmatrix} F/A & 0 & 0 \\ 0 & 0 & 0 \\ 0 & 0 & 0 \end{bmatrix} \quad (4.3)$$

The stress and stretch along the direction of testing were then smoothed with a locally weighted scatterplot smoothing function (LOWESS, $\alpha = 0.4$).^{333,334} The circumference of the bladder rings was also quantified before stretching as 2×height. The volume of the ring was also obtained with the same 3D reconstruction method previously shown for the whole bladder pressurization. The front and side views were used with the shape-from-silhouette method to generate a volume reconstruction of the rings at each stretch interval. The stress and stretch results calculated by Equations (4.2) and (4.3) were plotted and statistically analyzed, specifically on the low stress part of the loading curve. The low stress region of the curves had to be used as not all of the bladder rings reached higher levels of stress.

A 3-way ANOVA was performed on both the circumference and stress-stretch data with independent variables of sex (male vs female), tissue type (cellular vs decellularized), and level of stretch (0, 10, 20, & 30%) with ordinary least squares.³³⁴

4.3 Results

The diameter of the bladder tissue rings at the start of each test (i.e., at the one-gram preload stage) was analyzed. The data used for the statistical analysis is plotted in Figure 4.7. The regression model revealed an $R^2 = 0.458$, $F(4, 24) = 22.6$, and $p < 0.0001$, which indicates that a significant proportion of the variance was explained by the model variables.

Sex, tissue type, and mechanical stretch coefficients were significant with all having $p < 0.001$. The interaction term was also significant having $p < 0.01$. Based on the statistics on the data collected here, female bladders can be expected to have a circumference 2.9 mm less than males, and decellularizing the bladder rings can be expected to increase the circumference by 2.79 mm. The interaction term being significant indicated that the effect of sex also depends on the tissue type. Specifically, the significant interaction term indicates that the difference between sexes is more pronounced for decellularized tissue than cellular tissue, as can be observed in Figure 4.7. Finally, the mechanical stretch coefficient being significant shows that after stretching the tissue by an increasing 10% amount, the circumference can be expected to increase by about 0.1 mm. This highlights how mechanical stretching alters the tissue's microstructural organization and the effect of sex and tissue type.

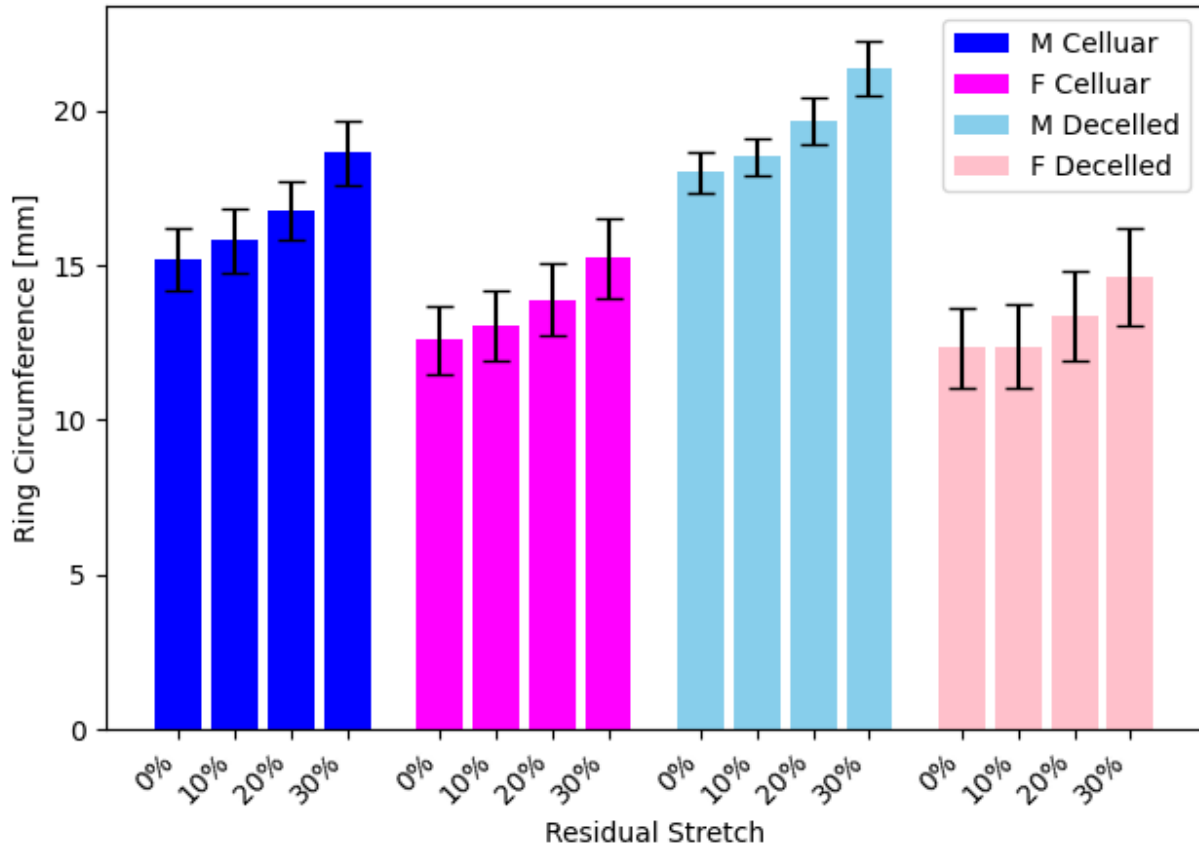


Figure 4.7: Bladder tissue ring circumference means (measured as 2×height from test imaging) measured at one-gram preload before each stretch test. Plot shows male (M), female (F), cellular, and decellularized tissue. Standard errors shown. The female tissue had smaller circumference on average than the male. Also, decellularized tissue had larger average circumference in males but not females.

The volume of the ring at the one-gram preload stage before each stretch test was found by the same reconstruction method as described for the 3D bladder pressurization methods. The results are shown by Figure 4.8. From this graph, it was found that the cellular tissue volume was more stable than the decellularized tissue volume as the tissue was progressively stretched. It can also be seen from Figure 4.8 that, before any stretching, the decellularized tissue had a larger volume compared to the cellular tissue in both sexes. Furthermore, with increased stretch, the average volume of the decellularized tissue decreased approaching the cellular average.

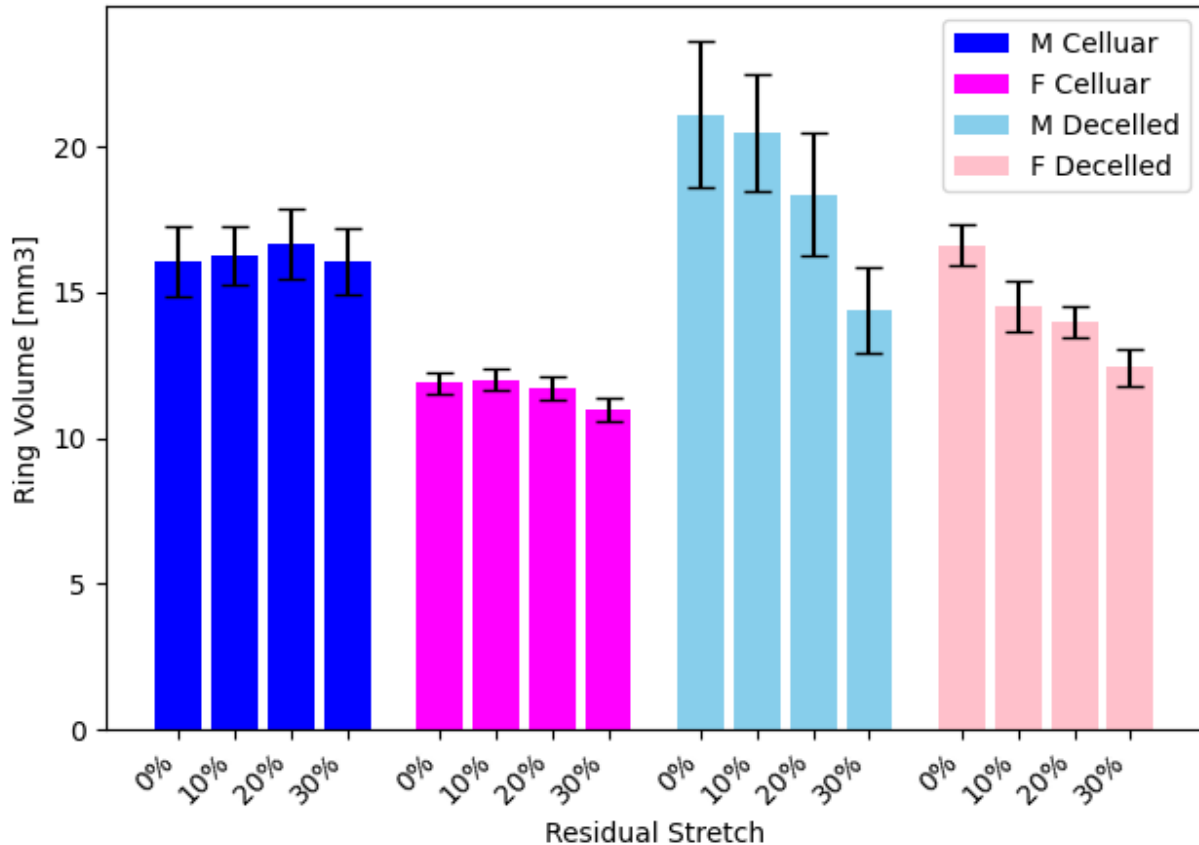


Figure 4.8: Mean volume of 3D reconstruction of ring at one-gram preload before each stretch test. It appeared that the cellular tissue volume was relatively stable as it was tested. Conversely, the decellularized tissue volume decreased with stretching. This trend appeared for both male (M) and female (F) tissues. Standard errors shown.

Finally, the first principal stress and stretches were plotted and analyzed with another 3-way ANOVA as done for the circumference results. Figure 4.9 shows the full plots of the stress-stretch results of the last loading cycle for the last stretch test, and Figure 4.10 shows the same data on a different scale to highlight the toe region (low stress) of the curves. As can be seen in Figure 4.9, not all the samples reached the expected linear region, so to compare the groups with the ANOVA, only the toe region (range from 0 kPa to 15 kPa) was used.

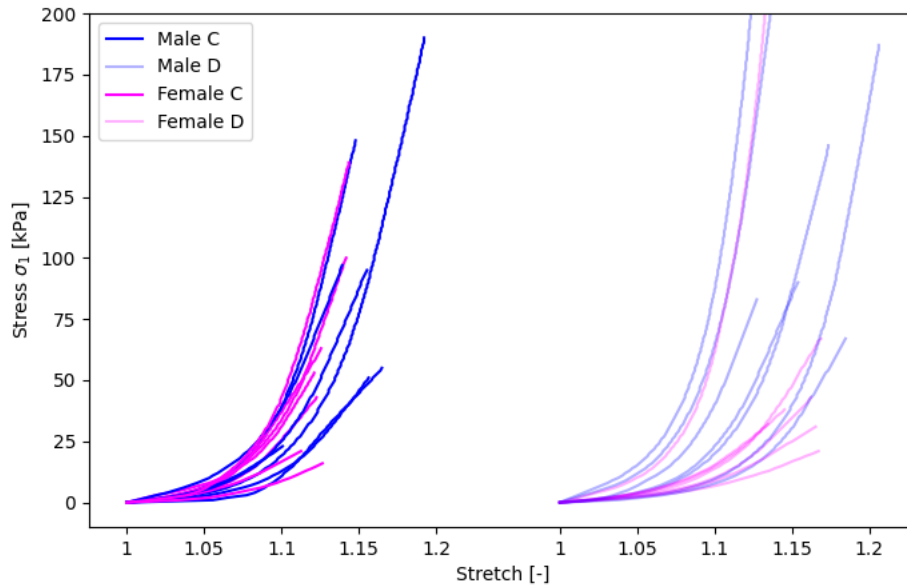


Figure 4.9: Cauchy stress and stretch collected from the last loading cycle of the last stretch test. The left full color curves show the results for the cellular (C) tissue, and the right translucent curves show the results for decellular (D) tissue. Note that that the samples do not all reach the same amount of stress/stretch due to limitations of the testing setup.

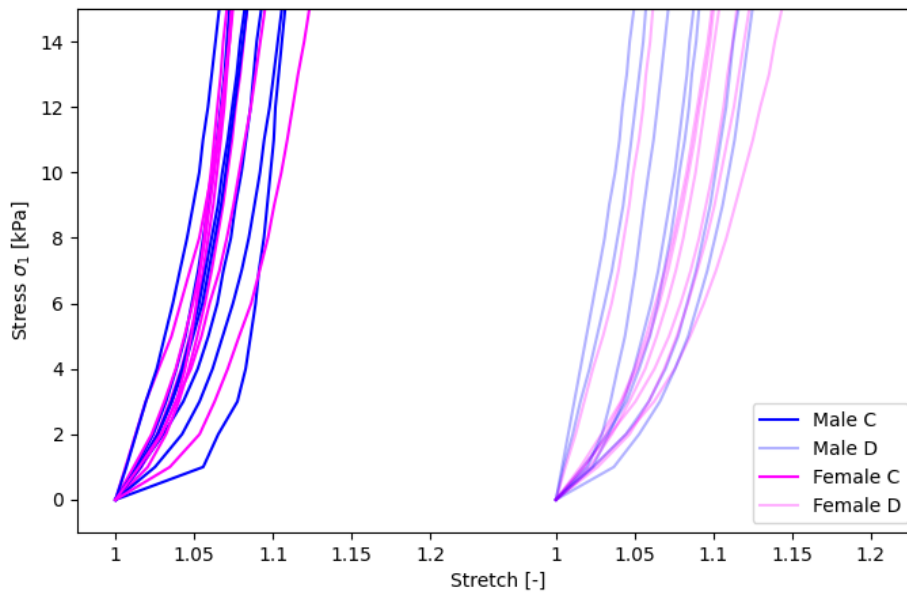


Figure 4.10: Same data as Figure 4.9 on a different scale to highlight the toe region of the curves used for 3-way ANOVA. The left full color curves show the results for the cellular (C) tissue, and the right translucent curves show the results for decellular (D) tissue.

A 3-way ANOVA was performed on the independent variables of sex (male vs female), tissue type (cellular vs decellularized), and level of stress (range 0 kPa to 15 kPa) with ordinary least squares. The regression model revealed an $R^2 = 0.626$, $F(4, 24) = 185$, and $p < 0.0001$, which indicates that a significant proportion of the variance was explained by the model variables.

Sex and tissue type were not significant in this model, however mechanical stress and the sex×tissue type interaction coefficients were significant with both having $p < 0.001$. This model revealed that sex and tissue type alone do not account for different mechanical stretch between the groups. However, the interaction term being significant highlights that the combination of sex and tissue type can show different mechanical behavior between groups. To explore the specific interaction effects, the same data was analyzed post-hoc with Tukey's test. The Tukey test revealed that the female cellular and decellular stress-stretch results were significantly different ($p < 0.05$), and that female and male decellular stress-stretch results were significantly different ($p < 0.05$). These results indicate that the female ECM has unique mechanical behavior among these groups. This can be qualitatively visualized in Figure 4.9 as the cellular male and female tissue appears clustered, while the female decellular tissue appears to have a lower stiffness compared to the decellular male.

4.4 Discussion

The ECM is largely responsible for the mechanical structure of the tissue as it is comprised of structural proteins including collagen and elastin.¹⁰⁷ The results presented here show that the decellularized tissue is different from the cellular state in both geometry and mechanical behavior. From the images in Figure 4.2, it was observed that the decellularized rings appeared larger than their cellular counterparts. This qualitative observation was validated by the circumference data. Figure 4.7 and the related statistical analyses showed that the decellular ring tissue indeed had a larger circumference. This may be due to the breakdown of the cellular structure, cell-ECM connections via integrins, and subsequent relaxation of the ECM.³³⁵ To summarize, it was found that, on average, female bladders had a smaller circumference than male bladders, and that decellularization had a smaller effect on the female bladders compared to the male group. These differences may be due to different cellular or ECM composition between the sexes.

Different geometry was also shown by Figure 4.8 where interesting trends in volume was observed with increased stretching. The cellular tissue volume was stable throughout the tests, while the ECM volume was larger prior to testing, and decreased with stretching to approach the

cellular average. The effect of reduced volume with progressive stretching for the decellularized tissue may be due to this tissue being more porous than cellular tissue, and increased stress causing fluid expulsion from the ECM. Since the ECM is hydrophilic³³⁶, the two-day long decellularization protocol may have saturated the tissue and increased its apparent volume. Since the cellular tissue did not have an extensive hydration period before testing, the tissue may have had less fluid volume contributing to its overall volume. So, the more stable volume results of the cellular tissue could be a result of better water retention, or lower hydration before testing, or a combination of these two factors. Thus, the constant volume assumption used in the methods appeared to be more valid for the cellular tissue than the decellularized.

Although significant differences due to sex and tissue type (C vs D) were found in the analysis of geometrical data, the mechanical stress-stretch results showed some but fewer differences. Statistical analysis of stress-stretch was only done on the toe region of the curves due to some samples not reaching high levels of stress. However, this low-stress region is still reasonable for defining the characteristics of the stress-stretch curve, since this non-linear regime is largely responsible for the overall shape of the curve, and at higher stresses, the plots become highly linear as shown by Figure 4.9. In comparing the toe region of the stress-stretch data, it was found that the female decellularized tissue was significantly different from the female cellular tissue, and the male decellular tissue. This result highlights the complexity of the sex-tissue structure interaction and its effects on the observed mechanical behavior. As stated earlier, this unique result may be due to different cellular or ECM composition between the sexes. The fact that no significant differences between the male cellular and decellular tissue mechanics was an interesting result, especially considering there were larger circumference differences between the two tissue types in males compared to females. The decellular tissue being oversaturated may have played a role in this outcome, as it has been previously shown that bladder tissue osmolarity effects its mechanics.⁹⁴

There were some notable limitations in the experimental setup. Most limitations were specific to the mechanical testing device used. Before testing, each sample was preloaded to one gram so that all the tissues started at a similar reference configuration. A stress-based preload is preferred to the load-based method, however the experimental setup did not allow for this. There were some limitations in the imaging method as well. The testing setup did not allow for simultaneous imaging of the front and side views of the tissue, although it is preferred. The side

images were only captured before each group of loading cycles, and an assumption (isochoric deformation) had to be made about the tissue. Simultaneous imaging from both sides would have allowed for more accurate stress calculations, as well as deeper analysis of the volume during testing. The final limitation of the experimental device was in the way the stretch was applied. As explained earlier, the device determines the height of the sample via thresholding, and then stretches the tissue to the target height based on the input stretch. As shown in Figure 4.9, not all the samples reached the same amount of stretch even though each had the same stretch input. This was likely due to using an un-optimized thresholding parameter, and system losses. It was for this reason that post-processing threshold optimization was developed. However, there was no way to optimize the threshold before the tissue was stretched so this limitation could not be overcome with the current device setup. Despite these limitations, notable differences between the tissue groups due to sex and decellularization were found.

Directions for future study include mechanical stretching with an improved uniaxial stretching device so achieve more robust mechanical results, biaxial stretching which better reflects the loading conditions of the bladder *in vivo*, and whole bladder pressurization of decellularized bladder tissues to further approach the *in vivo* load conditions.

4.5 Conclusion

The work here shows for the first time in mouse bladder tissue that decellularization affects the tissue geometry and mechanics in unique ways. This work supports the concept of testing and modeling tissue mechanics as a combination of the passive structural extracellular matrix and the active cellular components. Further investigation into the structural differences between the male and female bladder tissue may help explain the differences in geometry and mechanics observed here. The results of the current study show that decellularization affects the male and female mouse bladder tissue in different ways. Specifically, that the male ECM tissue rings had increased circumference, while a marginal decrease was observed in the female tissue. The female tissue also had smaller geometry in both circumference and volume compared to the males. Mechanical analysis showed that the female decellularized tissue was uniquely distinct from the other groups, which indicates an interaction effect of sex combined with decellularization. These results support the notion that sex differences on average are important to consider when studying physiology and tissue mechanics. Future work will develop improved testing methods to closer resemble *in vivo* conditions, as well as investigating the structural differences which are driving the results shown.

CHAPTER 5 SUMMARY

Quantitative metrics for bladder health are not well defined. Deeper research into the tissue mechanics of the bladder wall may provide a better characterization of bladder health and dysfunction. The thin-walled spherical pressure vessel model has long been used for modeling the mechanics of the bladder wall. There is a need for more detailed and descriptive mechanical models to be developed for more precise insight into the mechanical behavior of the bladder. The work presented in this dissertation works toward this goal by the development and implementation of a high fidelity 4D (space + time) reconstruction of the *ex vivo* bladder during pressurization. 4D reconstruction allowed implementation of a location specific mechanical model of the stresses on the bladder wall as well as more descriptive geometrical analysis.

From these advanced modeling techniques shown here, it was found that the bladder has anisotropic stretching behavior, and that the mechanical stresses at equivalent pressures are lower in the female bladder wall compared to male. Specifically, the bladder undergoes larger stretch in the circumferential direction than the longitudinal direction. This anisotropic behavior can only be exhibited with an accurate reconstruction of the bladder geometry, or with a spheroidal approximation. The sphere model that is often used to approximate bladder shape is not able to account for this unique directional mechanical stretching behavior. Additionally, it was found that for equivalent pressures above 6 mmHg, the female bladder wall exhibits lower mechanical stresses than the male bladder wall in both the spherical model and 3D mechanical models. Female bladders also had significantly smaller volumes compared to males at all pressures from 0 to 25 mmHg. Lastly, from the 4D modeling of bladder pressurization, it was found that female bladders also had lower compliance than males at pressure intervals of 5, 10, 15, and 20 mmHg. All taken together, these results illustrate how there are sex-specific mechanical behaviors of the murine bladder wall throughout pressurization.

Uniaxial testing of bladder tissues from the same cohort of mice used for the 4D pressurization experiments and modeling reflected more sex-specific geometrical and mechanical properties. Specifically, the circumference and volume of bladder ring sections were smaller for female tissue compared to male. Furthermore, decellularization had sex-specific effects on the geometry and mechanics of the bladder tissues. Male bladder ring tissues exhibited a larger

circumference after decellularization which was not observed for the female tissue. Finally, the female decellularized tissue had unique mechanical stretch and stress behavior compared to the male cellular, decellular, and female cellular tissues. Taken together, these bladder ring experimental results indicate that the female bladder may have microstructural differences compared to the male bladder which would be driving these observed differences. Accounting for sex-specific tissue properties is an important factor to consider for research on bladder health, dysfunction, and treatments.

The use of tissue mechanics in terms of understanding bladder function is limited in the literature. As tissue mechanics have had a significant impact on our understanding of other organs such as the brain, heart, and lungs, it seems imperative that there needs to be a greater focus on tissue mechanics of bladder to better characterize the function of this organ. The mechanics of the bladder deserve more attention, as the current urological methods for analyzing the bladder simply in terms of pressure and volume have not been able to tease out well-defined metrics for bladder health and disease. There is significant variation in clinical measures of bladder function in the healthy population, which may be able to be explained by inspection of the tissue-level mechanics, although this has yet to be fully explored.

Moreover, use of mouse models for studying bladder mechanics is currently underutilized in the literature. While results from animal models cannot be extrapolated directly to human applications, animal models are useful for development of basic knowledge and understanding of the bladder. Specifically, mice are powerful due to the models of gene modification and disease being widely standardized. Standard mouse models are valuable for studying the bladder in healthy and diseased conditions, as well as aiding in research reproducibility.

Biological sex is another factor that has been previously received less attention, although sex differences are increasingly appreciated in contemporary literature. Interestingly, physiological science has historically underrepresented female sex, but urology research has actually had a large focus on female sex due to substantial sex differences in the lower urinary tract. This has had the opposite effect where male sex has been underrepresented in urological research. Considering both sexes equally for biological research on the bladder is important for the development of gender-appropriate standards for health and treatments.

This current work shown is not without limitations. With regard to the bladder pressurization experiments, it was noticed that even after excision, not all the bladders were empty

when received for testing. The bladder being empty or having some degree of fullness would likely affect the results of the mechanical testing. A fuller bladder can be expected to have a greater degree of distensibility compared to an empty bladder, especially since the *ex vivo* bladders were tested the day after excision. In the future, quantifying the fullness of the *ex vivo* bladder before testing would give insight to the potential effects on the resulting mechanical behavior observed. Furthermore, the method of measuring thickness can be improved upon. With the current imaging technique, while the thickness of the bladder wall is visible, the thickness was typically 2 to 3 pixels thick. This is not a precise measure, and higher resolution imaging or a different thickness measure such as microscopy imaging would be beneficial.

With regard to the data analysis and reconstruction techniques, the segmentation method requires further refinement for future applications. In the development of automating image segmentation, a variety of image processing algorithms were explored, but all were found to be under-performing for the task. A machine learning method was instead implemented, but the neural network model was not sufficiently optimized for the task. It was found to perform better than the image processing algorithms, but the segmentations still required some manual repairs when the neural network performed poorly in some imaging conditions. Increasing the size of the training dataset, and further hyper-parameter optimization would likely be useful for improving the accuracy of the machine learning model so that less human intervention is required. Another area which requires further development is the visualization tooling. With the substantial amount of 3D data produced from the data analysis, visualizing this data is important. Inspection of the results would be vastly improved with better tools for viewing this 3D data.

Future work to build on the current methods presented here would include development of a method for tracking surface deformations of the bladder. Currently, as the bladders are segmented into binary images, all of the texture data from the imaging is lost. A 3D reconstruction method which accounts for the pixel texture of the bladders would open the door for both: more precise 3D reconstruction, and tracking surface deformations via digital image correlation techniques. Finally, as this work only studies the bladder mechanics in healthy mouse models, exploring the bladder mechanics of certain conditions such as aging, diabetes, or hormone replacement therapy would help draw better conclusions about healthy vs atypical bladder mechanics.

The work shown in this dissertation shows how the bladder has sex-specific mechanical behavior, which may be driven by microstructural sex differences. The sex differences in the

macrostructure of the lower urinary tract are well known. However, specifics about the microstructure of the bladder between the sexes are not well explored. Studying bladder function by accounting for the macro- and micro-level sex differences will likely be important for future research on bladder function and health. The results presented here are a step forward in illuminating the importance of bladder tissue mechanics and bladder wall microstructure as underleveraged drivers of bladder function.

BIBLIOGRAPHY

1. Stewart, W. *et al.* Prevalence and burden of overactive bladder in the United States. *World J Urol* **20**, 327–336 (2003).
2. Irwin, D. E. *et al.* Population-Based Survey of Urinary Incontinence, Overactive Bladder, and Other Lower Urinary Tract Symptoms in Five Countries: Results of the EPIC Study. *European Urology* **50**, 1306–1315 (2006).
3. Coyne, K. S. *et al.* The prevalence of lower urinary tract symptoms (LUTS) in the USA, the UK and Sweden: results from the Epidemiology of LUTS (EpiLUTS) study. *BJU International* **104**, 352–360 (2009).
4. Irwin, D. E., Kopp, Z. S., Agatep, B., Milsom, I. & Abrams, P. Worldwide prevalence estimates of lower urinary tract symptoms, overactive bladder, urinary incontinence and bladder outlet obstruction. *BJU International* **108**, 1132–1138 (2011).
5. Boyle, P. *et al.* The prevalence of lower urinary tract symptoms in men and women in four centres. The UrEpik study. *BJU International* **92**, 409–414 (2003).
6. Lightner, D. J., Gomelsky, A., Souter, L. & Vasavada, S. P. Diagnosis and Treatment of Overactive Bladder (Non-Neurogenic) in Adults: AUA/SUFU Guideline Amendment 2019. *J Urol* **202**, 558–563 (2019).
7. Cardoso, A. M. B., Lima, C. R. O. de P. & Ferreira, C. W. S. Prevalence of urinary incontinence in high-impact sports athletes and their association with knowledge, attitude and practice about this dysfunction. *European Journal of Sport Science* **18**, 1405–1412 (2018).
8. Brown, S. J., Donath, S., MacArthur, C., McDonald, E. A. & Krastev, A. H. Urinary incontinence in nulliparous women before and during pregnancy: prevalence, incidence, and associated risk factors. *Int Urogynecol J* **21**, 193–202 (2010).
9. Subak, L. L., Richter, H. E. & Hunskar, S. Obesity and urinary incontinence: epidemiology and clinical research update. *J Urol* **182**, S2-7 (2009).
10. Bardino, M., Di Martino, M., Ricci, E. & Parazzini, F. Frequency and Determinants of Urinary Incontinence in Adolescent and Young Nulliparous Women. *J Pediatr Adolesc Gynecol* **28**, 462–470 (2015).
11. D'Ancona, C. *et al.* The International Continence Society (ICS) report on the terminology for adult male lower urinary tract and pelvic floor symptoms and dysfunction. *Neurourology and Urodynamics* **38**, 433–477 (2019).
12. Leung, V. Y. *et al.* Nomograms of total renal volume, urinary bladder volume and bladder wall thickness index in 3,376 children with a normal urinary tract. *Pediatr Radiol* **37**, 181–188 (2007).
13. Lim, C. S. & Abrams, P. The Abrams-Griffiths nomogram. *World J Urol* **13**, 34–39 (1995).
14. Serati, M. *et al.* The bladder is an unreliable witness: The case for urodynamic investigations in female stress urinary incontinence. (2020).
15. Turner-Warwick, R., Whiteside, C. G., Worth, P. H. L., Milroy, E. J. G. & Bates, C. P. A Urodynamic View of the Clinical Problems associated with Bladder Neck Dysfunction and

- its Treatment by Endoscopic Incision and Trans-trigonal Posterior Prostatectomy¹. *British Journal of Urology* **45**, 44–59 (1973).
16. Chapple, C. R. *et al.* Lower Urinary Tract Symptoms Revisited: A Broader Clinical Perspective. *European Urology* **54**, 563–569 (2008).
 17. Blaivas, J. G. The bladder is an unreliable witness. *Neurourology and Urodynamics* **15**, 443–445 (1996).
 18. Pelosi, G., Faleiros, F., Pereira, M. R. C., Bimbatti, K. de F. & Tholl, A. D. Study on the prevalence of neurogenic bladder in Brazilians with traumatic and non-traumatic spinal cord injury. *The Journal of Spinal Cord Medicine* **0**, 1–5 (2021).
 19. Manack, A. *et al.* Epidemiology and healthcare utilization of neurogenic bladder patients in a us claims database. *Neurourology and Urodynamics* **30**, 395–401 (2011).
 20. Abrams, P. *Incontinence : 6th International Consultation on Incontinence, Tokyo, September 2016*. (International Continence Society, 2016).
 21. Lansang, R. S. & Krouskop, A. C. Bladder management. *EMedicine* (2004).
 22. Wyndaele, J. J. & Kovindha, A. *Urodynamic Testing After Spinal Cord Injury*. (Springer International Publishing, Cham, 2017). doi:10.1007/978-3-319-54900-2.
 23. *Neurological Aspects of Spinal Cord Injury*. (Springer International Publishing, Cham, 2017). doi:10.1007/978-3-319-46293-6.
 24. Bywater, M., Tornic, J., Mehnert, U. & Kessler, T. M. Detrusor Acontractility after Acute Spinal Cord Injury—Myth or Reality? *The Journal of Urology* **199**, 1565–1570 (2018).
 25. Welk, B. *et al.* Early urological care of patients with spinal cord injury. *World J Urol* **36**, 1537–1544 (2018).
 26. Arnold, E. P., Anthony, A., Fukui, J. & Utley, W. L. F. Bladder Function Following Spinal Cord Injury: a Urodynamic Analysis of the Outcome. *British Journal of Urology* **56**, 172–177 (1984).
 27. Wognum, S., Lagoa, C. E., Nagatomi, J., Sacks, M. S. & Vodovotz, Y. An Exploratory Pathways Analysis of Temporal Changes Induced by Spinal Cord Injury in the Rat Bladder Wall: Insights on Remodeling and Inflammation. *PLoS ONE* **4**, e5852 (2009).
 28. Tuttle, T. G., Lujan, H. L., Tykocki, N. R., DiCarlo, S. E. & Roccabianca, S. Remodeling of extracellular matrix in the urinary bladder of paraplegic rats results in increased compliance and delayed fiber recruitment 16 weeks after spinal cord injury. *Acta Biomaterialia* **141**, 280–289 (2022).
 29. Nagatomi, J., Gloeckner, D. C., Chancellor, M. B., deGroat, W. C. & Sacks, M. S. Changes in the Biaxial Viscoelastic Response of the Urinary Bladder Following Spinal Cord Injury. *Annals of Biomedical Engineering* **32**, 1409–1419 (2004).
 30. Toosi, K. K., Nagatomi, J., Chancellor, M. B. & Sacks, M. S. The Effects of Long-Term Spinal Cord Injury on Mechanical Properties of the Rat Urinary Bladder. *Ann Biomed Eng* **36**, 1470–1480 (2008).

31. Nagatomi, J., Toosi, K. K., Chancellor, M. B. & Sacks, M. S. Contribution of the extracellular matrix to the viscoelastic behavior of the urinary bladder wall. *Biomech Model Mechanobiol* **7**, 395–404 (2008).
32. Nagatomi, J., Getzenberg, R. H., Torimoto, K., Chancellor, M. B. & Sacks, M. S. Relationship between tissue composition and biomechanics of the urinary bladder: effects of spinal cord injury on bladder tissue. in *IEEE 30th Annual Northeast Bioengineering Conference, 2004. Proceedings of the* 162–163 (2004). doi:10.1109/NEBC.2004.1300045.
33. Lukacz, E. S. *et al.* A Novel Research Definition of Bladder Health in Women and Girls: Implications for Research and Public Health Promotion. *Journal of Women's Health* **27**, 974–981 (2018).
34. Wyman, J. F. *et al.* Normative noninvasive bladder function measurements in healthy women: A systematic review and meta-analysis. *Neurourology and Urodynamics* **39**, 507–522 (2020).
35. Sorel, M. R., Reitsma, H. J. B., Rosier, P. F. W. M., Bosch, R. J. L. H. R. & de Kort, L. M. O. Uroflowmetry in healthy women: A systematic review. *Neurourology and Urodynamics* **36**, 953–959 (2017).
36. Mahfouz, W., Al Afraa, T., Campeau, L. & Corcos, J. Normal urodynamic parameters in women. *Int Urogynecol J* **23**, 269–277 (2012).
37. Al Afraa, T., Mahfouz, W., Campeau, L. & Corcos, J. Normal lower urinary tract assessment in women: I. Uroflowmetry and post-void residual, pad tests, and bladder diaries. *Int Urogynecol J* **23**, 681–685 (2012).
38. Brostrom, S., Jennum, P. & Lose, G. Short-term reproducibility of cystometry and pressure-flow micturition studies in healthy women. *Neurourology and Urodynamics* **21**, 457–460 (2002).
39. Pauwels, E., De Wachter, S. & Wyndaele, J. J. Normality of bladder filling studied in symptom-free middle-aged women. *J Urol* **171**, 1567–1570 (2004).
40. De Wachter, S. & Wyndaele, J.-J. Frequency-volume charts: a tool to evaluate bladder sensation. *Neurourol Urodyn* **22**, 638–642 (2003).
41. Kassis, A. & Schick, E. Frequency-volume chart pattern in a healthy female population. *Br J Urol* **72**, 708–710 (1993).
42. Pfisterer, M. H.-D., Griffiths, D. J., Rosenberg, L., Schaefer, W. & Resnick, N. M. Parameters of bladder function in pre-, peri-, and postmenopausal continent women without detrusor overactivity. *Neurourol Urodyn* **26**, 356–361 (2007).
43. Altun, İ. & Cinar, N. D. Self-reported quantity of normal maximal voided volume in healthy young. *International Journal of Urological Nursing* **7**, 111–113 (2013).
44. Van Haarst, E. p., Heldeweg, E. a., Newling, D. w. & Schlatmann, T. j. The 24-h frequency-volume chart in adults reporting no voiding complaints: defining reference values and analysing variables. *BJU International* **93**, 1257–1261 (2004).
45. FitzGerald, M. P., Stablein, U. & Brubaker, L. Urinary habits among asymptomatic women. *American Journal of Obstetrics and Gynecology* **187**, 1384–1388 (2002).

46. Mueller, E. *et al.* Gender differences in 24-hour urinary diaries of asymptomatic north american adults. *Journal of Urology* **173**, 490–492 (2005).
47. Seseke, S. *et al.* Gender differences in voluntary micturition control — An fMRI study. *NeuroImage* **43**, 183–191 (2008).
48. Wyndaele, J. J. The normal pattern of perception of bladder filling during cystometry studied in 38 young healthy volunteers. *Journal of Urology* **160**, 479–481 (1998).
49. Pfisterer, M. H.-D., Griffiths, D. J., PhD, W. S. & Resnick, N. M. The Effect of Age on Lower Urinary Tract Function: A Study in Women. *Journal of the American Geriatrics Society* **54**, 405–412 (2006).
50. Kaynar, M. *et al.* The effect of bladder sensation on uroflowmetry parameters in healthy young men. *Neurourology and Urodynamics* **35**, 622–624 (2016).
51. Heeringa, R., de Wachter, S. G. G., van Kerrebroeck, P. E. V. & van Koeveringe, G. A. Normal bladder sensations in healthy volunteers: A focus group investigation. *Neurourology and Urodynamics* **30**, 1350–1355 (2011).
52. Ertberg, P., Møller, L. A. & Lose, G. A comparison of three methods to evaluate maximum bladder capacity: cystometry, uroflowmetry and a 24-h voiding diary in women with urinary incontinence. *Acta Obstetricia et Gynecologica Scandinavica* **82**, 374–377 (2003).
53. Wall, L. L., Wiskind, A. K. & Taylor, P. A. Simple bladder filling with a cough stress test compared with subtracted cystometry for the diagnosis of urinary incontinence. *American Journal of Obstetrics and Gynecology* **171**, 1472–1479 (1994).
54. Fonda, D., Brimage, P. J. & D’Astoli, M. Simple screening for urinary incontinence in the elderly: Comparison of simple and multichannel cystometry. *Urology* **42**, 536–540 (1993).
55. Blaivas, J. G., Groutz, A. & Verhaaren, M. Does the method of cystometry affect the incidence of involuntary detrusor contractions? A prospective randomized urodynamic study. *Neurourology and Urodynamics* **20**, 141–145 (2001).
56. D’Ancona, C. A. L., Gomes, M. J. & Rosier, P. F. W. M. ICS teaching module: Cystometry (basic module). *Neurourology and Urodynamics* **36**, 1673–1676 (2017).
57. Clausen, I., W. Tvedt, L. G. & Glott, T. Measurement of Urinary Bladder Pressure: A Comparison of Methods. *Sensors* **18**, 2128 (2018).
58. Homma, Y., Kondo, Y., Takahashi, S., Kitamura, T. & Kawabe, K. Reproducibility of Cystometry in Overactive Detrusor. *European Urology* **38**, 681–685 (2000).
59. Erdem, E. *et al.* How reliable are bladder perceptions during cystometry? *Neurourology and Urodynamics* **23**, 306–309 (2004).
60. Mitzner, W. MECHANICS OF THE LUNG IN THE 20TH CENTURY. *Compr Physiol* **1**, 2009–2027 (2011).
61. Faffe, D. S. & Zin, W. A. Lung Parenchymal Mechanics in Health and Disease. *Physiological Reviews* **89**, 759–775 (2009).
62. Suki, B. & Bates, J. H. T. Lung tissue mechanics as an emergent phenomenon. *Journal of Applied Physiology* **110**, 1111–1118 (2011).

63. Bates, P. *et al.* The standardization of terminology of lower urinary tract function. *Eur Urol* **2**, 274–276 (1976).
64. Toppercer, A. & Tetreault, J.-P. Compliance of the bladder: An attempt to establish normal values. *Urology* **14**, 204–205 (1979).
65. Wyndaele, J. j. *et al.* Bladder compliance what does it represent: Can we measure it, and is it clinically relevant? *Neurourology and Urodynamics* **30**, 714–722 (2011).
66. Gilmour, R. F. *et al.* A New Technique for Dynamic Analysis of Bladder Compliance. *Journal of Urology* **150**, 1200–1203 (1993).
67. Hennig, G. *et al.* Quantifying Whole Bladder Biomechanics Using the Novel Pentaplanar Reflected Image Macroscopy System. at <https://doi.org/10.21203/rs.3.rs-2214529/v1> (2022).
68. Johal, N. *et al.* Contractile function of detrusor smooth muscle from children with posterior urethral valves – The role of fibrosis. *Journal of Pediatric Urology* **17**, 100.e1-100.e10 (2021).
69. Brown, A. L. *et al.* 22 week assessment of bladder acellular matrix as a bladder augmentation material in a porcine model. *Biomaterials* **23**, 2179–2190 (2002).
70. Fry, C. H. *et al.* Fibrosis and the bladder, implications for function ICI-RS 2017. *Neurourology and Urodynamics* **37**, S7–S12 (2018).
71. Ferdinand Beer, E. Johnston, John DeWolf, & David Mazurek. *Mechanics of Materials*. (McGraw-Hill, 2019).
72. Nagle, A. S. *et al.* Quantification of bladder wall biomechanics during urodynamics: A methodologic investigation using ultrasound. *Journal of Biomechanics* **61**, 232–241 (2017).
73. le Feber, J., van Asselt, E. & van Mastrigt, R. Afferent bladder nerve activity in the rat: a mechanism for starting and stopping voiding contractions. *Urol Res* **32**, 395–405 (2004).
74. Colhoun, A. F. *et al.* A pilot study to measure dynamic elasticity of the bladder during urodynamics. *Neurourology and Urodynamics* **36**, 1086–1090 (2017).
75. Bright, E., Oelke, M., Tubaro, A. & Abrams, P. Ultrasound Estimated Bladder Weight and Measurement of Bladder Wall Thickness—Useful Noninvasive Methods for Assessing the Lower Urinary Tract? *The Journal of Urology* **184**, 1847–1854 (2010).
76. Blatt, A. H., Titus, J. & Chan, L. Ultrasound Measurement of Bladder Wall Thickness in the Assessment of Voiding Dysfunction. *The Journal of Urology* **179**, 2275–2279 (2008).
77. Oelke, M. International consultation on incontinence-research society (ICI-RS) report on non-invasive urodynamics: The need of standardization of ultrasound bladder and detrusor wall thickness measurements to quantify bladder wall hypertrophy. *Neurourology and Urodynamics* **29**, 634–639 (2010).
78. Serati, M. *et al.* Ultrasound measurement of bladder wall thickness in different forms of detrusor overactivity. *Int Urogynecol J* **21**, 1405–1411 (2010).
79. Kanyilmaz, S., Calis, F. A., Cinar, Y. & Akkoc, Y. Bladder wall thickness and ultrasound estimated bladder weight in healthy adults with portable ultrasound device. *J Res Med Sci* **18**, 103–106 (2013).

80. Watanabe, H., Akiyama, K., Saito, T. & Oki, F. A finite deformation theory of intravesical pressure and mural stress of the urinary bladder. *Tohoku J Exp Med* **135**, 301–307 (1981).
81. van Mastrigt, R., Koopal, J. W., Hak, J. & van de Wetering, J. Modeling the contractility of urinary bladder smooth muscle using isometric contractions. *Am J Physiol* **251**, R978-983 (1986).
82. Regnier, C. H., Kolsky, H., Richardson, P. D., Ghoniem, G. M. & Susset, J. G. The elastic behavior of the urinary bladder for large deformations. *Journal of Biomechanics* **16**, 915–922 (1983).
83. Laplace, P. S. *Œuvres complètes de Laplace*. (Gauthier-Villars, Paris, 1878).
84. Griffin, M., Premakumar, Y., Seifalian, A., Butler, P. E. & Szarko, M. Biomechanical Characterization of Human Soft Tissues Using Indentation and Tensile Testing. *JoVE (Journal of Visualized Experiments)* e54872 (2016) doi:10.3791/54872.
85. Holzapfel, G. A. *Biomechanics of Soft Tissue*. 15 (2000).
86. Vito, R. P. The mechanical properties of soft tissues—I: A mechanical system for bi-axial testing. *Journal of Biomechanics* **13**, 947–950 (1980).
87. Singh, G. & Chanda, A. Mechanical properties of whole-body soft human tissues: a review. *Biomed. Mater.* **16**, 062004 (2021).
88. B., A., Rao, S. & Pandya, H. J. Engineering approaches for characterizing soft tissue mechanical properties: A review. *Clinical Biomechanics* **69**, 127–140 (2019).
89. Navindaran, K., Kang, J. S. & Moon, K. Techniques for characterizing mechanical properties of soft tissues. *Journal of the Mechanical Behavior of Biomedical Materials* **138**, 105575 (2023).
90. Poladia, D. P. & Bauer, J. A. Functional, Structural, and Neuronal Alterations in Urinary Bladder during Diabetes: Investigations of a Mouse Model. *Pharmacology* **74**, 84–94 (2005).
91. Philyppov, I. B. *et al.* Impairment of urinary bladder mechanical properties in rat model of type 2 diabetes. *Neurourology and Urodynamics* **41**, 1670–1678 (2022).
92. Pak, K. J., Ostrom, R. S., Matsui, M. & Ehlert, F. J. Impaired M3 and enhanced M2 muscarinic receptor contractile function in a streptozotocin model of mouse diabetic urinary bladder. *Naunyn-Schmied Arch Pharmacol* **381**, 441–454 (2010).
93. Morales-Orcajo, E., Siebert, T. & Böhl, M. Location-dependent correlation between tissue structure and the mechanical behaviour of the urinary bladder. *Acta Biomaterialia* **75**, 263–278 (2018).
94. Tuttle, T., McClintock, D. & Roccabianca, S. Effects of swelling and anatomical location on the viscoelastic behavior of the porcine urinary bladder wall. *Journal of the Mechanical Behavior of Biomedical Materials* **143**, 105926 (2023).
95. Cardoza, R. J. Determining the Heterogeneous Properties of the Bladder Wall Using 3D-Analysis of the Whole Bladder. (University of Pittsburgh, United States -- Pennsylvania, 2022).

96. Wang, C. C. *et al.* Diabetes-induced Alterations in Biomechanical Properties of Urinary Bladder Wall in Rats. *Urology* **73**, 911–915 (2009).
97. Chang, M.-L., Li, H.-C., Liu, C.-K., Chiang, H.-S. & Hsu, C.-C. Novel Three-Dimensional Bladder Reconstruction Model from B-Mode Ultrasound Image to Improve the Accuracy of Bladder Volume Measurement. *Sensors* **21**, 4893 (2021).
98. Niu, H. *et al.* Reconstruction of 3D Bladder Model and Computation of Intra-Vesical Volume During Storing Based on Magnetic Resonance Imaging. in *2008 2nd International Conference on Bioinformatics and Biomedical Engineering* 1840–1842 (2008). doi:10.1109/ICBBE.2008.789.
99. Trostorf, R., Morales Orcajo, E., Pötzke, A., Siebert, T. & Böl, M. A pilot study on active and passive ex vivo characterisation of the urinary bladder and its impact on three-dimensional modelling. *Journal of the Mechanical Behavior of Biomedical Materials* **133**, 105347 (2022).
100. Mohammed, H. H. & Ali Lafta, H. A Combined Computational and Experimental Analysis on the Thickness of the Urinary Bladder Wall Layers during Filling Phase. in *2021 Sixth International Conference on Advances in Biomedical Engineering (ICABME)* 67–70 (2021). doi:10.1109/ICABME53305.2021.9604886.
101. Pewowaruk, R. *et al.* A pilot study of bladder voiding with real-time MRI and computational fluid dynamics. *PLoS ONE* **15**, e0238404 (2020).
102. Hirahara, N. *et al.* Four-Dimensional Ultrasonography for Dynamic Bladder Shape Visualization and Analysis During Voiding. *Journal of Ultrasound in Medicine* **25**, 307–313 (2006).
103. Parekh, A. *et al.* Ex vivo deformations of the urinary bladder wall during whole bladder filling: Contributions of extracellular matrix and smooth muscle. *Journal of Biomechanics* **43**, 1708–1716 (2010).
104. Makki, K., Bohi, A., Ogier, A. C. & Bellemare, M. E. Characterization of surface motion patterns in highly deformable soft tissue organs from dynamic MRI: An application to assess 4D bladder motion. *Computer Methods and Programs in Biomedicine* **218**, 106708 (2022).
105. Damaser, M. S. & Lehman, S. L. The effect of urinary bladder shape on its mechanics during filling. *Journal of Biomechanics* **28**, 725–732 (1995).
106. Gray, T. *et al.* Evaluation of bladder shape using transabdominal ultrasound: Feasibility of a novel approach for the detection of involuntary detrusor contractions. *Ultrasound* **27**, 167–175 (2019).
107. Dahms, Piechota, Dahiya, Lue, & Tanagho. Composition and biomechanical properties of the bladder acellular matrix graft: comparative analysis in rat, pig and human. *British Journal of Urology* **82**, 411–419 (1998).
108. Tuttle, T. G. *et al.* Investigation of Fiber-Driven Mechanical Behavior of Human and Porcine Bladder Tissue Tested Under Identical Conditions. *Journal of Biomechanical Engineering* **143**, (2021).

109. Wognum, S., Schmidt, D. E. & Sacks, M. S. On the Mechanical Role of De Novo Synthesized Elastin in the Urinary Bladder Wall. *Journal of Biomechanical Engineering* **131**, (2009).
110. Gilbert, T. W. *et al.* Collagen fiber alignment and biaxial mechanical behavior of porcine urinary bladder derived extracellular matrix. *Biomaterials* **29**, 4775–4782 (2008).
111. Gloeckner D. Claire *et al.* Passive Biaxial Mechanical Properties of the Rat Bladder Wall After Spinal Cord Injury. *Journal of Urology* **167**, 2247–2252 (2002).
112. Smith, P. P., DeAngelis, A. & Kuchel, G. A. Detrusor expulsive strength is preserved, but responsiveness to bladder filling and urinary sensitivity is diminished in the aging mouse. *American Journal of Physiology-Regulatory, Integrative and Comparative Physiology* **302**, R577–R586 (2012).
113. Zwaans, B. M. M., Grobbel, M., Carabulea, A. L., Lamb, L. E. & Roccabianca, S. Increased extracellular matrix stiffness accompanies compromised bladder function in a murine model of radiation cystitis. *Acta Biomaterialia* **144**, 221–229 (2022).
114. Lu, S.-H. *et al.* Biaxial mechanical properties of muscle-derived cell seeded small intestinal submucosa for bladder wall reconstitution. *Biomaterials* **26**, 443–449 (2005).
115. Kilborn, S. H., Trudel, G. & Uthoff, H. Review of Growth Plate Closure Compared with Age at Sexual Maturity and Lifespan in Laboratory Animals. **41**, (2002).
116. Bryda, E. C. The Mighty Mouse: The Impact of Rodents on Advances in Biomedical Research. *Mo Med* **110**, 207–211 (2013).
117. Mitchell, S. J., Scheibye-Knudsen, M., Longo, D. L. & de Cabo, R. Animal Models of Aging Research: Implications for Human Aging and Age-Related Diseases. *Annual Review of Animal Biosciences* **3**, 283–303 (2015).
118. Gurumurthy, C. B. & Lloyd, K. C. K. Generating mouse models for biomedical research: technological advances. *Disease Models & Mechanisms* **12**, dmm029462 (2019).
119. Dietz, H. C. & Mecham, R. P. Mouse models of genetic diseases resulting from mutations in elastic fiber proteins. *Matrix Biology* **19**, 481–488 (2000).
120. Perlman, R. L. Mouse models of human disease: An evolutionary perspective. *Evolution, Medicine, and Public Health* **2016**, 170–176 (2016).
121. Justice, M. J., Siracusa, L. D. & Stewart, A. F. Technical approaches for mouse models of human disease. *Disease Models & Mechanisms* **4**, 305–310 (2011).
122. Köks, S. *et al.* Mouse models of ageing and their relevance to disease. *Mechanisms of Ageing and Development* **160**, 41–53 (2016).
123. Bedell, M. A., Jenkins, N. A. & Copeland, N. G. Mouse models of human disease. Part I: Techniques and resources for genetic analysis in mice. *Genes & Development* (1997) doi:10.1101/gad.11.1.1.
124. Wang, H. & Dey, S. K. Roadmap to embryo implantation: clues from mouse models. *Nat Rev Genet* **7**, 185–199 (2006).
125. Platt, R. J. *et al.* CRISPR-Cas9 Knockin Mice for Genome Editing and Cancer Modeling. *Cell* **159**, 440–455 (2014).

126. Pelletier, S. Mouse Genome Engineering via CRISPR-Cas9 for Study of Immune Function. *Immunity Review* (2015) doi:10.1016/j.immuni.2015.01.004.
127. Chinwalla, A. T. *et al.* Initial sequencing and comparative analysis of the mouse genome. *Nature* **420**, 520–562 (2002).
128. Heppner, T. J., Hennig, G. W., Nelson, M. T. & Herrera, G. M. Afferent nerve activity in a mouse model increases with faster bladder filling rates in vitro, but voiding behavior remains unaltered in vivo. *American Journal of Physiology-Regulatory, Integrative and Comparative Physiology* **323**, R682–R693 (2022).
129. Korkmaz, I. & Rogg, B. A simple fluid-mechanical model for the prediction of the stress–strain relation of the male urinary bladder. *Journal of Biomechanics* **40**, 663–668 (2007).
130. Jost, S. P. Postnatal growth of the mouse bladder. *J Anat* **143**, 39–43 (1985).
131. Kumar, R., Pandey, A., Singh, A. & Verma, A. Performance of rice genotypes under low land ecosystems of Jharkhand. *Environment and Ecology* **31**, 1801-1805. (2013).
132. Tao, B. Empirical measurement of m&m’s Contained in a Standard Bottom Mouth Erlenmeyer Klein Flask and Comparison to Theoretical Models. *Acme Klein Bottle* https://www.kleinbottle.com/Bernie_Tao.htm (2001).
133. Durnin, L. *et al.* Urothelial purine release during filling of murine and primate bladders. *American Journal of Physiology-Renal Physiology* **311**, F708–F716 (2016).
134. Jackson, R. L. “The Uncertain Method of Drops”: How a Non-Uniform Unit Survived the Century of Standardization. *Perspectives on Science* **29**, 802–841 (2021).
135. Dörr, W. Cystometry in Mice—Influence of Bladder Filling Rate and Circadian Variations in Bladder Compliance. *The Journal of Urology* **148**, 183–187 (1992).
136. Veress, A. T., Chong, C. K., Field, L. J. & Sonnenberg, H. Blood pressure and fluid-electrolyte balance in ANF-transgenic mice on high- and low-salt diets. *Am J Physiol* **269**, R186-192 (1995).
137. Stewart, J. Diuretic responses to water-load in four strains of mice. *J Physiol* **198**, 355–363 (1968).
138. Drickamer, L. C. Rates of urine excretion by house mouse (*Mus domesticus*): Differences by age, sex, social status, and reproductive condition. *J Chem Ecol* **21**, 1481–1493 (1995).
139. Mingin, G. C. *et al.* Social stress in mice induces urinary bladder overactivity and increases TRPV1 channel-dependent afferent nerve activity. *Am J Physiol Regul Integr Comp Physiol* **309**, R629–R638 (2015).
140. Mingin, G. C., Peterson, A., Erickson, C. S., Nelson, M. T. & Vizzard, M. A. Social stress induces changes in urinary bladder function, bladder NGF content, and generalized bladder inflammation in mice. *American Journal of Physiology-Regulatory, Integrative and Comparative Physiology* **307**, R893–R900 (2014).
141. Chang, A. *et al.* Social stress in mice induces voiding dysfunction and bladder wall remodeling. *American Journal of Physiology-Renal Physiology* **297**, F1101–F1108 (2009).

142. Cornelissen, L. L., Misajet, B., Brooks, D. P. & Hicks, A. Influence of genetic background and gender on bladder function in the mouse. *Autonomic Neuroscience* **140**, 53–58 (2008).
143. Bjorling, D. E. *et al.* Evaluation of voiding assays in mice: impact of genetic strains and sex. *Am J Physiol Renal Physiol* **308**, F1369–F1378 (2015).
144. Yu, W. *et al.* Spontaneous voiding by mice reveals strain-specific lower urinary tract function to be a quantitative genetic trait. *American Journal of Physiology-Renal Physiology* **306**, F1296–F1307 (2014).
145. Chen, J., Drzewiecki, B. A., Merryman, W. D. & Pope, J. C. Murine bladder wall biomechanics following partial bladder obstruction. *Journal of Biomechanics* **46**, 2752–2755 (2013).
146. Hornsby, J. *et al.* Quantitative multiphoton microscopy of murine urinary bladder morphology during in situ uniaxial loading. *Acta Biomaterialia* **64**, 59–66 (2017).
147. Nishikawa, N. *et al.* Stretch- and carbachol-induced ATP release from bladder wall preparations of young and aged mice. *Neurourology and Urodynamics* **39**, 1644–1652 (2020).
148. Cheng, F. *et al.* A constrained mixture-micturition-growth (CMMG) model of the urinary bladder: Application to partial bladder outlet obstruction (BOO). *Journal of the Mechanical Behavior of Biomedical Materials* 105337 (2022) doi:10.1016/j.jmbbm.2022.105337.
149. Kierszenbaum, A. L. & Tres, L. *Histology and Cell Biology: An Introduction to Pathology E-Book*. (Elsevier Health Sciences, 2015).
150. Tykocki, N. R. & Monson, F. C. Excitability and contractility in arterioles and venules from the urinary bladder. *Curr Top Membr* **85**, 301–326 (2020).
151. Hossler, F. E., Lametschwandtner, A., Kao, R. & Finsterbusch, F. Microvascular Architecture of Mouse Urinary Bladder Described with Vascular Corrosion Casting, Light Microscopy, SEM, and TEM. *Microscopy and Microanalysis* **19**, 1428–1435 (2013).
152. Jezernik, K. & Pipan, N. Blood-urine barrier formation in mouse urinary bladder development. *The Anatomical Record* **235**, 533–538 (1993).
153. Lasič, E., Višnjar, T. & Kreft, M. E. Properties of the Urothelium that Establish the Blood–Urine Barrier and Their Implications for Drug Delivery. in *Reviews of Physiology, Biochemistry and Pharmacology* (eds. Nilius, B. *et al.*) 1–29 (Springer International Publishing, Cham, 2015). doi:10.1007/112_2015_22.
154. Gschwandtner, M. *et al.* Glycosaminoglycans are important mediators of neutrophilic inflammation *in vivo*. *Cytokine* **91**, 65–73 (2017).
155. Anand, M. *et al.* Estrogen Affects the Glycosaminoglycan Layer of the Murine Bladder. *Female Pelvic Med Reconstr Surg* **18**, 148–152 (2012).
156. Mathai, J. C. Hypercompliant Apical Membranes of Bladder Umbrella Cells. *Biophysical Journal* (2014).
157. Truschel, S. T. *et al.* Stretch-regulated Exocytosis/Endocytosis in Bladder Umbrella Cells. *MBoC* **13**, 830–846 (2002).

158. Sano, T. *et al.* Intravital imaging of mouse urothelium reveals activation of extracellular signal-regulated kinase by stretch-induced intravesical release of ATP. *Physiological Reports* **4**, e13033 (2016).
159. Vlaskovska, M. *et al.* P2X3 Knock-Out Mice Reveal a Major Sensory Role for Urothelially Released ATP. *J. Neurosci.* **21**, 5670–5677 (2001).
160. Mochizuki, T. *et al.* The TRPV4 Cation Channel Mediates Stretch-evoked Ca²⁺ Influx and ATP Release in Primary Urothelial Cell Cultures. *Journal of Biological Chemistry* **284**, 21257–21264 (2009).
161. Birder, L. A. *et al.* Altered urinary bladder function in mice lacking the vanilloid receptor TRPV1. *Nat Neurosci* **5**, 856–860 (2002).
162. Durnin, L. *et al.* An ex vivo bladder model with detrusor smooth muscle removed to analyse biologically active mediators released from the suburothelium. *The Journal of Physiology* **597**, 1467–1485 (2019).
163. Meng, E., Young, J. S. & Brading, A. F. Spontaneous activity of mouse detrusor smooth muscle and the effects of the urothelium. *Neurourology and Urodynamics* **27**, 79–87 (2008).
164. Canda, A., Chapple, C. & Chess-Williams, R. Pharmacologic responses of the mouse urinary bladder. *Open Medicine* **4**, 192–197 (2009).
165. Wuest, M., Kaden, S., Hakenberg, O. W., Wirth, M. P. & Ravens, U. Effect of rilmakalim on detrusor contraction in the presence and absence of urothelium. *Naunyn Schmied Arch Pharmacol* **372**, 203–212 (2005).
166. Eggena, P. Toad bladder compliance and water permeability in response to stretch. *American Journal of Physiology-Renal Physiology* **242**, F8–F16 (1982).
167. Staehelin, L. A. Structure and Function of Intercellular Junctions. in *International Review of Cytology* vol. 39 191–283 (Elsevier, 1974).
168. Phillips, J. I. & Davies, I. The comparative morphology of the bladder and urethra in young and old female C57BL/6 mice. *Experimental Gerontology* **15**, 551–562 (1980).
169. Nguyen, N. M. *et al.* Three-Dimensional Reconstruction of Neurovascular Network in Whole Mount Preparations and Thick-Cut Transverse Sections of Mouse Urinary Bladder. *World J Mens Health* **39**, 131–138 (2021).
170. Schueth, A., van, Z. M. A. M. J., Buurman, W. A. & van, K. G. A. Murine Bladder Imaging by 2-Photon Microscopy: An Experimental Study of Morphology. *Journal of Urology* **192**, 973–980 (2014).
171. Chai, T. C., Russo, A., Yu, S. & Lu, M. Mucosal signaling in the bladder. *Autonomic Neuroscience* **200**, 49–56 (2016).
172. Heppner, T. J., Tykocki, N. R., Hill-Eubanks, D. & Nelson, M. T. Transient contractions of urinary bladder smooth muscle are drivers of afferent nerve activity during filling. *Journal of General Physiology* **147**, 323–335 (2016).

173. Carpenter, F. G. Impairment and restoration of rat urinary bladder responsiveness following distension. *American Journal of Physiology-Regulatory, Integrative and Comparative Physiology* **244**, R106–R113 (1983).
174. Tykocki, N. R. *et al.* Development of stress-induced bladder insufficiency requires functional TRPV1 channels. *American Journal of Physiology-Renal Physiology* **315**, F1583–F1591 (2018).
175. Drake, M. J., Harvey, I. J., Gillespie, J. I. & Van Duyl, W. A. Localized contractions in the normal human bladder and in urinary urgency. *BJU International* **95**, 1002–1005 (2005).
176. Drake, M. J. *et al.* What are the origins and relevance of spontaneous bladder contractions? ICI-RS 2017. *Neurourology and Urodynamics* **37**, S13–S19 (2018).
177. Andersson, K.-E. & Arner, A. Urinary Bladder Contraction and Relaxation: Physiology and Pathophysiology. *Physiological Reviews* **84**, 935–986 (2004).
178. Ushiki, T. & Murakumo, M. Scanning Electron Microscopic Studies of Tissue Elastin Components Exposed by a KOH-Collagenase or Simple KOH Digestion Method. *Arch. Histol. Cytol.* **54**, 427–436 (1991).
179. Murakumo, M. *et al.* Three-Dimensional Arrangement of Collagen and Elastin Fibers in the Human Urinary Bladder: A Scanning Electron Microscopic Study. *Journal of Urology* **154**, 251–256 (1995).
180. Choi, J. K. THE FINE STRUCTURE OF THE URINARY BLADDER OF THE TOAD, BUFO MARINUS. *Journal of Cell Biology* **16**, 53–72 (1963).
181. Schueth, A., Spronck, B., van Zandvoort, M. A. M. J. & van Koeveeringe, G. A. Computer-assisted three-dimensional tracking of sensory innervation in the murine bladder mucosa with two-photon microscopy. *Journal of Chemical Neuroanatomy* **85**, 43–49 (2017).
182. Viana, R. *et al.* The development of the bladder trigone, the center of the anti-reflux mechanism. *Development* **134**, 3763–3769 (2007).
183. Carpenter, A. *et al.* 3-dimensional morphometric analysis of murine bladder development and dysmorphogenesis. *Developmental Dynamics* **241**, 522–533 (2012).
184. Tanagho, E. A. The Trigone: Anatomical and Physiological Considerations. 2. In Relation to the Bladder Neck. *The Journal of Urology* (1968) doi:10.1016/s0022-5347(17)62585-0.
185. Woodburne, R. T. Anatomy of the Bladder and Bladder Outlet. *The Journal of Urology* **100**, 474–487 (1968).
186. Korossis, S., Bolland, F., Southgate, J., Ingham, E. & Fisher, J. Regional biomechanical and histological characterisation of the passive porcine urinary bladder: Implications for augmentation and tissue engineering strategies. *Biomaterials* **30**, 266–275 (2009).
187. Hutch, J. A. The Internal Urinary Sphincter: A Double-Loop System. *The Journal of Urology* (1971) doi:10.1016/s0022-5347(17)61530-1.
188. Kleeman, F. J. The Physiology of the Internal Urinary Sphincter. *The Journal of Urology* (1970) doi:10.1016/S0022-5347(17)61779-8.

189. Yucel, S. & Baskin, L. S. An Anatomical Description of the Male and Female Urethral Sphincter Complex. *Journal of Urology* **171**, 1890–1897 (2004).
190. Woodburne, R. T. The Sphincter mechanism of the urinary bladder and the urethra. *The Anatomical Record* **141**, 11–20 (1961).
191. Sanghee Lee, Alonso Carrasco Jr, Randall B. Meacham, & Anna P. Malykhina. Transurethral Instillation Procedure in Adult Male Mouse. *Journal of Visualized Experiments* (2017) doi:10.3791/56663.
192. Duan, X. *et al.* Establishment of new transurethral catheterization methods for male mice. *Biology Methods and Protocols* **9**, bpae005 (2024).
193. Lamanna, O. K., Hsieh, M. H. & Forster, C. S. Novel catheter design enables transurethral catheterization of male mice. *American Journal of Physiology-Renal Physiology* **319**, F29–F32 (2020).
194. Smith, P. P. & Kuchel, G. A. Continuous uroflow cystometry in the urethane-anesthetized mouse. *Neurourology and Urodynamics* **29**, 1344–1349 (2010).
195. Yu, W. *et al.* Deletion of Mechanosensory β 1-integrin From Bladder Smooth Muscle Results in Voiding Dysfunction and Tissue Remodeling. *Function* **3**, zqac042 (2022).
196. Takezawa, K. *et al.* Combination of bladder ultrasonography and novel cystometry method in mice reveals rapid decrease in bladder capacity and compliance in LPS-induced cystitis. *American Journal of Physiology-Renal Physiology* **307**, F234–F241 (2014).
197. Pandita, R. K., Fujiwara, M., Alm, P. & Andersson, K.-E. CYSTOMETRIC EVALUATION OF BLADDER FUNCTION IN NON-ANESTHETIZED MICE WITH AND WITHOUT BLADDER OUTLET OBSTRUCTION. *The Journal of Urology* **164**, 1385–1389 (2000).
198. Cockayne, D. A. *et al.* Urinary bladder hyporeflexia and reduced pain-related behaviour in P2X3-deficient mice. *Nature* **407**, 1011–1015 (2000).
199. Daly, D., Rong, W., Chess-Williams, R., Chapple, C. & Grundy, D. Bladder afferent sensitivity in wild-type and TRPV1 knockout mice. *The Journal of Physiology* **583**, 663–674 (2007).
200. Rong, W., Spyer, K. M. & Burnstock, G. Activation and sensitisation of low and high threshold afferent fibres mediated by P2X receptors in the mouse urinary bladder. *The Journal of Physiology* **541**, 591–600 (2002).
201. Lemack, G. E. *et al.* Altered bladder function in transgenic mice expressing rat elastin. *Neurourology and Urodynamics* **18**, 55–68 (1999).
202. Ottensmeyer, M. P., Kerdok, A. E., Howe, R. D. & Dawson, S. L. The Effects of Testing Environment on the Viscoelastic Properties of Soft Tissues. in *Medical Simulation* (eds. Cotin, S. & Metaxas, D.) 9–18 (Springer, Berlin, Heidelberg, 2004). doi:10.1007/978-3-540-25968-8_2.
203. Saber-Sheikh, K., Clarke, R. L. & Braden, M. Viscoelastic properties of some soft lining materials: I—effect of temperature. *Biomaterials* **20**, 817–822 (1999).

204. Hosseini, S. M., Wilson, W., Ito, K. & van Donkelaar, C. C. How preconditioning affects the measurement of poro-viscoelastic mechanical properties in biological tissues. *Biomech Model Mechanobiol* **13**, 503–513 (2014).
205. Fung, Y. C. On mathematical models of stress-strain relationship for living soft tissues. 15 (1975).
206. Ansermet, C. *et al.* The intrinsic circadian clock in podocytes controls glomerular filtration rate. *Sci Rep* **9**, 16089 (2019).
207. Saitoh, M. *et al.* Mechanical Properties and Modeling of the Stress-Strain Behavior of the Urinary Bladder In Vivo. (1994) doi:10.1520/STP18112S.
208. Lundbeck, F., Djurhuus, J. Chr. & Vaeth, M. Bladder Filling in Mice: An Experimental in Vivo Model to Evaluate the Reservoir Function of the Urinary Bladder in a Long Term Study. *The Journal of Urology* **141**, 1245–1249 (1989).
209. Pieter Uvin *et al.* The Use of Cystometry in Small Rodents: A Study of Bladder Chemosensation. *Journal of Visualized Experiments* (2012) doi:doi:10.3791/3869.
210. Aizawa, N. & Fujita, T. Comparison of the effects of two anesthetics, isoflurane and urethane, on bladder function in rats. *Journal of Pharmacological Sciences* **152**, 144–150 (2023).
211. Chang, H.-Y. & Havton, L. A. Differential effects of urethane and isoflurane on external urethral sphincter electromyography and cystometry in rats. *American Journal of Physiology-Renal Physiology* **295**, F1248–F1253 (2008).
212. Longhurst, P. A., Eika, B., Leggett, R. E. & Levin, R. M. Urinary Bladder Function in the Tight-Skin Mouse. *The Journal of Urology* **148**, 1611–1614 (1992).
213. Damaser, M. S. Whole Bladder Mechanics during Filling. *Scandinavian Journal of Urology and Nephrology* **33**, 51–58 (1999).
214. van Mastrigt, R., Coolsaet, B. L. R. A. & van Duyl, W. A. Passive properties of the urinary bladder in the collection phase. *Med. Biol. Eng. Comput.* **16**, 471–482 (1978).
215. van Beek, A. J. A finite element model of the urinary bladder.
216. Schüle, J. *et al.* Multi-Physical Tissue Modeling of a Human Urinary Bladder. in *2021 43rd Annual International Conference of the IEEE Engineering in Medicine & Biology Society (EMBC)* 4297–4302 (2021). doi:10.1109/EMBC46164.2021.9629482.
217. Mattiasson, A. & Uvelius, B. Changes in contractile properties in hypertrophic rat urinary bladder. *J Urol* **128**, 1340–1342 (1982).
218. Basford, J. R. The Law of Laplace and its relevance to contemporary medicine and rehabilitation. *Archives of Physical Medicine and Rehabilitation* **83**, 1165–1170 (2002).
219. Richard Budynas & Keith Nisbett. *Shigley's Mechanical Engineering Design*. (McGraw-Hill, 2019).
220. Ronchi, F. *et al.* Experimental study on bladder Wall's strain in vesical function. *Urol. Res.* **10**, 285–291 (1982).

221. Monteiro, V. S. A. Computational model of the human urinary bladder. *TDX (Tesis Doctorals en Xarxa)* (Universitat Politècnica de Catalunya, 2013).
222. Sadd, M. H. *Elasticity: Theory, Applications, and Numerics*. (Elsevier, 2010).
223. Weiss, J. A., Maker, B. N. & Govindjee, S. Finite element implementation of incompressible, transversely isotropic hyperelasticity. *Computer Methods in Applied Mechanics and Engineering* **135**, 107–128 (1996).
224. Roccabianca, S. & Bush, T. R. Understanding the mechanics of the bladder through experiments and theoretical models: Where we started and where we are heading. *Technology* **04**, 30–41 (2016).
225. Chagnon, G., Rebouah, M. & Favier, D. Hyperelastic Energy Densities for Soft Biological Tissues: A Review. *J Elast* **120**, 129–160 (2015).
226. Guimarães, C. F., Gasperini, L., Marques, A. P. & Reis, R. L. The stiffness of living tissues and its implications for tissue engineering. *Nat Rev Mater* **5**, 351–370 (2020).
227. Khaniki, H. B., Ghayesh, M. H., Chin, R. & Amabili, M. Hyperelastic structures: A review on the mechanics and biomechanics. *International Journal of Non-Linear Mechanics* **148**, 104275 (2023).
228. *Tissue Mechanics*. (Springer, New York, NY, 2007). doi:10.1007/978-0-387-49985-7.
229. Jokandan, M. S. *et al.* Bladder wall biomechanics: A comprehensive study on fresh porcine urinary bladder. *Journal of the Mechanical Behavior of Biomedical Materials* **79**, 92–103 (2018).
230. Natali, A. N. *et al.* Bladder tissue biomechanical behavior: Experimental tests and constitutive formulation. *Journal of Biomechanics* **48**, 3088–3096 (2015).
231. Gasser, T. C., Ogden, R. W. & Holzapfel, G. A. Hyperelastic modelling of arterial layers with distributed collagen fibre orientations. *J R Soc Interface* **3**, 15–35 (2006).
232. Holzapfel, G. A., Gasser, T. C. & Ogden, R. W. A New Constitutive Framework for Arterial Wall Mechanics and a Comparative Study of Material Models. *Journal of Elasticity* **61**, 1–48 (2000).
233. Ogden. Large deformation isotropic elasticity: on the correlation of theory and experiment for compressible rubberlike solids. *Proc. R. Soc. Lond. A* **328**, 567–583 (1972).
234. Rust, W. *Non-Linear Finite Element Analysis in Structural Mechanics*. (Springer, 2015).
235. Rivlin, R. S. & Rideal, E. K. Large elastic deformations of isotropic materials IV. further developments of the general theory. *Philosophical Transactions of the Royal Society of London. Series A, Mathematical and Physical Sciences* **241**, 379–397 (1997).
236. Mooney, M. A Theory of Large Elastic Deformation. *Journal of Applied Physics* **11**, 582–592 (1940).
237. Treloar, L. R. G. The elasticity of a network of long-chain molecules—II. *Trans. Faraday Soc.* **39**, 241–246 (1943).

238. Sheta, B., Elhabiby, M. & El-Sheimy, N. COMPARISON AND ANALYSIS OF NONLINEAR LEAST SQUARES METHODS FOR VISION BASED NAVIGATION (VBN) ALGORITHMS. (2012).
239. Artzy, E., Frieder, G. & Herman, G. T. The theory, design, implementation and evaluation of a three-dimensional surface detection algorithm. *Computer Graphics and Image Processing* **15**, 1–24 (1981).
240. Herman, G. T. & Liu, H. K. Three-dimensional display of human organs from computed tomograms. *Computer Graphics and Image Processing* **9**, 1–21 (1979).
241. Herman, G. T. & Coin, C. G. The use of three-dimensional computer display in the study of disk disease. *J Comput Assist Tomogr* **4**, 564–567 (1980).
242. Glenn, W. V. J. *et al.* Multiplanar Display Computerized Body Tomography Applications in the Lumbar Spine. *Spine* **4**, 282 (1979).
243. Altschuler, M. D. *et al.* Demonstration of a software package for the reconstruction of the dynamically changing structure of the human heart from cone beam X-ray projections. *J Med Syst* **4**, 289–304 (1980).
244. Levoy, M. Display of surfaces from volume data. *IEEE Computer Graphics and Applications* **8**, 29–37 (1988).
245. Herman, G. T. & Liu, H. K. Dynamic boundary surface detection. *Computer Graphics and Image Processing* **7**, 130–138 (1978).
246. Cardenas, C. E., Yang, J., Anderson, B. M., Court, L. E. & Brock, K. B. Advances in Auto-Segmentation. *Seminars in Radiation Oncology* **29**, 185–197 (2019).
247. Srihari, S. N. Representation of Three-Dimensional Digital Images. *ACM Comput. Surv.* **13**, 399–424 (1981).
248. Nyquist, H. Certain Factors Affecting Telegraph Speed. *Transactions of the American Institute of Electrical Engineers* **XLIII**, 412–422 (1924).
249. Shannon, C. E. Communication in the Presence of Noise. *Proceedings of the IRE* **37**, 10–21 (1949).
250. Pipe, J. G. Reconstructing MR images from undersampled data: Data-weighting considerations. *Magnetic Resonance in Medicine* **43**, 867–875 (2000).
251. Joseph, P. M. Sampling errors in projection reconstruction MRI. *Magnetic Resonance in Medicine* **40**, 460–466 (1998).
252. Hyun, C. M., Kim, H. P., Lee, S. M., Lee, S. & Seo, J. K. Deep learning for undersampled MRI reconstruction. *Phys. Med. Biol.* **63**, 135007 (2018).
253. Baker, H. Three-dimensional modelling. in *Proceedings of the 5th international joint conference on Artificial intelligence - Volume 2* 649–655 (Morgan Kaufmann Publishers Inc., San Francisco, CA, USA, 1977).
254. Chien, C. H. & Aggarwal, J. K. Volume/surface octrees for the representation of three-dimensional objects. *Computer Vision, Graphics, and Image Processing* **36**, 100–113 (1986).

255. Martin, W. N. & Aggarwal, J. K. Volumetric Descriptions of Objects from Multiple Views. *IEEE Transactions on Pattern Analysis and Machine Intelligence* **PAMI-5**, 150–158 (1983).
256. Pavlidis, G., Koutsoudis, A., Arnaoutoglou, F., Tsioukas, V. & Chamzas, C. Methods for 3D digitization of Cultural Heritage. *Journal of Cultural Heritage* **8**, 93–98 (2007).
257. Baraniuk, R. G. *et al.* Compressive Video Sensing: Algorithms, architectures, and applications. *IEEE Signal Processing Magazine* **34**, 52–66 (2017).
258. Stanković, V., Stanković, L. & Cheng, S. Compressive image sampling with side information. in *2009 16th IEEE International Conference on Image Processing (ICIP)* 3037–3040 (2009). doi:10.1109/ICIP.2009.5414408.
259. Lorensen, W. E. & Cline, H. E. Marching cubes: A high resolution 3D surface construction algorithm. *SIGGRAPH Comput. Graph.* **21**, 163–169 (1987).
260. Chernyaev, E. V. Marching Cubes 33: Construction of Topologically Correct Isosurfaces.
261. Lewiner, T., Lopes, H., Vieira, A. W. & Tavares, G. Efficient Implementation of Marching Cubes' Cases with Topological Guarantees. *Journal of Graphics Tools* **8**, 1–15 (2003).
262. Lorensen, W. E. Marching through the Visible Man. in *Proceedings Visualization '95* 368–373 (1995). doi:10.1109/VISUAL.1995.485154.
263. Du, Q. & Wang, D. Tetrahedral mesh generation and optimization based on centroidal Voronoi tessellations. *International Journal for Numerical Methods in Engineering* **56**, 1355–1373 (2003).
264. Lévy, B. & Liu, Y. Lp Centroidal Voronoi Tessellation and its applications. *ACM Trans. Graph.* **29**, 119:1-119:11 (2010).
265. Alliez, P., Cohen-Steiner, D., Tong, Y. & Desbrun, M. Voronoi-based Variational Reconstruction of Unoriented Point Sets.
266. Chew, L. P. Guaranteed-quality mesh generation for curved surfaces. in *Proceedings of the ninth annual symposium on Computational geometry* 274–280 (Association for Computing Machinery, New York, NY, USA, 1993). doi:10.1145/160985.161150.
267. Ruppert, J. A Delaunay Refinement Algorithm for Quality 2-Dimensional Mesh Generation. *Journal of Algorithms* **18**, 548–585 (1995).
268. Cohen-Steiner, D., de Verdière, É. C. & Yvinec, M. Conforming Delaunay triangulations in 3D. in *Proceedings of the eighteenth annual symposium on Computational geometry* 199–208 (Association for Computing Machinery, New York, NY, USA, 2002). doi:10.1145/513400.513425.
269. Rineau, L. & Yvinec, M. A generic software design for Delaunay refinement meshing. *Computational Geometry* **38**, 100–110 (2007).
270. Koomey, J., Berard, S., Sanchez, M. & Wong, H. Implications of Historical Trends in the Electrical Efficiency of Computing. *IEEE Annals of the History of Computing* **33**, 46–54 (2011).

271. Hadjiiski, L. *et al.* Automated segmentation of urinary bladder and detection of bladder lesions in multi-detector row CT urography. in *Medical Imaging 2009: Computer-Aided Diagnosis* vol. 7260 1083–1089 (SPIE, 2009).
272. Halilaj, E. *et al.* Machine learning in human movement biomechanics: Best practices, common pitfalls, and new opportunities. *Journal of Biomechanics* **81**, 1–11 (2018).
273. Vento, D. D. & Fanfarillo, A. Traps, Pitfalls and Misconceptions of Machine Learning applied to Scientific Disciplines. in *Proceedings of the Practice and Experience in Advanced Research Computing on Rise of the Machines (learning)* 1–8 (Association for Computing Machinery, New York, NY, USA, 2019). doi:10.1145/3332186.3332209.
274. Weese, J. & Lorenz, C. Four challenges in medical image analysis from an industrial perspective. *Medical Image Analysis* **33**, 44–49 (2016).
275. Duncan, J. S. & Ayache, N. Medical image analysis: progress over two decades and the challenges ahead. *IEEE Transactions on Pattern Analysis and Machine Intelligence* **22**, 85–106 (2000).
276. Gsaxner, C., Roth, P. M., Wallner, J. & Egger, J. Exploit fully automatic low-level segmented PET data for training high-level deep learning algorithms for the corresponding CT data. *PLOS ONE* **14**, e0212550 (2019).
277. Xiao, C. *et al.* RefineNet-based 2D and 3D automatic segmentations for clinical target volume and organs at risks for patients with cervical cancer in postoperative radiotherapy. *Journal of Applied Clinical Medical Physics* **23**, e13631 (2022).
278. Akkus, Z. *et al.* Fully Automated Segmentation of Bladder Sac and Measurement of Detrusor Wall Thickness from Transabdominal Ultrasound Images. *Sensors* **20**, 4175 (2020).
279. Balagopal, A. *et al.* Fully automated organ segmentation in male pelvic CT images. *Phys Med Biol* **63**, 245015 (2018).
280. Ma, X. *et al.* U-Net based deep learning bladder segmentation in CT urography. *Medical Physics* **46**, 1752–1765 (2019).
281. Dai, W. *et al.* CAN3D: Fast 3D medical image segmentation via compact context aggregation. *Medical Image Analysis* **82**, 102562 (2022).
282. Xu, X., Zhou, F. & Liu, B. Automatic bladder segmentation from CT images using deep CNN and 3D fully connected CRF-RNN. *Int J CARS* **13**, 967–975 (2018).
283. Fournelle, M. *et al.* Portable Ultrasound Research System for Use in Automated Bladder Monitoring with Machine-Learning-Based Segmentation. *Sensors* **21**, 6481 (2021).
284. Albawi, S., Mohammed, T. A. & Al-Zawi, S. Understanding of a convolutional neural network. in *2017 International Conference on Engineering and Technology (ICET)* 1–6 (2017). doi:10.1109/ICEngTechnol.2017.8308186.
285. Yin, M., Vaughan, J. W. & Wallach, H. Understanding the Effect of Accuracy on Trust in Machine Learning Models. (2019).

286. Nagle, A. S. *et al.* Comparison of 2D and 3D ultrasound methods to measure serial bladder volumes during filling: Steps toward development of non-invasive ultrasound urodynamics. *Bladder (San Franc)* **5**, e32 (2018).
287. Suwanrath, C., Suntharasaj, T., Sirapatanapipat, H. & Geater, A. Three-Dimensional Ultrasonographic Bladder Volume Measurement: Reliability of the Virtual Organ Computer-Aided Analysis Technique Using Different Rotation Steps. *Journal of Ultrasound in Medicine* **28**, 847–854 (2009).
288. Vinod, N. N. *et al.* Bladder volume correction factors measured with 3D ultrasound and BladderScan. *Can J Urol* **26**, 9829–9834 (2019).
289. Fananapazir, G., Kitich, A., Lamba, R., Stewart, S. L. & Corwin, M. T. Normal reference values for bladder wall thickness on CT in a healthy population. *Abdom Radiol (NY)* **43**, 2442–2445 (2018).
290. Riccabona, M., Nelson, T. R. & Pretorius, D. H. Three-dimensional ultrasound: accuracy of distance and volume measurements. *Ultrasound in Obstetrics & Gynecology* **7**, 429–434 (1996).
291. Zhang, Y., Duan, C., Ye, D. & Liang, Z. The segmentation of MR bladder wall in 3D based on minimum closed set model. in *2013 IEEE International Conference on Medical Imaging Physics and Engineering* 319–323 (2013). doi:10.1109/ICMIPE.2013.6864560.
292. Ogier, A. C., Rapacchi, S., Troter, A. L. & Bellemare, M.-E. 3D Dynamic MRI for Pelvis Observation - a First Step. in *2019 IEEE 16th International Symposium on Biomedical Imaging (ISBI 2019)* 1801–1804 (IEEE, Venice, Italy, 2019). doi:10.1109/ISBI.2019.8759589.
293. Soper, T. D., Porter, M. P. & Seibel, E. J. Surface mosaics of the bladder reconstructed from endoscopic video for automated surveillance. *IEEE Trans Biomed Eng* **59**, 1670–1680 (2012).
294. Lurie, K. L., Angst, R., Zlatev, D. V., Liao, J. C. & Bowden, A. K. E. 3D reconstruction of cystoscopy videos for comprehensive bladder records. *Biomed. Opt. Express, BOE* **8**, 2106–2123 (2017).
295. Rosa, B. M. G. & Yang, G. Z. Bladder Volume Monitoring Using Electrical Impedance Tomography With Simultaneous Multi-Tone Tissue Stimulation and DFT-Based Impedance Calculation Inside an FPGA. *IEEE Transactions on Biomedical Circuits and Systems* **14**, 775–786 (2020).
296. Andrikos, I. *et al.* EDIT Software: A tool for the semi-automatic 3D reconstruction of bladder cancer and urinary bladder of animal models. *Computer Methods and Programs in Biomedicine* **232**, 107448 (2023).
297. Griffiths, D. Imaging bladder sensations. *Neurourology and Urodynamics* **26**, 899–903 (2007).
298. Nenadic, I. *et al.* Noninvasive Evaluation of Bladder Wall Mechanical Properties as a Function of Filling Volume: Potential Application in Bladder Compliance Assessment. *PLOS ONE* (2016).

299. Chai, X., van Herk, M., Hulshof, M. C. C. M. & Bel, A. A voxel-based finite element model for the prediction of bladder deformation. *Medical Physics* **39**, 55–65 (2012).
300. Costa, M. J., Delingette, H., Novellas, S. & Ayache, N. Automatic Segmentation of Bladder and Prostate Using Coupled 3D Deformable Models. in *Medical Image Computing and Computer-Assisted Intervention – MICCAI 2007* (eds. Ayache, N., Ourselin, S. & Maeder, A.) 252–260 (Springer, Berlin, Heidelberg, 2007). doi:10.1007/978-3-540-75757-3_31.
301. Ronneberger, O., Fischer, P. & Brox, T. U-Net: Convolutional Networks for Biomedical Image Segmentation. in *Medical Image Computing and Computer-Assisted Intervention – MICCAI 2015* 234–241 (Springer, 2015). doi:10.1007/978-3-319-24574-4_28.
302. milesial. *Milesial/Pytorch-UNet*. (2024).
303. Laurentini, A. The visual hull concept for silhouette-based image understanding. *IEEE Transactions on Pattern Analysis and Machine Intelligence* **16**, 150–162 (1994).
304. Virtanen, P. *et al.* SciPy 1.0: fundamental algorithms for scientific computing in Python. *Nat Methods* **17**, 261–272 (2020).
305. Vollmer, J., Mencl, R. & Müller, H. Improved Laplacian Smoothing of Noisy Surface Meshes. *Computer Graphics Forum* **18**, 131–138 (1999).
306. Dawson-Haggerty, M. *Mikedh/Trimesh*. (2024).
307. Wadell, H. Volume, Shape, and Roundness of Quartz Particles. *The Journal of Geology* **43**, 250–280 (1935).
308. Panozzo, D., Puppo, E. & Rocca, L. Efficient Multi-scale Curvature and Crease Estimation. *Panozzo, Daniele, Enrico Puppo, and Luigi Rocca. 'Efficient multi-scale curvature and crease estimation.'* 2nd International Workshop on Computer Graphics, Computer Vision and Mathematics, *GraVisMa* (2010).
309. *Libigl/Libigl-Python-Bindings*. (libigl dev team, 2024).
310. Porteous, I. R. *Geometric Differentiation: For the Intelligence of Curves and Surfaces*. (Cambridge University Press, 2001).
311. Humphrey, J. D. & Kyriacou, S. K. The use of Laplace's equation in aneurysm mechanics. *Neurol Res* **18**, 204–208 (1996).
312. Dijkstra, E. W. A note on two problems in connexion with graphs. *Numer. Math.* **1**, 269–271 (1959).
313. Bih, L.-I., Ho, C.-C., Tsai, S.-J., Lai, Y.-C. & Chow, W. Bladder shape impact on the accuracy of ultrasonic estimation of bladder volume. *Archives of Physical Medicine and Rehabilitation* **79**, 1553–1556 (1998).
314. Pitre, D. A., Ma, T., Wallace, L. J. & Bauer, J. A. Time-dependent urinary bladder remodeling in the streptozotocin-induced diabetic rat model. *Acta Diabetol* **39**, 23–27 (2002).
315. Fagerberg, S.-E., Kock, N. G., Peterson, I. & Stener, I. Urinary Bladder Disturbances in Diabetics: I. A Comparative Study of Male Diabetics and Controls Aged between 20 and 50 Years. *Scandinavian Journal of Urology and Nephrology* **1**, 19–27 (1967).

316. Frey, P., Sarter, B. & Gautherie, M. Fully automatic mesh generation for 3-D domains based upon voxel sets. *International Journal for Numerical Methods in Engineering* **37**, 2735–2753 (1994).
317. Huang, J., Yagel, R., Filippov, V. & Kurzion, Y. An accurate method for voxelizing polygon meshes. *Proceedings of the 1998 IEEE symposium on Volume visualization* 119–126 (1998) doi:10.1145/288126.288181.
318. Zhang, C. & Chen, T. Efficient feature extraction for 2D/3D objects in mesh representation. *Proceedings 2001 International Conference on Image Processing* (2001) doi:10.1109/ICIP.2001.958278.
319. Abrams, P., Kelleher, C. J., Kerr, L. A. & Rogers, R. G. Overactive Bladder Significantly Affects Quality of Life. *THE AMERICAN JOURNAL OF MANAGED CARE* **6**, (2000).
320. Chiaffarino, F., Parazzini, F., Lavezzari, M. & Giambanco, V. Impact of Urinary Incontinence and Overactive Bladder on Quality of Life. *European Urology* **43**, 535–538 (2003).
321. Powell, L. C., Szabo, S. M., Walker, D. & Gooch, K. The economic burden of overactive bladder in the United States: A systematic literature review. *Neurourology and Urodynamics* **37**, 1241–1249 (2018).
322. Reeves, P. *et al.* The Current and Future Burden and Cost of Overactive Bladder in Five European Countries. *European Urology* **50**, 1050–1057 (2006).
323. Wagner, T. H. *et al.* Health-Related Consequences of Overactive Bladder. *THE AMERICAN JOURNAL OF MANAGED CARE* **8**, (2002).
324. Nash, M. P. & Hunter, P. J. Computational Mechanics of the Heart. *Journal of Elasticity* **61**, 113–141 (2000).
325. Barnes, J. M., Przybyla, L. & Weaver, V. M. Tissue mechanics regulate brain development, homeostasis and disease. *Journal of Cell Science* **130**, 71–82 (2017).
326. Wahl, E. F., Lerman, S. E., Lahdes-Vasama, T. T. & Churchill, B. M. Measurement of bladder compliance can be standardized by a dimensionless number: theoretical perspective. *BJU International* **94**, 895–897 (2004).
327. Volikova, A. I. *et al.* Structural, biomechanical and hemodynamic assessment of the bladder wall in healthy subjects. *Research and Reports in Urology* **11**, 233–245 (2019).
328. Chang, S.-J., Chiang, I.-N., Hsieh, C.-H., Lin, C.-D. & Yang, S. S.-D. Age- and gender-specific nomograms for single and dual post-void residual urine in healthy children. *Neurourology and Urodynamics* **32**, 1014–1018 (2013).
329. Mahutga, R. R., Schoepfoerster, C. T. & Barocas, V. H. The Ring-Pull Assay for Mechanical Properties of Fibrous Soft Tissues – an Analysis of the Uniaxial Approximation and a Correction for Nonlinear Thick-Walled Tissues. *Exp Mech* **61**, 53–66 (2021).
330. Alexander, R. Mechanical properties of urinary bladder. *American Journal of Physiology* **220**, (1971).

331. Bailey, L. E. & Ong, S. D. Krebs-Henseleit solution as a physiological buffer in perfused and superfused preparations. *Journal of Pharmacological Methods* **1**, 171–175 (1978).
332. Sanchez-Alavez, M., Alboni, S. & Conti, B. Sex- and age-specific differences in core body temperature of C57Bl/6 mice. *AGE* **33**, 89–99 (2011).
333. William Cleveland. Robust Locally Weighted Regression and Smoothing Scatterplots: Journal of the American Statistical Association: Vol 74, No 368. *Journal of the American Statistical Association* **74**, (1978).
334. Seabold, S. & Perktold, J. Statsmodels: Econometric and Statistical Modeling with Python. in *PROC. OF THE 9th PYTHON IN SCIENCE CONF.* ((2010).
335. Wilson, C. B., Leopard, J., Cheresch, D. A. & Nakamura, R. M. Extracellular matrix and integrin composition of the normal bladder wall. *World J Urol* **14**, S30–S37 (1996).
336. Aitken, K. J. & Bägli, D. J. The bladder extracellular matrix. Part I: architecture, development and disease. *Nature Reviews Urology* **6**, 596–611 (2009).